Received September 4, 2015, accepted September 22, 2015, date of publication October 5, 2015,
date of current version December 7, 2015.

Digital Object Identifier 10.1109/ACCESS.2015.2486778

INVITED PAPER

Indoor Office Wideband Millimeter-Wave Propagation Measurements and Channel Models at 28 and 73 GHz for Ultra-Dense 5G Wireless Networks

GEORGE R. MacCARTNEY, JR., (Student Member, IEEE), THEODORE S. RAPPAPORT, (Fellow, IEEE), SHU SUN, (Student Member, IEEE), AND SIJIA DENG, (Student Member, IEEE)

NYU WIRELESS Research Center, NYU Tandon School of Engineering, Brooklyn, NY 11201, USA

Corresponding author: G. R. MacCartney (gmac@nyu.edu)

This work was supported in part by the NYU WIRELESS Industrial Affiliates: AT&T, CableLabs, Cablevision, Ericsson, Huawei, Intel Corporation, InterDigital Inc., Keysight Technologies, L3 Communications, Nokia, National Instruments, Qualcomm Technologies, Samsung Corporation, SiBeam, Straight Path Communications, and UMC, in part by the GAANN Fellowship Program, and in part by the National Science Foundation under Grant 1320472, Grant 1237821, and Grant 1302336.

ABSTRACT Ultra-wideband millimeter-wave (mmWave) propagation measurements were conducted in the 28- and 73-GHz frequency bands in a typical indoor office environment in downtown Brooklyn, New York, on the campus of New York University. The measurements provide large-scale path loss and temporal statistics that will be useful for ultra-dense indoor wireless networks for future mmWave bands. This paper presents the details of measurements that employed a 400 Megachips-per-second broadband sliding correlator channel sounder, using rotatable highly directional horn antennas for both co-polarized and cross-polarized antenna configurations. The measurement environment was a closed-plan in-building scenario that included a line-of-sight and non-line-of-sight corridor, a hallway, a cubicle farm, and adjacent-room communication links. Well-known and new single-frequency and multi-frequency directional and omnidirectional large-scale path loss models are presented and evaluated based on more than 14 000 directional power delay profiles acquired from unique transmitter and receiver antenna pointing angle combinations. Omnidirectional path loss models, synthesized from the directional measurements, are provided for the case of arbitrary polarization coupling, as well as for the specific cases of co-polarized and cross-polarized antenna orientations. The results show that novel large-scale path loss models provided here are simpler and more physically based compared to previous 3GPP and ITU indoor propagation models that require more model parameters and offer very little additional accuracy and lack a physical basis. Multipath time dispersion statistics for mmWave systems using directional antennas are presented for co-polarization, cross-polarization, and combined-polarization scenarios, and show that the multipath root mean square delay spread can be reduced when using transmitter and receiver antenna pointing angles that result in the strongest received power. Raw omnidirectional path loss data and closed-form optimization formulas for all path loss models are given in the Appendices.

INDEX TERMS Millimeter-wave, mmWave, path loss, 5G, indoor hotspot, RMS delay spread, small cell, channel sounder, propagation, 28 GHz, 73 GHz, multipath, polarization.

I. INTRODUCTION

Over the past few years there has been an explosion in mobile data traffic as a consequence of the growth of smartphones, tablets, and devices that provide, monitor, transfer, and record ZettaBytes of data every year [1]–[3]. Smartphone adoption rates are sharply increasing as carriers and service providers attempt to attract more customers [4], [5]. The advent of smartphones and ''Wireless Fidelity'' (WiFi) enabled devices has facilitated the surge in wireless technologies and applications, but has created congestion in the sub–6 GHz spectrum in which a majority of these devices operate in [6]–[9].

The 2.4 GHz and 5 GHz WiFi bands have been widely used for indoor wireless communications in typical

office environments, restaurants, and hotels since the early 2000's [10], [11], but dense deployment of indoor hotspots and new wireless multimedia devices have led to increased congestion and traffic over indoor networks [12]. Offices are ''cutting the cord'' by investing in numerous wireless multimedia devices for video. Additionally, augmented 3-Dimensional (3D) and virtual reality applications for sporting events and video games require low latency and high bandwidth capacities for seamless and uninterrupted experiences [13]. In addition to the 2.4 GHz and 5 GHz WiFi bands, the 60 GHz mmWave band is used for Wireless Gigabit Alliance (WiGig) to support high-data-rate applications. The vast available bandwidth (57-64 GHz) at 60 GHz (and unlicensed availability in the U.S. and other countries) motivated extensive 60 GHz indoor propagation measurements to understand channel characteristics necessary for designing indoor wireless local area network (WLAN) systems capable of achieving multi-gigabits-per-second throughputs [14], [15]. The study of mmWave propagation has been widely conducted at 60 GHz (with fewer at other mmWave bands) for common indoor environments in order to properly model path loss and channel characteristics.

The impending spectrum and capacity crunch for outdoor cellular may very well lead to the use of the 28 GHz and 73 GHz mmWave frequency bands as an extension for 5G outdoor and indoor communications, especially due to the trend of shrinking cell sizes. If the 28 GHz and 73 GHz bands eventually become unlicensed similar to the 60 GHz band, the wide range of applications and events they could support would tremendously reduce the load on cellular and backhaul networks as we move into the age of Internet of Things (IoT) [16]. In any case, extensive indoor propagation measurements at the 28 GHz and 73 GHz bands are needed in order to accurately characterize and model the channel to design capable indoor systems at these frequencies.

The NYU WIRELESS research center conducted extensive measurements during the summer of 2014 in a typical office building at 28 GHz and 73 GHz with various transmitter (TX) and receiver (RX) azimuth and elevation antenna pointing angle combinations and for different antenna polarization configurations. Over 70 GB of raw data were collected and are the foundation for the models and characteristics presented in this article. This paper uses extensive propagation measurements at these two promising mmWave bands, and explores many previous and new large-scale path loss models in a detailed way, and introduces new path loss models that predict signal strength (for coverage or interference analysis) as a function of distance and frequency for new mmWave frequency bands that are likely to be used for indoor and outdoor coverage in the coming decades.

Wireless spectrum above 6 GHz, specifically between 30 GHz and 300 GHz, is commonly referred to as the mmWave spectrum, and contains a massive amount of raw bandwidth that is vastly underutilized but soon could become available for unlicensed or licensed use [6], [7], [17]. To date, the only mmWave band used for widespread commercial applications is the unlicensed 60 GHz band, where oxygen absorption creates loss greater than free space compared to other mmWave bands, thus reducing signal strength over long range (several hundred meters) propagation distances [18], but alternatively helps to minimize interference in directional systems. The large swath of available spectrum in the unlicensed 57–64 GHz band (60 GHz band) represents one of the largest unlicensed areas of spectrum real-estate to achieve ultra-high data rates for multi-Gbps wireless communications performance, spectrum flexibility, and capacity [19], [20]. Additionally, the form factor of mmWave systems and antennas will be smaller, compared to sub-6 GHz systems, making it convenient for highly-directional steerable antenna arrays to be integrated into electronic products [21]–[23].

Yong *et al.* presented an overview of 60 GHz technologies and their potential to provide next generation multi-gigabit wireless communications, along with a series of technical challenges to resolve before large-scale deployments can occur [24]. A number of open issues and technical challenges have yet to be fully addressed at 60 GHz, and they can be generally classified into the following categories: channel propagation, antenna technologies, RF solutions, and modulation schemes [13], [24]–[27]. The continuously evolving IEEE 802.11ad and WiGig standards, supported by WiFi companies who recognize that current spectral resources are insufficient, will also help to further exploit the 60 GHz spectrum [18], [19], [28]–[30]. The early success of WiGig has led to new mmWave technologies and hardware that can stream high-definition (HD) wireless content between devices with 4K image resolution and low-latency video game play [31]–[33], leading the way towards a renaissance of wireless communications in the *massively broadband*® era [34].

Researchers in Japan conducted pioneering research in the 1990's in the 60 GHz band, and developed point-to-point base-stations and user-stations with mmWave monolithic microwave integrated circuit (MMIC) devices with antennas the size of a quarter that could transmit as high as 156 Mbps for WLANs [35], [36]. In a recent indoor experiment down a narrow hallway, researchers were able to transmit 7.5 Gbps at a distance of 15 m using a high gain Antipodal Linear Tapered Slot Antenna (ALTSA) at 60 GHz [37], with additional studies resulting in a path loss exponent (PLE) of 2.12 relative to a 1 meter (m) free space reference distance in line-of-sight (LOS), slightly above theoretical free space path loss (PLE = 2) [38]. Researchers in India also focused on mmWave antenna design at 60 GHz with relatively high gains and small form factors for gigabit wireless communications and applications [39].

A. PREVIOUS INDOOR CHANNEL MEASUREMENTS

Propagation measurements in indoor office environments at mmWave frequency bands are necessary for creating statistical channel models that support the development of new stan-

dards and technologies for wireless communications systems. Current WiGig and WirelessHD standards and devices are limited to short ranges in the 60 GHz band, where oxygen absorption is known to add an additional 10 to 20 dB of loss per km above the distance-dependent propagation path loss of far-field radiation [7]. As new mmWave frequency allocations are made available at frequencies that do not suffer such absorption, channel models that predict signal strength and multipath time delays (such as results given here) will be required for proper modem and system design.

1) INDOOR PROPAGATION BELOW 6 GHz

There have been myriad studies for indoor wireless propagation and channel models over the past 25 years. As just a sample of typical work in an indoor office environment, a 900 MHz signal with 200 kHz of bandwidth experienced between 28 dB and 61 dB of attenuation per decade of distance for distances up to 27 m, across multiple floors [40]. Ericsson used a path loss model from multi-floor measurements of an office building that had four breakpoints, but assumed 30 dB of attenuation at $d_0 = 1$ m (free space path loss in the first meter) at 900 MHz and measured a PLE of 2 for distances up to 10 m, and used a multiple slope model at greater distances [41]. Indoor multipath propagation measurements were performed by Saleh and Valenzuela with a 10 nanosecond (ns) probing pulse centered at 1.5 GHz with vertically polarized discone TX and RX antennas at 2 m heights [42]. The indoor channel was observed to vary slowly with time, resulting in maximum RMS delay spreads of 50 ns in adjacent rooms, and signal attenuation between 30 dB and 40 dB per decade of distance.

Bultitude measured the 910 MHz band in an indoor office-style building with a continuous wave (CW) tone transmitted at 500 mW with an omnidirectional TX antenna, and a quarter-wave monopole RX antenna [43]. Results indicated that in LOS environments, signal attenuation over distance closely followed Friis' free space path loss equation where propagating signals attenuate following the square power law. In some cases, the observed path loss was less than predicted free space path loss propagation indicating a waveguide effect in narrow hallways of the office building.

In the late 1980's, Motley and Keenan performed indoor multi-floor measurements and found PLEs of 4 and 3.5 relative to a 1 m free space reference distance at 900 MHz and 1700 MHz, respectively, using TX and RX dipole antennas [44]. Rappaport *et al.* conducted wideband multipath measurements at 1300 MHz in factory buildings with a 10 ns transmitting pulse in both LOS and non-LOS (NLOS) environments with TX and RX discone antennas that resulted in path loss attenuation of 22 dB per decade of distance and an RMS delay spread that ranged from 30 ns to 300 ns [45].

In the early 1990's, Rappaport *et al.* performed indoor measurements at 1.3 GHz and 4.0 GHz for both circularly and linearly polarized antennas. Results indicated similar propagation path loss for both frequencies, and larger cross-polarization discrimination was found in LOS channels compared to NLOS or obstructed channels [46]–[48]. Additionally, the use of an omnidirectional TX antenna and a directional circularly-polarized RX antenna provided the lowest RMS delay spread and the lowest maximum excess delay (10 dB down) among the various polarizations of omnidirectional and directional antennas.

A paper on indoor propagation by Andersen *et al.* in 1995 highlighted the value of using a 1 m close-in free space reference distance for meaningful indoor path loss models [49]. The paper also demonstrated the viability of ray-tracing for indoor channel impulse response prediction for single and multi-floor propagation. Single story retail and grocery stores had PLEs of 2.2 and 1.8 at 914 MHz, respectively, with respect to (w.r.t.) a 1 m free space reference distance. Indoor offices with soft partitions measured at 900 MHz and 1900 MHz had PLEs w.r.t. a 1 m free space reference distance of 2.4 and 2.6, respectively, with standard deviations of 9.6 dB and 14.1 dB, respectively. Radio-frequency penetration was also reported to attenuate between 3 dB and 30 dB for metallic tinted windows. Rappaport and Sandhu published a survey paper in 1994 that summarized radio-propagation measurements for frequencies between 850 MHz and 60 GHz and the problems of radio-wave propagation into buildings for wireless communications systems [50]. Average floor attenuation factors were found to be 24.4 dB and 31.6 dB at 914 MHz for a transmitter and receiver separated by 3 floors in two different office buildings.

Alvarez *et al.* studied the indoor radio channel between 1 GHz and 9 GHz, and defined four scenarios: LOS (when there was a direct path between the TX and RX), Soft-NLOS (when there was no direct path, but rather reflected paths between the TX and RX), Hard-NLOS (when there was no direct or reflected path between the TX and RX), and corridor (special case for LOS, when there was a direct path and many strong reflected paths between the TX and RX) [51]. A vector network analyzer (VNA) channel sounder with omnidirectional TX and RX antennas was used to record the channel transfer function by concatenating frequency sweeps between 1 and 5 GHz and 5 and 9 GHz. The estimated PLEs from the measurement data were 1.4 (using a free space close-in reference distance of $d_0 = 15.1$ cm) for the LOS scenario, 3.2 ($d_0 = 8.2$ cm) for Soft-NLOS, and 4.1 ($d_0 = 6.7$ cm) for Hard-NLOS.

Ghassemzadeh *et al.* used a VNA to transmit an ultra-wideband 1250 MHz radio-frequency (RF) bandwidth signal centered at 5 GHz with a conical monopole omnidirectional TX and RX antenna inside 23 homes in northern and central New Jersey [52]. In LOS environments the close-in free space reference distance path loss model relative to a 1 m free space path loss (FSPL) distance resulted in a PLE of 1.7, and was determined to be 3.1 in NLOS environments. The shadow factor standard deviation about the mean path loss lines ranged from 2.8 dB to 4.4 dB, indicating small large-scale signal fluctuations in the indoor home environments for ultra-wideband propagation at 5 GHz.

In the late 1990's Durgin *et al.* performed numerous CW indoor and outdoor-to-indoor measurements between walls and other partitions to derive path loss models in residential areas at 5.85 GHz [53]–[56]. The propagation models developed from the measurements were helpful for outdoor-to-indoor deployments, as results indicated that signals that penetrated homes attenuated on average by about 14 dB, with tree shadowing attenuation that varied from 11 dB to 16 dB. Close-in building shadowing also attenuated the propagating signals by 15 dB to 21 dB, depending on RX antenna heights.

Durgin *et al.* studied angle delay and dispersion characteristics for outdoor and indoor peer-to-peer channels centered at 1920 MHz in the early 2000's. Both omnidirectional and directional (30° half-power beamwidth (HPBW)) antennas were used to measure angles of arrival and delay spread statistics. Typical results for RMS delay spreads were 17 ns to 219 ns for outdoor cross-campus measurements, whereas three indoor-to-indoor locations resulted in 27 ns to 34 ns RMS delay spreads and *normalized angular spreads* of multipath power between 0.73 and 0.90 [57], [58]. Patawari *et al.* also studied peer-to-peer propagation at 1.8 GHz with low antenna heights and with 200 MHz of first null-to-null RF bandwidth, and measured RMS delay spreads up to 330 ns in rural areas and up to 200 ns in urban peer-to-peer environments [59].

Ray-tracing simulations are another popular method for modeling indoor and outdoor propagation channels, and are less time-intensive and less costly compared to actual measurements. Motorola demonstrated the viability of ray-tracing for its revolutionary 18 GHz Altair WLAN product in the early 1990's [60]. The University of Bristol and Virginia Tech were two of the first institutions to demonstrate the promise of ray-tracing for small-cell and indoor deployments [61]. Schaubach *et al.* used geometric optics to estimate average path loss and delay spread in microcellular environments by creating database environments and writing a computer program to perform ray-tracing on the databases. Simulations compared with time-delay measurements at 914 MHz on the Virginia Tech campus validated the program and methodology [62].

Work by Seidel *et al.* in the 1990's showed good agreement for path loss and delay spread characteristics using predictive ray-tracing techniques and measurements at 1.3 GHz and 4.0 GHz. The predicted and measured path loss differed by less than 6 dB over most locations, and RMS delay spreads were within 20 ns for each measured location in rooms with 4.5 m ceiling heights [63], [64]. Additional ray-tracing simulations using 3D building databases and transmitted, reflected, and scattered ray mechanisms successfully predicted propagation at 1900 MHz, confirmed using a spread spectrum system [65]. An indoor ray-tracing software developed in the 1990's was able to predict path loss, partition loss, and floor attenuation loss for indoor environments at various sub-6 GHz frequencies by taking advantage of attenuation models based on the types of partitions, frequency, and distance [66], [67]. Improved ray-tracers for indoor wireless propagation included 3D ray-launching methods using geodesic spheres and distributed wavefronts to increase accuracy and prediction at 900 MHz [68].

A measurement-based statistical indoor radio-channel impulse response model (SIRCIM) and statistical outdoor simulator (SMRCIM) were implemented from many thousands of collected channel impulse responses (CIRs) in factories at 1.3 GHz [69], [70], and from outdoor cellular channel power delay profiles (PDPs) [71], [72]. These CIR models were popular with industry in the 1990's during the early years of digital cellular and WiFi [73]. The SIRCIM and SMRCIM models were based on statistical and geometrical models to synthesize the phases and directions of arrival and departure in an impulse response (IR) model [73], [74].

2) INDOOR PROPAGATION ABOVE 6 GHz

Since the early 1990's, many studies at mmWave bands for the indoor environment have been conducted, predominantly in the 60 GHz band, one of the most promising candidates for multi-gigabit wireless indoor communications systems. Smulders *et al.* performed frequency-domain measurements across 2 GHz of bandwidth centered at 58 GHz in an indoor environment and employed biconical horn antennas with omnidirectional radiation patterns at the TX and RX [75]–[77]. The wideband mmWave measurements yielded RMS delay spreads between 15 ns and 45 ns in small rooms and between 30 ns and 70 ns in larger rooms indicating that more paths with considerable energy arrive at the receiver over a larger time delay in larger rooms. A worst case RMS delay spread of 100 ns was also reported.

Xu *et al.* studied the 60 GHz indoor channel using a directional horn antenna with 7° HPBW in the azimuth plane and 29 dBi of gain at the RX, and an open-ended waveguide with 90° HPBW in the azimuth plane and 6.7 dBi of gain at the TX [14], [78]. A sliding correlator channel sounder was utilized with an RF null-to-null bandwidth of 200 MHz and a 10 ns time resolution, with PDPs or channel impulse responses captured at discrete pointing angles while rotating the RX antenna. LOS measurements resulted in a PLE less than 2 (theoretical FSPL), using a 1 m close-in free space reference distance. These findings were similar to those at lower frequencies in indoor environments, where ground and ceiling bounce reflections and a waveguide effect are known to increase power at the receiver such that the measured path loss is less than theoretical FSPL.

Measurements similar to those conducted by Xu *et al.*, were performed by Bensebti *et al.* to study large-scale path loss in the indoor multipath propagation channel at 60 GHz at the University of Bristol using a spread spectrum channel sounder with directional, semi-directional, and omnidirectional TX and RX antennas placed at heights of 1.5 m [79]. Excess delay spreads ranged from 10 ns to 40 ns over short distances, with minimal deep fades. The total received discrete power was exponentially distributed in a

LOS environment along a corridor that was 3 m × 30 m for 7 m to 33 m transmitter-receiver (T-R) separation distances.

Zwick *et al.* performed numerous wideband channel measurements at 60 GHz using a heterodyne transmitter and receiver. They measured propagation at 60 GHz with a channel sounder consisting of a 500 MHz bandwidth (2 ns resolution) PN sequence as the probing signal that was transmitted at 10 different frequency slots between 59 GHz and 64 GHz and concatenated the measurements (for 5 GHz of total bandwidth), using omnidirectional antennas in several rooms for short-range distances [80]. Using omnidirectional TX and RX antennas, they measured median RMS delay spreads from 3 ns to 9 ns, in addition to calculating a PLE of 1.33 relative to a 1 m free space reference distance and a shadow factor of 5.1 dB across all measurements.

Geng *et al.* conducted 60 GHz propagation measurements in various indoor environments in continuous-route (CR) and direction-of-arrival (DOA) measurement campaigns [81]. The RMS delay spread trended to a log-normal distribution, and the typical range was from 3 ns to 80 ns. The propagation mechanisms were studied based on DOA measurements, indicating that the direct wave and the first-order reflected waves from smooth surfaces were sufficient in LOS propagation environments, while in NLOS cases, diffraction was a significant propagation mechanism, and the transmission loss through walls was very high. Geng *et al.* also conducted 60 GHz measurements in corridor, LOS hallway, and NLOS hallway environments, and the measured PLEs were 1.6 in LOS corridor, 2.2 in LOS hallway, and 3.0 in NLOS hallway environments [82].

Anderson *et al.* conducted indoor wideband measurements at 2.5 GHz and 60 GHz using a broadband vector sliding correlator channel sounder to record PDPs [83], [84]. For the 2.5 GHz measurements, both the transmitter and receiver antennas were vertically polarized omnidirectional biconical antennas with 6 dBi of gain. The transmit power before the TX antenna was 0 dBm in order to emulate 2.4 GHz WLANs operating with omnidirectional antennas. The transmit power was set to -10 dBm at 60 GHz and was necessary in order to maintain linear operation of the TX power amplifier, and to avoid saturating the RX low noise amplifier (LNA). The low transmit power (+15 dBm equivalent isotropically radiated power (EIRP) with 25 dBi antennas) was used to emulate femtocellular systems to study a typical single-cell-per-room network environment. For the 60 GHz measurements, vertically polarized pyramidal horn antennas with 25 dBi of gain and a HPBW of 50° were used at both the transmitter and receiver. Anderson *et al.* selected eight transmitter locations and 22 receiver locations with T-R separation distances from 3.5 m to 27.4 m on the same floor in a modern office building with a variety of obstructions in the signal path [83], [84]. The transmitter and receiver locations were chosen to represent a wide range of typical office femtocellular propagation environments. The heights of the transmitter and receiver antennas were 1.2 m above the floor with an exception at one receiver location where the RX antenna was 2.4 meters above the floor. By using a minimum mean square error (MMSE) fit, the PLE with respect to a 1 m free space reference distance at 2.5 GHz was found to be 2.4 with a standard deviation of 5.8 dB, and at 60 GHz the PLE was 2.1 with a standard deviation of 7.9 dB.

Manabe *et al.* investigated how the radiation patterns and antenna polarizations at remote terminals affects multipath propagation characteristics at 60 GHz, in a conference room [85], [86]. Four types of antennas were used to examine the effects of radiation patterns of RX antennas: an omnidirectional antenna and three directive antennas with wide, medium, and narrow HPBWs. The use of a directive antenna at the remote terminal was an effective method to reduce the effects of multipath propagation. Further reduction in multipath effects was achieved with the use of circularly polarized directive antennas instead of linearly polarized directive antennas.

In 2005, Moraitis and Constantinou performed indoor 60 GHz radio channel measurements by recording power delay profiles using a direct RF pulse technique with a 10 ns repetitive square pulse, modulated up to the 60 GHz carrier having a bandwidth of 100 MHz and 10 dBm of transmit power while using identical 21 dBi vertically polarized horn antennas at the TX and RX [87]. The extracted power delay profiles revealed that excess delay was less in hallways (up to 8.18 ns) compared to offices (up to 14.69 ns). The measurements also revealed that the office environment did not experience large channel variation over local areas.

Maltsev *et al.* used an 800 MHz OFDM channel sounder centered at 60 GHz using circular horn antennas at the transmitter and receiver and found that cross-polarized antennas in LOS environments could yield approximately 20 dB of isolation at 60 GHz [15], [88], and about 10-20 dB of isolation for NLOS environments. Torkildson *et al.* investigated the potential for exploiting spatial multiplexing as a means to increase spectral efficiency at 60 GHz in an indoor environment [89], [90]. The robustness of a link was observed to improve by increasing the number of antennas at the RX, which would also reduce the sensitivity of the channel capacity. The indoor channel was significantly degraded when the LOS path was blocked due to an obstruction, suggesting more accurate and elaborate channel models were needed to better assess link performance in the absence of a LOS path.

Aside from the majority of indoor propagation research at 60 GHz, little is known about other mmWave bands. In the early 1990's, Motorola conducted extensive 18 GHz indoor propagation measurements using both sectored and omnidirectional antennas in support of their Altair WLAN product, but little was published. Haneda *et al.* conducted numerous measurement campaigns in the 60 GHz and 70 GHz bands in indoor shopping malls, railway stations, and office environments using a VNA based channel sounding method over 5 GHz of bandwidth [91], [92]. The measurements employed a directional horn antenna at the TX with 20 dBi of gain, and a biconical omnidirectional antenna at the RX.

Specular reflections in the propagation channel accounted for 75% of the received power in office environments, and 90% of the received power in a shopping mall and railway station, and delay spreads were similar at both 60 GHz and 70 GHz.

Kim *et al.* studied large-scale path loss from wideband (400 MHz bandwidth) measurements in various indoor environments at 11 GHz, using both vertically and horizontally polarized TX and RX antennas [143]. Measurements resulted in attenuation slopes between 0.55 and 1.5 and between 0.36 and 1.0 in LOS for environments for co- and cross-polarized antennas, respectively. In NLOS environments, attenuation slopes were between 2.0 and 2.6 and between 2.1 and 3.0 for co- and cross-polarized antennas, respectively. Average cross-polarization power ratios were 12.8 dB for vertical to horizontal polarization and 11.6 dB for horizontal to vertical polarization.

Zhu *et al.* performed indoor channel measurements and modeling of large-scale channel parameters at 45 GHz (an unlicensed band in China) using three different sets of antennas at the TX and RX with varying HPBWs [144], [145]. Cross-polarization discrimination was observed to be larger in LOS environments compared to NLOS environments, and decreased as antenna HPBW increased (28.5 dB (LOS) vs. 23.0 dB (NLOS) for horn antennas, 18.5 dB (LOS) vs. 7.0 dB (NLOS) for open-ended waveguides, and 3.0 dB (LOS) vs. 1.0 dB (NLOS) for dipole antennas). Path loss model parameters were not tied to a close-in free space reference distance, resulting in NLOS environment attenuation slope values close to 0 or negative - which are unrealistic. This result shows the instability and lack of intuition by not using a close-in free space path loss anchor.

Wu *et al.* conducted 28 GHz indoor laboratory measurements using horn antennas that rotated in the entire azimuth plane while using a VNA to measure the channel [93]. They used the Saleh-Valenzuela model to characterize the indoor channel and were able to extract intra-cluster parameters. Lei *et al.* also performed indoor 28 GHz channel propagation measurements in an indoor environment with a VNA and a pair of 26 dBi gain horn antennas for distances up to 30 m. Path loss attenuation slopes as a function of log-distance in different indoor environments were estimated to be 2 in free space, 2.2 in a hallway, 1.2 in a corridor, and 1.8 in an office [94].

Zhao *et al.* performed reflection and penetration loss measurements at 28 GHz in and around buildings in New York City [146]. Measurement results indicated a large penetration loss of 45.1 dB through an office building with three interior walls. Additionally, outdoor tinted glass resulted in a penetration loss of 40.1 dB compared to indoor non-tinted glass that indicated 3.9 dB of penetration loss.

B. RECENT MOTIVATION FOR INDOOR mmWave STUDIES

Research groups are now beginning to study the indoor propagation channel at mmWave frequencies other than 60 GHz. Unlicensed spectrum from 64-71 GHz and mobile or fixed point-to-point WLANs in the 71–76 GHz, 81–86 GHz, and 92–95 GHz bands have been, or soon will be deployed using licensing rules and recommendations by the Federal Communications Commission (FCC) [95], [96] in the United States, the Electronic Communications Commission (ECC) [97] in Europe, the Office of Commission (Ofcom) [98] in the United Kingdom, the Canadian Radio-television and Telecommunications Commission (CRTC) [99] in Canada, and the Australian Communications and Media Authority (ACMA) [99] in Australia.

An even stronger indication for the impending use of mmWave frequency bands in future fifth generation (5G) indoor and outdoor wireless communications systems can be found in public comments filed in response to the FCC's 2014 notice of inquiry (NOI) FCC 14-154 and FCC 14-177 regarding the use of spectrum above 24 GHz [100], [101]. The UK Office of Commission (Ofcom) requested similar public comments in 2015 on the use of spectrum in higher mmWave frequency bands [102].

In this paper, we compile a massive amount of measurement data, and provide a careful comparison of well-known and new large-scale path loss models. We provide closed-form expressions for solving for the optimum (minimum error fit) solutions over distance for all of the models in this paper, and reveal that simple models using a 1 m reference distance offer remarkably good prediction accuracy compared to more complicated path loss models that are used in current 3GPP standards that require more parameters and lack a fundamental basis in physics. Section II describes the 28 GHz and 73 GHz measurement equipment and hardware, and Section III describes the measurement campaign, procedures, and locations. Section IV presents wideband mmWave directional and omnidirectional path loss models for co-, cross-, and combined-polarization antenna configurations. For the models presented in Section IV, careful analyses and optimization are given for the best-fit parameters to a number of well-known and novel single and multi-frequency path loss models for use at mmWave frequencies. Section V provides directional multipath time dispersion statistics of the indoor environment for co-, cross-, and combined-polarization antenna configurations. Conclusions are drawn in Section VI. Appendix A includes closed-form expressions for optimizing the path loss model parameters presented in the following sections and Appendix B provides the raw omnidirectional path loss values used to generate the models.

II. MEASUREMENT EQUIPMENT AND HARDWARE

Numerous outdoor mmWave propagation measurement campaigns at 28 GHz and 73 GHz in Brooklyn and Manhattan, New York [6], [103]–[107], as well as indoor propagation measurements in a typical indoor office environment from 2012–2014 have been reported by the authors [108], [109]. The same sliding correlator channel sounder systems were also used during the summer 2014 indoor propagation measurements, which are the subject of this paper.

TABLE 1. Broadband sliding correlator channel sounding system specifications for the 28 GHz and 73 GHz indoor measurement campaign [6], [103], [104], [106].

Carrier Frequency	28 GHz	73.5 GHz
Probing Signal	11^{th} order PRBS (length=2047)	
TX PN Code Chip Rate	400 Mcps	
TX PN Code Chip Width	2.5 ns	
RX PN Code Chip Rate	399.95 Mcps	
Slide Factor	8000	
Digitizer Sampling Rate	2 Megasamples / second	
RF Bandwidth (Null-to-Null)	800 MHz	
TX/RX IF Frequency	5.4 GHz	5.625 GHz
TX/RX LO Frequency	22.6 GHz	67.875 GHz
TX/RX LO Power	10 dBm	
Max. TX Output Power	23.9 dBm	12.1 dBm
TX/RX Antenna Gain	15 dBi	20 dBi
TX/RX Azimuth HPBW	28.8°	15°
TX/RX Elevation HPBW	30°	15°
Max. TX EIRP	38.9 dBm	32.1 dBm
TX Antenna Height	2.5 m	
RX Antenna Height	1.5 m	
Max. Measureable Path Loss	152 dB	162 dB
Multipath Time Resolution	2.5 ns	
TX Polarization	Vertical	
RX Polarization	Vertical / Horizontal	

A. TRANSMITTER HARDWARE

The 28 GHz and 73 GHz measurement systems employed a sliding correlator channel sounding method with superheterodyne architectures using identical baseband hardware and similar intermediate frequency (IF) and RF stages. The baseband probing signal provided 2.5 ns multipath resolution from a 400 megachips-per-second (Mcps) pseudorandom binary sequence (PRBS) generated via an 11-bit linear feedback shift register (LFSR) using emitter-coupled logic (ECL) circuitry design. In both systems the baseband sequence was modulated to an IF between 5 GHz and 6 GHz that then entered custom-designed RF front-end up-converter boxes which modulated the IF signals to RF center frequencies of 28 GHz and 73.5 GHz, with a maximum transmit power of 23.9 dBm and 12.1 dBm for each band, respectively. At the waveguide flange output of the RF front-end up-converters, the signal was transmitted through a 15 dBi gain (28.8°/30° azimuth/elevation HPBW) or 20 dBi gain (15°/15° azimuth/elevation HPBW) rotatable pyramidal horn antenna, for the 28 GHz and 73 GHz frequencies, respectively. The probing signal and frequency settings for each stage of the transmitter system architectures are provided in Table 1. Block diagrams of the 28 GHz and 73 GHz transmitter hardware are shown in [6], [103], [104], and [108].

To perform directional measurements across different azimuth and elevation planes, the directional antennas were mechanically steered using LabVIEW controlled gimbals with sub-degree accuracy in both planes. This allowed us to transmit over a large portion of the 4π steradian sphere, emulating a near-omnidirectional TX antenna. Thus, many angles of departure (AODs) were used to measure the indoor environment.

B. RECEIVER HARDWARE

The 28 GHz and 73 GHz receivers employed identical pyramidal horn antennas as used at the TX (a 15 dBi gain and 20 dBi gain antenna at 28 GHz and 73 GHz, respectively). The incoming 800 MHz null-to-null RF bandwidth signal was downconverted to an IF stage between 5 GHz and 6 GHz in both architectures and then subsequently demodulated into its I and Q baseband components. Both the I and Q baseband components were then mixed with a PRBS sequence identical to the transmitted signal, but at a slightly slower rate of 399.95 Mcps, which produced an impulse when both codes were aligned in time. The cross-correlation mixing operation reduced the bandwidth of the I and Q signals to 50 kHz due to the time dilation properties of sliding correlation [73], [110], [111]. The subsequent I and Q voltage signals were low-pass filtered and then individually sampled at 2 MS/s. Using LabVIEW software, the digital I and Q samples ($I^2 + Q^2$) were squared and then summed to generate the raw PDP of the channel. In order to increase the SNR of the received signal, 20 successive PDPs were averaged to obtain a recorded PDP for each individual measurement.[1]

At the receiver, directionality across a large portion of the azimuth and elevation planes was made possible by mechanically steering the directional receiver antennas with gimbals controlled by LabVIEW software. The flexibility in maneuvering the RX antenna allowed many different angles of arrival (AOAs) over the entire 360° azimuth plane and many elevation planes to be measured (measurement details are explained in Section III). Block diagrams of the 28 GHz and 73 GHz receiver hardware are provided in [6], [103], [104], and [108], and specifications of the receiver hardware and equipment are given in Table 1.

III. MEASUREMENT ENVIRONMENT AND EXPERIMENTAL PROCEDURES

Measurements were conducted in the NYU WIRELESS research center on the 9^{th} floor of 2 MetroTech Center in downtown Brooklyn, New York, which is a 10-story building constructed in the early 1990's with tinted windows and steel reinforcement between each floor. The 9^{th} floor is a typical single floor office environment with common obstructions such as desks, chairs, cubicle partitions, offices, classrooms, doors, hallways, walls made of drywall, and elevators. We tried to measure between adjacent floors (9^{th} to 10^{th}) with a wide range of antenna pointing angle combinations between the TX and RX at 73 GHz with maximum transmit power,

[1] Some results in this paper may be slightly different than initially reported in [103] and [109] due to this updated averaging method and the use of a more stringent 5 dB SNR thresholding algorithm described in [112].

but the metal and concrete structure and tinted glass windows of the building prevented any signals from being measured between adjacent office floors. This test was not attempted at 28 GHz. Identical TX and RX locations were used for both the 28 GHz and 73 GHz measurements with both co- and cross-polarization antenna configurations between the TX and RX. For co-polarization measurements, the TX and RX horn antennas were vertically polarized (V-V), whereas for the cross-polarization measurements, the TX antenna was vertically polarized and the RX antenna was horizontally polarized (V-H). Since future mmWave wireless systems will be used by people and appliances with various physical orientations, approximately half of the measurements used co-polarized antennas at the TX and RX, and half used cross-polarized antennas. TX antennas were placed 2.5 m above the floor, very close to the 2.7 m ceiling to emulate common indoor hotspot locations, and RX antennas were placed 1.5 m above the floor (typical handset level heights).

TABLE 2. TX and corresponding RX locations measured for the 28 GHz and 73 GHz indoor propagation measurements referenced to Fig. 1. 3D T-R separation distance ranges are provided for each TX and corresponding RX locations, as well as RX locations that experienced outage (e.g. no detectable signal for all pointing angles) for V-V or V-H antenna polarization configurations. A "-" indicates no outage and the RX ID number indicates where an outage occurred.

TX ID	RX IDs	T-R Dist. (m)	V-V Outages		V-H Outages	
			28 GHz	73 GHz	28 GHz	73 GHz
1	1–9	$6.4 \leq d \leq 32.9$	-	9	9	8, 9
2	10, 11–22, 161	$4.1 \leq d \leq 45.9$	-	17, 20	14, 15, 17	13–15, 17, 19, 20
3	16,17, 23–27	$5.3 \leq d \leq 8.7$	-	-	-	-
4	11–16, 18, 28, 121, 161	$7.1 \leq d \leq 33.0$	-	-	-	-
5	8, 19, 28–33	$3.9 \leq d \leq 31.2$	-	-	-	-

A. MEASUREMENT LOCATIONS AND ENVIRONMENTS

Five TX locations and 33 RX locations were selected, resulting in measurements from 48 TX-RX location combinations that had 3D T-R separation distances ranging from 3.9 m to 45.9 m, with RX locations chosen in LOS and NLOS environments (the floor dimensions were 35 m × 65.5 m). The 10 LOS measurement locations had 3D distances ranging from 4.6 m to 21.3 m, and the 38 NLOS measurement locations had 3D distances that ranged from 3.9 m to 45.9 m.

Fig. 1 displays a map of the five TX locations, the 33 RX locations (some were used for multiple transmitters), and basic descriptions of the surrounding obstructions. The TX locations were selected to study specific indoor environments such as open- and closed-plan settings, indoor hotspots, hallways, corridors, and office spaces. The three main indoor environments measured during the campaign were corridor, open-plan, and closed-plan, and they align well with measurements used in 3GPP and WINNER models. A corridor environment is when a propagating signal travels down a corridor to reach the receiver by a LOS path, reflections, scattering, and/or diffraction, but not penetration. An open-plan environment includes a cubicle-farm and a central TX location around soft partitions such as cubicle walls [67], [113]. A closed-plan environment is when a propagating signal must penetrate an obstruction such as a fixed building wall to reach the receiver. Each of the measurement environments described here are generally included in a closed-plan environment.

A subset of RX locations (typically 8 to 10) were measured for each TX location during the measurement campaign. The identical 48 TX-RX location combinations were measured at 28 GHz and 73 GHz, to enable direct comparison across the two frequency bands. Table 2 provides the RX locations that were measured for each TX location, and indicates which TX-RX combinations resulted in outages (for V-V, V-H, or both antenna polarization configurations). Fig. 2 displays an image of the environment surrounding the TX1 location. The RX121 and RX161 locations were identical to the RX12 and RX16 locations, however the glass door near RX16 was propped open for RX121 and RX161 measurements and was closed for RX12 and RX16 measurements. The RX121 and RX161 locations are included in the 48 TX-RX location combinations measured.

B. MEASUREMENT PROCEDURES

The propagation measurements at 28 GHz and 73 GHz were conducted with the same TX and RX locations (see map in Fig. 1). For each measured TX-RX location combination, 16 overall unique antenna azimuth sweeps were performed to investigate AOD and AOA statistics. An antenna sweep consisted of a fixed TX antenna in the elevation and azimuth planes, with the RX antenna fixed in elevation, where PDPs were recorded at step increments as the RX antenna was rotated in the azimuth plane (for AOAs), or a fixed RX antenna in the elevation and azimuth planes, with the TX antenna fixed in elevation and where PDPs were recorded at step increments as the TX antenna was rotated in the azimuth plane (for AODs). For each antenna sweep, the TX and RX antennas were rotated in step increments of 30° or 15° in the azimuth plane (approximately the antenna azimuth HPBW) for the 28 GHz and 73 GHz measurements, respectively. The measurements for each TX and RX combination included two antenna polarization combinations: V-V and V-H. The first eight of the 16 measurement sweeps were for the V-V antenna polarization configuration. For the eight V-V measurement sweeps, two were AOD sweeps (TX sweeps) and six were AOA sweeps (RX sweeps) with different fixed TX and RX antenna elevations. For one AOA sweep (Measurement 1, denoted as M1) and one AOD sweep (M6), the TX and RX antennas were aligned on boresight in the azimuth and elevation planes regardless

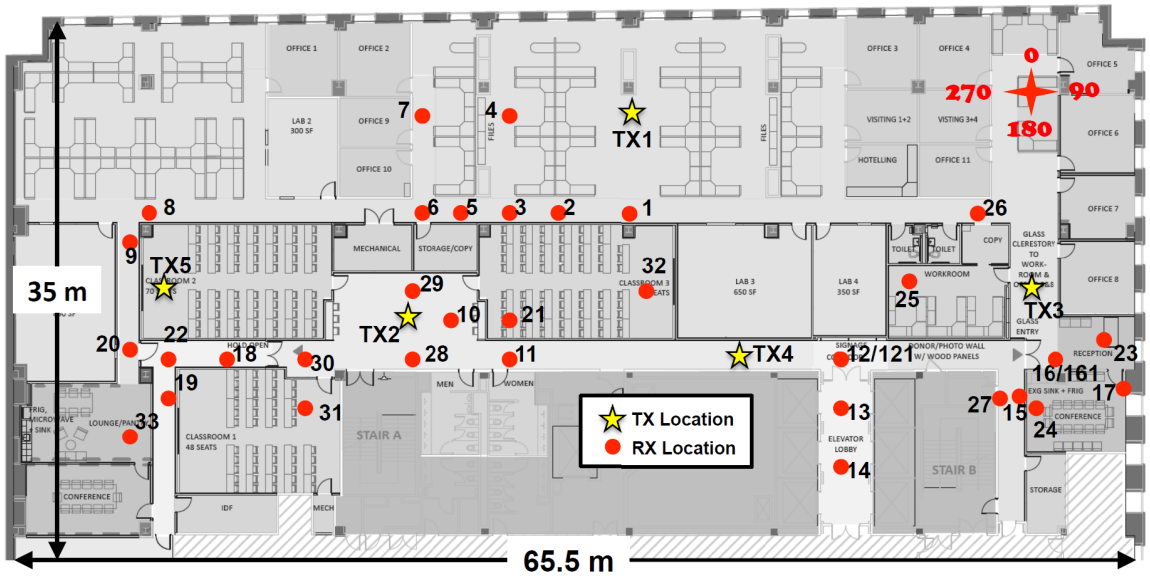

FIGURE 1. Map of the 2 MetroTech Center 9th floor with five TX locations and 33 RX locations. The yellow stars represent the TX locations and the red dots represent the RX locations. The compass in the top right corner indicates the coordinate system used inside the building for AOD and AOA angle conventions and for post-processing analyses. The RX121 and RX161 locations were identical to the RX12 and RX16 locations, however the glass door near RX16 was propped open for RX121 and RX161 measurements, and was closed for RX12 and RX16 measurements. The RX121 and RX161 locations are included in the 48 TX-RX measured locations.

FIGURE 2. TX1 location with surrounding cubicles, desks, chairs, drywall columns, and windows. The TX antenna was placed 2.5 m above the floor, near the 2.7 m tall ceiling.

of whether the environment was LOS or NLOS (boresight pointing angles for each TX-RX location combination in LOS and NLOS environments were determined via trigonometry before each measurement day). For LOS measurements the trigonometry calculations were verified during boresight alignment. Following M1, two AOA sweeps were performed with the RX antenna uptilted (M2) and downtilted (M3) by one antenna HPBW with respect to the boresight elevation angle, while the TX antenna remained fixed at the boresight angle in the azimuth and elevation planes. Afterwards, two additional AOA sweeps were conducted with the TX antenna uptilted (M4) and downtilted (M5) by one antenna HPBW with respect to the boresight elevation angle, with the RX antenna elevation fixed at the initial boresight angle. For larger T-R separation distances, the RX antenna started to point closer to the horizon than at closer distances. Additionally, one final AOA sweep (M7) was performed with the TX antenna set to the second strongest AOD (found during M6), and finally, a second AOD sweep (M8) was conducted with the TX antenna either uptilted or downtilted by one antenna HPBW after determining the elevation plane with the strongest received power from M4 and M5.

The identical first eight co-polarized antenna measurement sweeps were performed for Measurements 9–16 (M9–M16), but for cross-polarized (V-H) TX (vertical) and RX (horizontal) antennas. A detailed account of the measurements is provided in Table 3. At each unique pointing angle combination during a measurement sweep, a PDP was acquired at the receiver. Up to 192 (16 measurements × 12 ($\frac{360°}{30°}$) angles) and 384 (16 measurements × 24 ($\frac{360°}{15°}$) angles) total PDPs were possible for acquisition at each TX-RX location combination for the 28 GHz and 73 GHz measurements, respectively. Measurements at most NLOS locations, however, only provided a small number of angles with energy for recording, since most pointing angles at a particular receiver location did not have detectable energy.

IV. LARGE-SCALE PATH LOSS MODELS

Path loss models estimate the attenuation over distance of propagating signals, and are vital for designing communications systems. Different types (deterministic, empirical, and stochastic) of large-scale path loss models exist, but measurement-based path loss models provide realistic insight into propagation characteristics of a wireless channel [112], [114]. Single frequency and multi-frequency

IEEE Access
The journal for rapid open access publishing

TABLE 3. 28 GHz and 73 GHz initial antenna angles and orientations for each measurement sweep conducted for every TX-RX location combination. Elevation angles are with respect to the boresight angles determined via trigonometry regardless of whether the environment was LOS or NLOS. HPBW step increments were used for the azimuth sweeps or when changing elevation planes. The 73 GHz step increments were 15° and the 28 GHz step increments were 30°.

Meas. No.	TX Azimuth	TX Elevation	RX Azimuth	RX Elevation	Sweep Type	Polarization
M1	0	0	0	0	RX	V-V
M2	0	0	0	+HPBW	RX	V-V
M3	0	0	0	-HPBW	RX	V-V
M4	0	+HPBW	0	0	RX	V-V
M5	0	-HPBW	0	0	RX	V-V
M6	0	0	0	0	TX	V-V
M7	2nd strongest AOD	0	0	0	RX	V-V
M8	0	+/- HPBW	0	0	TX	V-V
M9	0	0	0	0	RX	V-H
M10	0	0	0	+HPBW	RX	V-H
M11	0	0	0	-HPBW	RX	V-H
M12	0	+HPBW	0	0	RX	V-H
M13	0	-HPBW	0	0	RX	V-H
M14	0	0	0	0	TX	V-H
M15	2nd strongest AOD	0	0	0	RX	V-H
M16	0	+/- HPBW	0	0	TX	V-H

path loss models are defined and studied in the following section. The distances d in the models are 3D T-R separation distances based on measurements. Additionally, both co- and cross-polarized path loss models and combined polarization path loss models are given for directional and omnidirectional cases. For combining the polarization measurements, the co- and cross-polarized measurements were lumped into one dataset. For omnidirectional models, the measurements for co- and cross-polarized antennas for the same identical locations were considered *separate*, since full antenna sweeps were conducted across large portions of the azimuth and elevation planes to synthesize omnidirectional path loss at one location for a specific polarization configuration.

A. SINGLE FREQUENCY PATH LOSS MODELS

A common path loss model is the *close-in free space reference distance (CI)* path loss model provided in Eq. (1) and parameterized by the singe model parameter n, also known as the PLE:

$$\mathrm{PL}^{\mathrm{CI}}(f,d)[\mathrm{dB}] = \mathrm{FSPL}(f,d_0) + 10n\log_{10}\left(\frac{d}{d_0}\right) + X_\sigma^{\mathrm{CI}} \quad \text{for } d \geq d_0, \quad \text{where } d_0 = 1 \text{ m} \tag{1}$$

where X_σ^{CI} is a zero mean Gaussian random variable with standard deviation σ in dB (large-scale channel fluctuations due to shadowing [73]). The CI model uses a physically-based reference distance d_0, where $\mathrm{FSPL}(f,d_0) = 10\log_{10}(\frac{4\pi d_0}{\lambda})^2$. The CI path loss model is found by determining the PLE n via the MMSE approach that fits the measured data with smallest error (by minimizing σ) using a true physical anchor point that expresses the free space transmitted power from the TX antenna out to the close-in distance d_0. The closed-form expression for optimizing the CI PLE can be found in Appendix A. For the mmWave CI model, $d_0 = 1$ m is used, proposed as a standard in [49] and [112]. High gain directional antennas may have far-field radiation patterns (Fraunhofer distances) greater than 1 m from the antenna, but the CI path loss model can easily be reverted back to a 1 m reference distance by assuming that the far-field begins at 1 m (even if it does not). The error between the near- and far-field will not be significant in communication analysis using a 1 m reference distance, since very few users would ever be this close to the TX antenna, and close-in users will have extremely strong signals and little path loss [112]. Standardizing to a $d_0 = 1$ m reference distance allows for easy model comparison between different frequency bands and measurements from other researchers, and allows closed-form computation in analysis, and intuitive computation of path loss or received power without a calculator, since the power decays by $10n$ dB per decade of distance beyond 1 m [112]. The CI path loss model may be used for estimating path loss from either cross- or co-polarization measurements, or for a generalized data set that combines both co- and cross-polarized (combined polarized) measurements (as would occur in a practical cellular system with random device orientations). As shown in [112], the single-parameter CI model may be used for multiple frequencies with good accuracy in outdoor channels, but as shown subsequently, a two-parameter variation of the CI model offers a better fit for indoor channels.

An extension of the basic (CI) path loss model for the special case of cross-polarization propagation is to add a constant attenuation factor known as the *cross-polarization discrimination* (XPD) factor, that best fits the measured data via an MMSE method [46], [48], [73], [115], [144] given by:

$$\mathrm{PL}^{\mathrm{CIX}}(f,d)[\mathrm{dB}] = \mathrm{FSPL}(f,d_0) + 10n_{(\mathrm{V\text{-}V})}\log_{10}\left(\frac{d}{d_0}\right) + \mathrm{XPD}[\mathrm{dB}] + X_\sigma^{\mathrm{CIX}} \tag{2}$$

This model, which we call the *close-in reference distance with XPD (CIX)* path loss model, is similar to the constant floor attenuation model introduced in [66], [67], and [113] and the cross-pol discrimination given in [115], and uses the co-polarization PLE in (1) to determine the best fit XPD factor caused by antenna polarization mismatch. Instead of solving for a PLE for cross-polarized measured path loss in (1), the CIX model uses the PLE (as a constant) found from co-polarized antenna measurements at identical locations of cross-polarized measurements, and adds an optimized constant attenuation (XPD). One simply solves for the optimal XPD value (in dB) via the MMSE method (while selecting as a constant, the PLE value from the co-polarized measurements) that fits the measured cross-polarized path loss data with the smallest error (by minimizing σ). As seen from (2), the CIX model uses the optimum attenuation factor (XPD) in dB that is added to the CI model to minimize the error between the estimated and measured cross-polarized path loss. In (2), $n_{(\mathrm{V\text{-}V})}$ represents the co-polarization PLE determined from measurements, as provided in Table 5, XPD

is the optimized cross-polarization attenuation factor in dB, and X_σ^{CIX} is the zero mean Gaussian (in dB) shadow fading random variable for the CIX model in (2) that describes the large-scale variation of signal power about mean path loss and constant XPD attenuation term as a function of distance. The CIX model provides the best-fit to the cross-polarized data (minimizes error via MMSE), while using the co-polarized PLE from (1) and a 1 m free space reference distance. The CIX model closed-form expressions for optimizing the XPD value are given in Appendix A.

The *floating-intercept (FI)* path loss model is used in the WINNER II and 3GPP standards [116], [117]. This model requires two parameters and does not consider a physically-based anchor to the transmitted power, and has a similar form to (1):

$$\mathrm{PL}^{\mathrm{FI}}(d)[\mathrm{dB}] = \alpha + 10 \cdot \beta \log_{10}(d) + X_\sigma^{\mathrm{FI}} \tag{3}$$

where α is the floating-intercept in dB (different than a FSPL reference), and β is the slope of the line (different than a PLE), also with a zero mean Gaussian (in dB) shadow fading random variable X_σ^{FI} which describes large-scale signal fluctuations about the mean path loss over distance. Similar to the CI and CIX models, the best-fit involves solving for α and β to minimize σ and the closed-form optimized solutions are provided in Appendix A. Note that (3) requires two model parameters, whereas the CI model only required a single parameter, the PLE. Previous work indicated that the CI and FI path loss models produce very similar shadow fading standard deviations in outdoor mmWave channels [112], [118]–[120], casting doubt on the value of using an extra modeling parameter when there is a lack of physical relationship to transmitted power.

B. MULTI-FREQUENCY PATH LOSS MODELS

A multi-frequency three-parameter model known as the *alpha-beta-gamma (ABG)* model includes a frequency-dependent and distance-dependent term to describe path loss at various frequencies [120], [121]. The ABG model equation is given by (4):

$$\mathrm{PL}^{\mathrm{ABG}}(f,d)[\mathrm{dB}] = 10\alpha \log_{10}\left(\frac{d}{d_0}\right) + \beta + 10\gamma \log_{10}\left(\frac{f}{1\ \mathrm{GHz}}\right) + X_\sigma^{\mathrm{ABG}}, \quad \text{where } d_0 = 1\ \mathrm{m} \tag{4}$$

where α and γ are coefficients that describe the distance and frequency dependence on path loss, β is an optimized offset parameter that is devoid of physical meaning, f is the frequency in GHz, and X_σ^{ABG} is Gaussian random variable representing the shadowing or large-scale signal fluctuations about the mean path loss over distance. The ABG model is an extension of the FI model for multiple frequencies, and reverts to the FI model (when setting $\gamma = 0$ or 2) if only a single frequency is used. The ABG model is solved via MMSE to minimize σ by simultaneously solving for α, β, and γ. Note that the ABG model is identical to the CI model if we equate α in the ABG model in (4) with the PLE n in the CI model in (1), γ in (4) with the free space PLE of 2, and β in (4) with $20\log_{10}(4\pi \times 1 \times 10^9/c)$. Furthermore, the ABG model requires three parameters and the CI model only requires one parameter, and as shown subsequently, the additional two variables in the ABG model offer very little improvement in accuracy and little connection to propagation physics [112], [122]. The closed-form expressions for optimizing the ABG model parameters are derived in Appendix A.

Similar to the CIX model, one may consider the *alpha-beta-gamma with XPD factor (ABGX)* model that is used for the specific case of cross-polarized propagation measurements. The ABGX model is provided in (5):

$$\mathrm{PL}^{\mathrm{ABGX}}(f,d)[\mathrm{dB}] = 10\alpha \log_{10}\left(\frac{d}{d_0}\right) + \beta + 10\gamma \log_{10}\left(\frac{f}{1\ \mathrm{GHz}}\right) + \mathrm{XPD}[\mathrm{dB}] + X_\sigma^{\mathrm{ABGX}}, \quad \text{where } d_0 = 1\ \mathrm{m} \tag{5}$$

where the optimum α, β, and γ values found for the ABG co-polarized measurement locations are used as constants to solve for the XPD value using identical cross-polarized locations that minimizes σ via MMSE. The closed-form expressions that optimize the XPD factor for the ABGX model when using the optimized co-polarized ABG model parameters are provided in Appendix A.

A new simple two-parameter multi-frequency model can be considered to be an extension of the CI model. The *close-in free space reference distance with frequency dependent path loss exponent (CIF)* path loss model is a multi-frequency model that employs the same physically motivated FSPL anchor at 1 m as the CI model. The CIF model equation is presented in (6):

$$\mathrm{PL}^{\mathrm{CIF}}(f,d)[\mathrm{dB}] = \mathrm{FSPL}(f,d_0) + 10n\left(1 + b\left(\frac{f-f_0}{f_0}\right)\right)\log_{10}\left(\frac{d}{d_0}\right) + X_\sigma^{\mathrm{CIF}}, \quad \text{where } d_0 = 1\ \mathrm{m} \tag{6}$$

where n denotes the distance dependency of path loss (e.g. the path loss exponent, or PLE), b is an intuitive model-fitting parameter that represents the slope of linear frequency dependency of path loss, thus modeling the results here which show that path loss increases with frequency at a specific distance for indoor channels,[2] f_0 is a fixed reference frequency that serves as the balancing point or center of the linear frequency dependency of the PLE, and is based on the weighted average of all frequencies represented by the model, and X_σ^{CIF} is the zero mean Gaussian (in dB) random variable

[2]As shown in [112], outdoor channels exhibit a PLE that does not have a strong frequency dependence – virtually all of the frequency dependence is captured in the first meter of free space propagation. However, indoor channels, as shown here, have a PLE that is much more frequency dependent beyond the first meter and are more lossy as frequency increases.

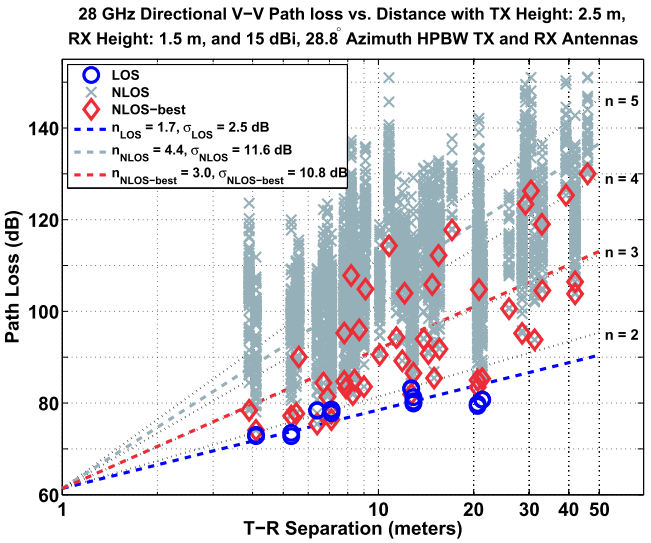

(a) 28 GHz V-V indoor directional path loss

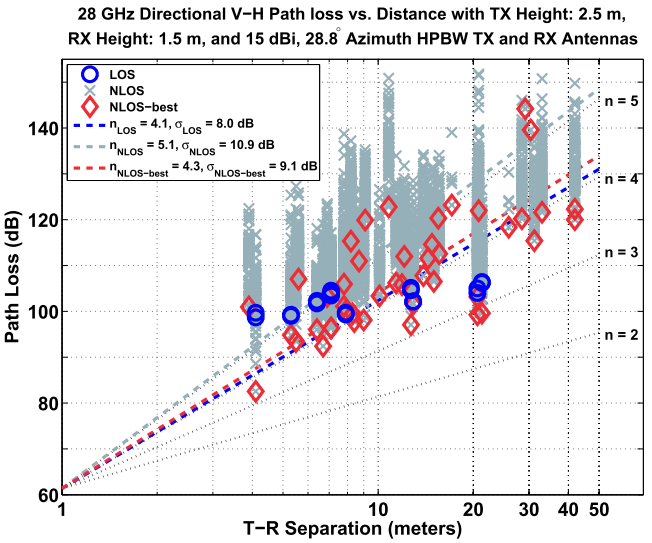

(b) 28 GHz V-H indoor directional path loss

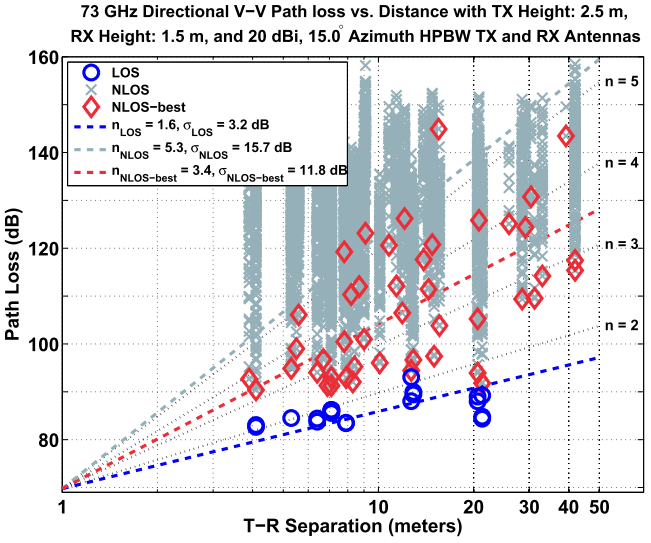

(c) 73 GHz V-V indoor directional path loss

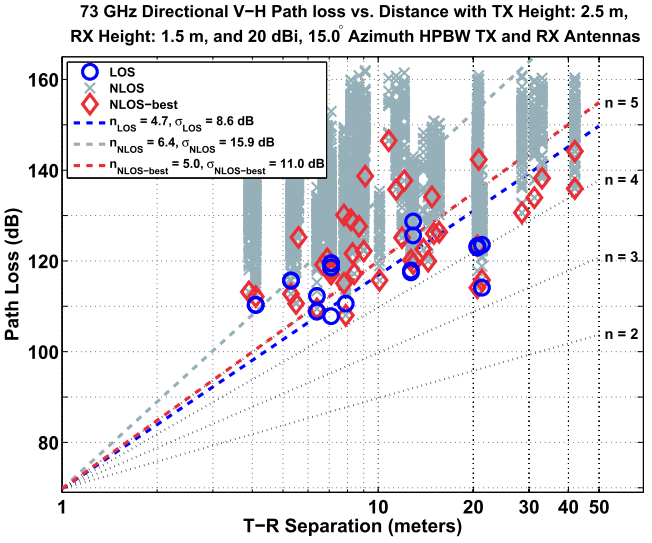

(d) 73 GHz V-H indoor directional path loss

FIGURE 3. Single frequency 28 GHz and 73 GHz indoor directional CI ($d_0 = 1$ m) path loss models with TX antenna heights of 2.5 m and RX antenna heights of 1.5 m in a typical office environment for co- and cross-polarized TX and RX antennas. Each blue circle represents LOS path loss values, gray crosses represent NLOS path loss values measured at arbitrary antenna pointing angles between the TX and RX (provided that signal could be received), and red diamonds represent angles with the lowest path loss measured for each NLOS TX-RX location combination.

that describes large-scale signal fluctuations about the mean path loss over distance. Note that the CIF model (6) reverts to the CI model (1) when the slope $b = 0$ or when data from just one frequency is used.

In the multi-frequency CIF model, the parameter f_0 is computed as: $f_0 = \sum_{k=1}^{K} f_k N_k \big/ \sum_{k=1}^{K} N_k$ where f_0 is the weighted frequency average of all measurements for each specific environment and antenna scenario, found by summing up, over all frequencies, the number of measurements N_k at a particular frequency and antenna scenario, multiplied by the corresponding frequency f_k, and dividing that sum by the entire number of measurements $\sum_{k=1}^{K} N_k$ taken over all frequencies for that specific environment and antenna scenario. Here we rounded the calculated f_0 to the nearest integer in GHz. For example, the combined polarization omnidirectional multi-frequency models in this paper used $f_0 = 51$ GHz in LOS and $f_0 = 49$ GHz in NLOS, based on the number of measured locations and measurements at each frequency in each environment. With a specified f_0, the MMSE method is used to simultaneously solve for the model parameters b and n that minimize σ. The CIF model has a similar form as the ABG model (both have a frequency term, distance term, and constant intercept term) but CIF only requires two model parameters instead of three, while also including the close-in free space distance for maintaining a physical tie to transmitted power [112], [122]. The CIF closed-form

TABLE 4. Path loss environment definitions for directional path loss models.

Setting	Description
LOS	Path loss determined for environments when TX and RX antennas are pointed at each other, aligned on boresight with no obstructions between them.
NLOS	Path loss determined for environments when TX and RX antennas are separated by obstructions and there is no clear optical path between the antennas. This scenario also includes the case where the TX and RX antennas have a clear line-of-sight path to one another, but the antennas are not aligned on boresight.
NLOS-best	Path loss determined for the unique antenna pointing angles (in the azimuth and elevation planes) resulting in the strongest received power for each specific TX-RX location combination. This results from the single strongest measured PDP from the *NLOS* data at each TX-RX location.

TABLE 5. Single frequency directional CI path loss model (1) parameters with $d_0 = 1$ m for 28 GHz and 73 GHz indoor channels with TX heights of 2.5 m and RX heights of 1.5 m for V-V and V-H antenna polarization configurations. The 28 GHz TX and RX antennas had 15 dBi (28.8° azimuth HPBW) of gain and the 73 GHz TX and RX antennas had 20 dBi (15° azimuth HPBW) of gain. "Freq." stands for carrier frequency and "Pol." stands for TX-RX antenna polarization configuration. The LOS distances ranged from 4.6 m to 21.3 m and the NLOS distances ranged from 3.9 m to 45.9 m.

Single Frequency Directional CI Path Loss Models for $d_0 = 1$ m							
Freq.	Pol.	LOS		NLOS		NLOS-best	
		PLE	σ [dB]	PLE	σ [dB]	PLE	σ [dB]
28 GHz	V-V	1.7	2.5	4.4	11.6	3.0	10.8
	V-H	4.1	8.0	5.1	10.9	4.3	9.1
73 GHz	V-V	1.6	3.2	5.3	15.7	3.4	11.8
	V-H	4.7	8.6	6.4	15.9	5.0	11.0

expressions for the best fit model parameters are given in Appendix A.

A *CIF XPD factor (CIFX)* model naturally follows, similar to the CIX and ABGX models for estimating path loss with cross-polarized antennas over multiple frequencies. The CIFX model equation is provided in (7):

$$\begin{aligned} \mathrm{PL}^{\mathrm{CIFX}}(f,d)[\mathrm{dB}] &= \mathrm{FSPL}(f,d_0) \\ &\quad +10n\left(1+b\left(\frac{f-f_0}{f_0}\right)\right)\log_{10}\left(\frac{d}{d_0}\right) \\ &\quad +\mathrm{XPD}[\mathrm{dB}]+X_\sigma^{\mathrm{CIFX}}, \quad \text{where } d_0 = 1 \text{ m} \end{aligned} \tag{7}$$

where the n and b values found for the co-polarized CIF model and the same f_0 parameter are used as constants to solve for the XPD that minimizes σ via MMSE. The closed-form expressions for optimizing the CIFX model parameters are similar to the CIX and ABGX models and are provided in Appendix A. It is important to note that the single frequency CI model (1) can also be used as a multi-frequency path loss model, while requiring only a single parameter, PLE [112].

C. DIRECTIONAL PATH LOSS MODELS FOR CO- AND CROSS-POLARIZED ANTENNAS

Directional path loss models are useful for modeling systems at mmWaves that may use directional antennas for arbitrary direction pointing, beam steering, or beam combining techniques [123], [124]. Previous work at 28, 38, 60, and 73 GHz in outdoor environments provided insights into directional path loss models [6], [106], [112], [125]–[127]. Now, path loss models are given for 28 GHz and 73 GHz indoor channels. The definitions for descriptors of the physical environments for directional path loss models are identical to those used in [112], and are given in Table 4. Figs. 3a and 3b display the directional path loss scatter plots and best fit CI models (1) at 28 GHz in LOS and NLOS environments for co-polarization (V-V) and cross-polarization (V-H) antenna configurations, respectively. Each plot also shows the *NLOS-best* CI path loss model (see Table 4) that considers only the strongest received power for each measured NLOS TX-RX location combination. For V-V antenna polarizations, the LOS PLE is 1.7 at 28 GHz and 1.6 at 73 GHz, both less than the theoretical free space PLE of 2, and virtually identical at both frequencies, indicating that the indoor mmWave propagation channel experiences constructive interference from ground and ceiling bounce reflections and a waveguide effect down hallways and corridors that has a LOS directional PLE that is not frequency dependent. The same phenomena were reported at lower microwave and Ultra-High Frequency (UHF) bands in indoor environments [45], [128]. Table 4 shows that by using the strongest single beam combination between the TX and RX at a NLOS location, the signal level is greatly improved (PLE is reduced) when compared to arbitrary beam pointing. This improvement is more prominent at 73 GHz, where the path loss is much greater (PLE = 5.3) for arbitrary pointing beams, and is reduced to PLE = 3.4 for the single best beam formation between the TX and RX antennas.

The 28 GHz LOS V-H CIX directional path loss model (2) indicates an XPD factor of 24.7 dB for cross-polarized antennas indicating that strong polarization discrimination exists in LOS environments [15], [46], [48], [88], [115]. The CI LOS PLE (n) at 28 GHz for V-H is 4.1, much greater than the 28 GHz V-V CI LOS PLE (1.7), shown in Table 5 and Table 6 for 3D T-R separation distances d. For NLOS environments, the 28 GHz CI PLE is 4.4 and 5.1 for the V-V and V-H antenna polarization configurations, respectively. This indicates a significant de-polarization effect in NLOS indoor environments at 28 GHz, and is further emphasized by the XPD factor of 9.1 dB determined from (2), which is substantially less than the 24.7 dB XPD factor found for 28 GHz LOS indoor mmWave channels. Similar results were noticed for the 73 GHz indoor channel, where LOS environments indicate an XPD factor of 31.4 dB, much greater than the XPD factor of 14.3 dB for NLOS environments.

Tables 5 and 6 show the directional CI (1) and CIX (2) path loss model parameters, respectively, with $d_0 = 1$ m at 28 GHz and 73 GHz in the indoor environment. Results in Table 5 are slightly different than those initially published

IEEE Access
The journal for rapid open access publishing

TABLE 6. Single frequency directional CIX path loss model (2) parameters with $d_0 = 1$ m for 28 GHz and 73 GHz indoor channels with TX heights of 2.5 m and RX heights of 1.5 m for V-H antenna polarization configurations. The 28 GHz TX and RX antennas had 15 dBi (28.8° azimuth HPBW) of gain and the 73 GHz TX and RX antennas had 20 dBi (15° azimuth HPBW) of gain. "Freq." stands for carrier frequency and "Pol." stands for TX-RX antenna polarization configuration.

Single Frequency Directional CIX Path Loss Model Parameters for $d_0 = 1$ m										
Freq.	Pol.	LOS			NLOS			NLOS-Best		
		$n_{(V\text{-}V)}$	XPD [dB]	σ [dB]	$n_{(V\text{-}V)}$	XPD [dB]	σ [dB]	$n_{(V\text{-}V)}$	XPD [dB]	σ [dB]
28 GHz	V-H	1.7	24.7	2.6	4.4	9.1	9.6	3.0	14.0	8.7
73 GHz	V-H	1.6	31.4	4.6	5.3	14.3	13.2	3.4	18.4	8.7

in [109] due to more stringent noise thresholding described in [112]. The 28 GHz and 73 GHz LOS PLEs for V-V are 1.7 and 1.6, respectively, due to constructive interference, and the shadow fading (SF) standard deviations for V-V and V-H measurements at the two bands are approximately 3 dB and 8 dB for the CI models, respectively. The 73 GHz NLOS CI model shows a much larger shadow fading standard deviation that is approximately 16 dB for V-V and V-H configurations, indicating much larger fluctuations in received signal strength around the mean received power over all T-R separation distances, regardless of whether the polarizations are matched or not. The NLOS CIX models at 28 GHz and 73 GHz are better estimates of cross-polarization path loss compared to the CI model as they have smaller SF values (1.3 dB and 2.7 dB less) than the CI V-H path loss models.

Table 7 shows the parameters for the FI model, where it can be seen that α values can vary widely compared to free space path loss at 1 m in LOS for V-V at 28 GHz (68.3 dB compared to 61.4 dB theoretical FSPL at 1 m) and 73 GHz (79.6 dB compared to 69.7 dB theoretical FSPL at 1 m), and in some environments by more than 20 to 30 dB. This reveals that the FI model lacks a physical link to the transmitted signal power, and does not physically model what actually happens in a practical LOS or NLOS system where there are no obstructions, i.e., free space conditions, in the first several meters of propagation. Furthermore, the slope values (β) of the mean least-squares fit line in (3) are close to or less than free space ($\beta = 2$) in NLOS environments for both 28 GHz and 73 GHz with co- and cross-polarized antennas, which does not properly predict the intuitive fact that NLOS cross-polarized signals undergo much heavier attenuation with distance than free space signals. This underscores the lack of intuition provided by the FI model when trying to reconcile the physical effects of polarization and environmental loss with distance. The lack of measurements or data samples is often the cause of α and β values that make no physical sense [112], [120]. Post-processing methods that employ different thresholding techniques can also significantly change the parameters in the very sensitive FI model [112]. The results in Tables 5–7 indicate that there is little value in using a model with more than one parameter, since the difference in standard deviation between the CI and FI models is very small, in most cases less than 1 dB.

With regards to the CI path loss model, the 73 GHz band is more lossy than the 28 GHz band in indoor NLOS environments, and emphasizes the frequency dependency of path loss in indoor environments beyond the first meter of FSPL. The 73 GHz band is initially 8.4 dB more lossy in the first meter of propagation, but as seen in Table 5, at greater distances the PLE is 0.9 greater for the V-V case, indicating that 73 GHz NLOS propagation experiences an additional 9 dB per decade of distance more path loss beyond the first meter of propagation compared to 28 GHz, indicating frequency dependent path loss indoors. The smaller 73 GHz wavelength results in more diffuse scattering and greater shadowing in the physical surroundings that weaken signals when compared to 28 GHz in the NLOS indoor office environment. The carpeted floors, cubicle sound proofing, and textured wall surfaces all likely contribute to greater attenuation due to diffusion at 73 GHz.

The CI model of (1) provides the benefit of simple comparisons of measurements across many frequency bands using just one parameter, since frequency dependent effects of the model are primarily contained in the 1 m FSPL where a substantial amount of loss occurs, while the PLE value represents the environmental effects of propagation that are less sensitive to frequency than the loss in the first meter. For outdoor mmWave channels, the PLE was found to be only slightly sensitive to frequency [112]. However, Tables 5, 6, and 7 show that for indoor channels, the environment provides additional and substantial frequency-dependent loss beyond the first meter of free space propagation. Variations of the CI model as described in [3], [112], and [122] and presented here with the CIF model (6) allow the PLE to vary with frequency.

Table 8 provides the 28 GHz and 73 GHz directional multi-frequency CI, CIX, CIF, CIFX, ABG and ABGX path loss models for the directional LOS, NLOS, and NLOS-Best environments and scenarios. The multi-frequency XPD models are used for cross-polarized measurements, as they result in lower standard deviation and better minimization of σ compared to a non-XPD model, as noticed in the differences in σ when comparing the CI cross-polarized (V-H) model and CIX model for directional single frequency measurements in Table 5. The standard deviation differences for the three multi-frequency models are less than 1 dB or so of each other in LOS and NLOS environments, as shown in Table 8. The CI and CIF models have identical slope parameters (PLE and n, respectively) in LOS (1.7) and NLOS-Best (3.2) environments and differ by only 0.1 in NLOS. In the NLOS-Best environment, the ABG model has a similar slope parameter (α) compared to the CI and CIF models where the CI (PLE) and CIF (n) parameters are 3.2 and the ABG

TABLE 7. Single frequency directional FI path loss model (3) parameters for 28 GHz and 73 GHz indoor channels with TX heights of 2.5 m and RX heights of 1.5 m for both V-V and V-H antenna polarization configurations. The 28 GHz TX-RX antennas had 15 dBi (28.8° azimuth HPBW) of gain and the 73 GHz TX-RX antennas had 20 dBi (15° azimuth HPBW) of gain. "Ant. Pol." stands for antenna polarization.

Single Frequency Directional FI Path Loss Model Parameters										
Frequency	Ant. Pol.	LOS			NLOS			NLOS-best		
		α [dB]	β	σ [dB]	α [dB]	β	σ [dB]	α [dB]	β	σ [dB]
28 GHz	V-V	68.3	1.0	2.0	81.6	2.6	10.6	54.1	3.7	10.7
	V-H	94.8	0.8	1.6	92.7	2.3	8.0	73.0	3.3	8.7
73 GHz	V-V	79.6	0.7	2.3	114.0	1.3	11.3	75.6	2.9	11.7
	V-H	101.1	1.6	4.6	120.5	1.7	9.0	100.6	2.3	8.2

TABLE 8. 28 GHz and 73 GHz multi-frequency directional path loss model parameters for the CI, CIX, CIF, CIFX, ABG, and ABGX models for LOS, NLOS, and NLOS-Best environments and scenarios. The CIX, CIFX, and ABGX cross-polarized models use the corresponding parameters found for the respective co-polarized models to find the XPD factor in dB that minimizes σ. "Pol." stands for polarization configuration (either V-V or V-H).

28 GHz and 73 GHz Multi-Frequency Directional LOS Path Loss Model Parameters						
	Pol.	PLE	XPD		σ	
CI	V-V	1.7	-		2.9 dB	
CIX	V-H	1.7	28.1 dB		4.7 dB	
	Pol.	n	b	f_0	XPD	σ
CIF	V-V	1.7	-0.07	52 GHz	-	2.9 dB
CIFX	V-H	1.7	-0.07	52 GHz	28.1 dB	5.0 dB
	Pol.	α	β	γ	XPD	σ
ABG	V-V	0.9	43.6	1.8	-	2.1 dB
ABGX	V-H	0.9	43.6	1.8	27.4 dB	4.9 dB
28 GHz and 73 GHz Multi-Frequency Directional NLOS Path Loss Model Parameters						
	Pol.	PLE	XPD		σ	
CI	V-V	4.9	-		14.6 dB	
CIX	V-H	4.9	11.3 dB		13.3 dB	
	Pol.	n	b	f_0	XPD	σ
CIF	V-V	4.8	0.19	50 GHz	-	13.9 dB
CIFX	V-H	4.8	0.19	50 GHz	11.6 dB	11.8 dB
	Pol.	α	β	γ	XPD	σ
ABG	V-V	1.9	27.5	4.3	-	11.1 dB
ABGX	V-H	1.9	27.5	4.3	8.9 dB	8.7 dB
28 GHz and 73 GHz Multi-Frequency Directional NLOS-Best Path Loss Model Parameters						
	Pol.	PLE	XPD		σ	
CI	V-V	3.2	-		11.5 dB	
CIX	V-H	3.2	16.0 dB		9.6 dB	
	Pol.	n	b	f_0	XPD	σ
CIF	V-V	3.2	0.13	50 GHz	-	11.3 dB
CIFX	V-H	3.2	0.13	50 GHz	16.1 dB	9.0 dB
	Pol.	α	β	γ	XPD	σ
ABG	V-V	3.3	11.1	3.2	-	11.2 dB
ABGX	V-H	3.3	11.1	3.2	16.2 dB	8.8 dB

α parameter is 3.3. The CIX, CIFX, and ABGX LOS XPD models show that there is large polarization isolation in LOS environments, where the XPD factors are greater than 27 dB for each. The ABG and ABGX models have lower standard deviations in a majority of scenarios when compared to the CIF and CIFX models, but always by less than a dB, except for the arbitrary pointing NLOS situation, where the ABG and ABGX models have a 2 - 3 dB smaller standard deviation. To achieve this better fit, the ABG model optimizes to a nonsensical γ value of 4.3, which is an unrealistic amount of attenuation with increasing frequency. Also note that in the arbitrary pointing NLOS case, none of the models are very good, as the standard deviations for all three models are large, over 11 dB in NLOS cases, yet the CI and CIF models offer parameters that make sense physically. The ABGX and ABG models do not have a close-in free space path loss leverage point, thus these models are not tied to the true transmitted power, and as shown in [112], [122], are much less stable or accurate compared to models that use a free-space reference distance when used outside the measurement range for which the model parameters were optimized. The standard deviations of multi-frequency path loss models for similar environments in Table 8 show just how closely the different directional models predict path loss, with little difference in standard deviations observed for most cases (a majority differ by less than 1 dB, with differences less than an order of magnitude than the standard deviation of the models). The small differences in standard deviation and added intuition and stability suggest that the simpler, physics-based CI, CIX, CIF, and CIFX models may be better suited for closed-form analysis as well as standards work when developing future mmWave indoor networks. As shown subsequently, the omnidirectional path loss models reveal even smaller differences between the CIF and ABG models.

D. OMNIDIRECTIONAL PATH LOSS MODELS FOR CO- AND CROSS-POLARIZED ANTENNAS

While the preceding directional path loss models are useful for wireless systems using directional antennas [124], [129], [130], standards bodies rely on omnidirectional path loss models to allow arbitrary antenna patterns to be used for simulations. In order to synthesize an omnidirectional path loss model from directional measurements, the antenna radiation patterns used during measurements must be de-embedded or removed from the results [131]. This can be achieved by summing received powers (in the linear scale) from unique, non-overlapping pointing angle directional measurements (from adjacent angular bins) after subtracting the antennas gains, as

IEEE Access
The journal for rapid open access publishing

TABLE 9. Path loss environment definitions for omnidirectional path loss models.

Setting	Description
LOS	Path loss when there is a clear optical path between the TX and RX.
NLOS	Path loss when the TX and RX are separated by obstructions and there is no clear optical path between the antennas.

implemented in [132] and [133]. Since the measurement sweeps included antenna pointing directions separated by approximately one antenna HPBW in the azimuth and elevation planes, the summed directions are virtually orthogonal to each other in space, thereby avoiding over-counting of received power or multipath energy [112], [133]. The raw omnidirectional path loss data used to generate the omnidirectional path loss models presented in this paper are provided in tabular form in Appendix B.

The same method used in [132] was performed on the 28 GHz and 73 GHz indoor directional data, where for each TX-RX location pair, the omnidirectional path loss between the i^{th} TX location and the j^{th} RX location was recovered from individual and non-overlapping pointing angle received powers in the azimuth and elevation planes following [112], [132], [133]:

$$\mathrm{PL}_{i,j}[\mathrm{dB}] = \mathrm{Pt}_{i,j}[\mathrm{dBm}] - 10\log_{10}\left[\sum_{z}\sum_{y}\sum_{x}\sum_{w}\mathrm{Pr}_{i,j}\left(\theta_{r_w}, \phi_{r_x}, \theta_{t_y}, \phi_{t_z}\right)[\mathrm{mW}]\right] \tag{8}$$

where θ_t and ϕ_t are the TX antenna pointing angles in the azimuth and elevation planes, respectively, θ_r and ϕ_r are the RX antenna pointing angles in the azimuth and elevation planes, where $\mathrm{Pt}_{i,j}$ is the omnidirectional transmit power, and the $\mathrm{Pr}_{i,j}$ values are the individual directional received powers from the unique pointing angles, with the antenna gains removed. The individual directional received powers were found from the PDPs recorded for each unique antenna pointing angle, where power is the area under each PDP. To ensure consistency with the omnidirectional path loss models presented in [112] and [132], the same descriptors of physical environments for omnidirectional path loss models were used in this article and are defined in Table 9.

Figs. 4a – 4d display the CI ($d_0 = 1$ m) and FI omnidirectional scatter plots and path loss models at 28 GHz and 73 GHz for LOS and NLOS indoor office environments with separate V-V and V-H antenna polarization configurations. Table 10 lists the omnidirectional CI and FI path loss model parameters. Table 11 gives the CIX model parameters for the V-H omnidirectional cross-polarization scenarios. The tables show that in LOS environments, the V-V CI model omnidirectional PLE is 1.1 and 1.3 at 28 GHz and 73 GHz, respectively. Similar to the directional V-V CI models, the omnidirectional PLEs are less than theoretical free space path loss ($n = 2$), and not surprisingly show significantly lower loss than the directional LOS channels. In NLOS environments for V-V antennas, the omnidirectional PLE is 2.7 and 3.2 at 28 GHz and 73 GHz, respectively, showing higher path loss at 73 GHz than at 28 GHz, likely due to increased diffuse scattering with shorter wavelengths at higher frequencies [7]. The NLOS directional V-V PLEs are 4.4 and 5.3 at 28 GHz and 73 GHz, respectively, compared to the omnidirectional values of 2.7 and 3.2 at 28 GHz and 73 GHz, respectively, showing that omnidirectional antennas would capture more energy than directional antennas, but offer less link margin (less distance range due to smaller antenna gain) [112], [133].

For cross-polarized antennas, the 28 GHz LOS (V-H PLE = 2.5) and NLOS (V-H PLE = 3.6) CIX omnidirectional models resulted in attenuation XPD factors of 14.0 dB and 10.4 dB, respectively. The LOS and NLOS V-H PLEs for 73 GHz are 3.5 (XPD = 22.8 dB) and 4.5 (XPD = 15.4 dB), respectively, also indicating higher path loss at 73 GHz as well as greater polarization discrimination. Similar to the directional path loss models, for omnidirectional LOS channels, a lumped cross-polarization attenuation factor used in (2) yields a simple CIX path loss model with lower standard deviation (better fit) about the distance-dependent mean path loss compared to a traditional CI model for cross-polarized path loss data.

The 14.0 dB and 10.4 dB omnidirectional XPD factors in LOS and NLOS at 28 GHz may be sufficient for indoor systems to implement simultaneous dual antenna polarization transmission [134], [135], depending on the modulation scheme used, and with interference cancellation methods that may allow for simultaneous transmissions of cross-polarized signals, however, this needs to be further investigated. The 73 GHz LOS and NLOS XPD factors of 22.8 dB and 15.4 dB are substantially larger than those at 28 GHz and yield remarkable polarization isolation for 73 GHz diversity polarization transmission in indoor environments. The results show that NLOS environments experience higher path loss which results in a lower XPD factor compared to LOS [47].

The FI omnidirectional models at 28 GHz and 73 GHz both have intercept α values in LOS environments that are several dB offset from theoretical free space at 1 m at the respective frequencies. The very low LOS β slope value of 0.5 at 73 GHz shows the extreme sensitivity of the FI model and how the model parameters defy physical interpretation (where a PLE value of 0.5 indicates little increase in path loss as distance increases, which is unrealistic). This illustrates the caution that must be taken when using the FI model to extrapolate path loss outside of the measurement range.

The small LOS β slope values may be due to the small sample set of LOS locations. The strength of the CI model compared to the FI model is that it only requires a single parameter to accurately predict path loss, and models FSPL up until the reference distance d_0, giving an accurate physically-based reference anchor point for estimating LOS path loss. Choosing $d_0 = 1$ m is convenient and

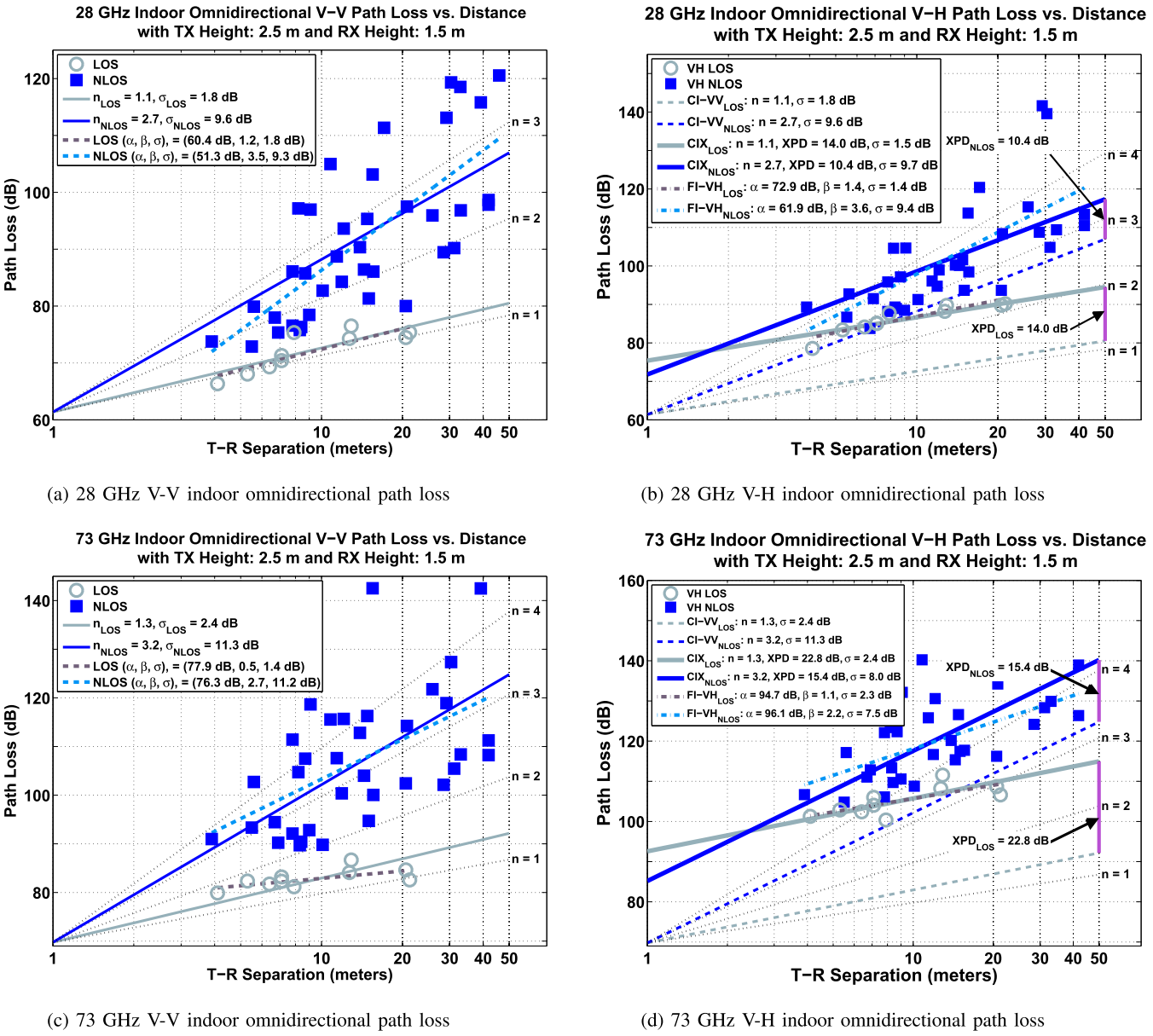

(a) 28 GHz V-V indoor omnidirectional path loss

(b) 28 GHz V-H indoor omnidirectional path loss

(c) 73 GHz V-V indoor omnidirectional path loss

(d) 73 GHz V-H indoor omnidirectional path loss

FIGURE 4. Single frequency 28 GHz and 73 GHz indoor omnidirectional CI ($d_0 = 1$ m) and FI path loss scatter plots and models with TX antenna heights of 2.5 m and RX antenna heights of 1.5 m in a typical office environment for co- and cross-polarized TX and RX antennas. Gray circles represent LOS omnidirectional path loss values and solid blue squares represent NLOS omnidirectional path loss values, using Eq. (8). (a) 28 GHz V-V; (b) 28 GHz V-H; (c) 73 GHz V-V; and (d) 73 GHz V-H.

sensible because FSPL exists in the first meter of propagation, before the transmitted wave encounters most walls, ceilings, and floors that cause reflections, scattering, or diffraction loss (blockage). If more LOS omnidirectional locations were measured, we would expect the FI β slope to converge to the CI PLE values in LOS environments (1.1 and 1.3 at 28 GHz and 73 GHz, respectively), as shown in the 28 GHz LOS V-V model displayed in Fig. 4a, where the CI PLE and FI β values are within 0.1 of each other.

Some researchers may correctly argue that the two-parameter FI model (3) reduces the shadow factor (standard deviation) about the mean path loss line compared to the shadow factor found using the single-parameter CI path loss model (1). That argument may be true in very sparse measurement data sets, but when enough measurements are taken, the standard deviations are generally within a fraction of a dB for both models as seen in Table 10 and [112]. From this study, Table 10 shows that there are only three cases (all cross-polarized cases) where the standard deviation is more than 1 dB different between the CI and FI omnidirectional models: the 73 GHz V-H NLOS case, and the 28 GHz and 73 GHz LOS V-H cases, where the standard deviation is different by 2.2 dB, 1.6 dB and 4.0 dB, respectively, yet we have already established that the CIX model with an

IEEE Access
The journal for rapid open access publishing

TABLE 10. Single frequency omnidirectional CI path loss model parameters with $d_0 = 1$ m and FI path loss model parameters for 28 GHz and 73 GHz indoor propagation channels with TX heights of 2.5 m and RX heights of 1.5 m for both V-V and V-H antenna polarization configurations for LOS and NLOS environments. "Freq." stands for carrier frequency, "Pol." stands for TX-RX antenna polarization configuration, and "Env." stands environment.

Single Frequency Omnidirectional CI and FI Path Loss Models							
Freq.	Pol.	Env.	CI: $d_0 = 1$ m		FI		
			PLE	σ [dB]	α [db]	β	σ [dB]
28 GHz	V-V	LOS	1.1	1.8	60.4	1.2	1.8
		NLOS	2.7	9.6	51.3	3.5	9.3
	V-H	LOS	2.5	3.0	72.9	1.4	1.4
		NLOS	3.6	9.4	61.9	3.6	9.4
73 GHz	V-V	LOS	1.3	2.4	77.9	0.5	1.4
		NLOS	3.2	11.3	76.3	2.7	11.2
	V-H	LOS	3.5	6.3	94.7	1.1	2.3
		NLOS	4.5	9.7	96.1	2.2	7.5

TABLE 11. Single frequency omnidirectional CIX path loss model parameters with $d_0 = 1$ m for 28 GHz and 73 GHz indoor channels with TX heights of 2.5 m and RX heights of 1.5 m for V-H antenna polarization configurations. The 28 GHz TX and RX antennas had 15 dBi (28.8° azimuth HPBW) of gain and the 73 GHz TX and RX antennas had 20 dBi (15° azimuth HPBW) of gain. "Freq." stands for carrier frequency and "Pol." stands for TX-RX antenna polarization configuration.

Single Frequency Omnidirectional CIX Path Loss Models for $d_0 = 1$ m							
Freq.	Pol.	LOS			NLOS		
		$n_{(V\text{-}V)}$	XPD [dB]	$\sigma_{(XPD)}$ [dB]	$n_{(V\text{-}V)}$	XPD [dB]	$\sigma_{(XPD)}$ [dB]
28 GHz	V-H	1.1	14.0	1.5	2.7	10.4	9.7
73 GHz	V-H	1.3	22.8	2.4	3.2	15.4	8.0

TABLE 12. 28 GHz and 73 GHz multi-frequency omnidirectional path loss model parameters for the CI, CIX, CIF, CIFX, ABG, and ABGX models for LOS and NLOS environments. The CIX, CIFX, and ABGX cross-polarized models use the corresponding parameters found for the respective co-polarized models to find the XPD factor in dB that minimizes σ. "Pol." stands for polarization configuration (either V-V or V-H).

28 GHz and 73 GHz Multi-Frequency Omnidirectional LOS Path Loss Model Parameters						
	Pol.	PLE	XPD		σ	
CI	V-V	1.2	-		2.3 dB	
CIX	V-H	1.2	18.4 dB		5.7 dB	
	Pol.	n	b	f_0	XPD	σ
CIF	V-V	1.2	0.18	51 GHz	-	2.1 dB
CIFX	V-H	1.2	0.18	51 GHz	18.4 dB	4.8 dB
	Pol.	α	β	γ	XPD	σ
ABG	V-V	0.9	26.8	2.6	-	1.8 dB
ABGX	V-H	0.9	26.8	2.6	18.2 dB	4.7 dB
28 GHz and 73 GHz Multi-Frequency Omnidirectional NLOS Path Loss Model Parameters						
	Pol.	PLE	XPD		σ	
CI	V-V	2.9	-		10.9 dB	
CIX	V-H	2.9	12.6 dB		10.4 dB	
	Pol.	n	b	f_0	XPD	σ
CIF	V-V	3.0	0.21	50 GHz	-	10.4 dB
CIFX	V-H	3.0	0.21	50 GHz	12.7 dB	9.3 dB
	Pol.	α	β	γ	XPD	σ
ABG	V-V	3.1	1.3	3.8	-	10.3 dB
ABGX	V-H	3.1	1.3	3.8	12.9 dB	9.0 dB

XPD term in (2) is a better estimator of path loss for V-H antenna configurations than either the CI or FI model (Compare Table 10 and Table 11). Furthermore, the CIX model provides nearly identical standard deviations compared to the FI model, where the maximum difference in standard deviation of both models over all frequencies and environments is 0.5 dB. Important points to consider are that all models here have rather large standard deviations (8 dB or so), so selecting a simpler path loss model that has fewer parameters with less than a dB of difference in standard deviation assures virtually identical modeling accuracy in the face of typical measurement error, physical positioning error, ray-tracing database error, and cable and calibration fluctuations [112]. Further, in the absence of measured data, the physical foundation of the CI family of path loss models allows for extrapolation beyond the 3D T-R separation distances of the measurements because they are physically-anchored to a known free space (true transmitter power) path loss value and distance, whereas the FI models are only valid over the measured 3D T-R separation distances [122].

A key observation from the omnidirectional path loss data is the pronounced increase in the PLE for 73 GHz compared to 28 GHz for any given environment, due to the increased path loss experienced by signals with smaller wavelengths. The standard deviation also increased at 73 GHz compared to 28 GHz for the omnidirectional models, as seen in Tables 10–11. Due to a more stringent noise thresholding algorithm used here and described in [112], values in Table 10 are slightly different than those presented in [109]. The differences in the CI, FI, and CIX model standard deviations in Tables 10–11 are 1 dB or less in a majority of the different environments and scenarios, while the overall standard deviations are much larger (greater than 8 dB in NLOS cases).

Multi-frequency omnidirectional path loss model parameters for co- and cross-polarized antennas are given in Table 12. Similar to the directional models, the standard deviations for each omnidirectional multi-frequency model with specific polarizations (CI, CIF, and ABG) are within 1 dB for the corresponding LOS and NLOS environments (σ is between 1.8 dB and 2.3 dB in LOS and between 10.3 dB and 10.9 dB in NLOS for the CI, CIF, and ABG models). The FSPL anchoring point is an advantage in the CI and CIF models, where in LOS environments, the CI PLE and CIF n values are identical (1.2), and 2.9 and 3.0 in NLOS, respectively. The advantage of the two-parameter CIF model over the single-parameter CI model is the frequency weighting term b on the PLE, to account for frequency-dependent loss with distance, which results in a lower standard deviation of 2.1 dB (CIF) compared to 2.3 dB (CI) in LOS, and 10.4 dB (CIF) compared to 11.5 dB (CI) in NLOS. The CI and

TABLE 13. Single frequency combined polarization directional path loss models at 28 GHz and 73 GHz for LOS, NLOS, and NLOS-Best scenarios.

Single Frequency Combined Polarization Directional CI Path Loss Models with $d_0 = 1$ m						
Freq.	LOS		NLOS		NLOS-best	
	PLE	σ [dB]	PLE	σ [dB]	PLE	σ [dB]
28 GHz	2.9	13.3	4.8	11.9	3.0	10.8
73 GHz	3.1	16.8	5.7	16.7	3.4	11.8

Single Frequency Combined Polarization Directional FI Path Loss Models									
Freq.	LOS			NLOS			NLOS-best		
	α [dB]	β	σ [dB]	α [dB]	β	σ [dB]	α [dB]	β	σ [dB]
28 GHz	4.1 m $\leq d \leq$ 21.3 m			3.9 m $\leq d \leq$ 45.9 m					
	83.4	0.8	12.2	87.5	2.4	10.1	54.1	3.7	10.7
73 GHz	4.1 m $\leq d \leq$ 21.3 m			3.9 m $\leq d \leq$ 41.9 m					
	94.5	0.7	15.8	117.8	1.3	11.7	75.6	2.9	11.7

CIF models for co-polarized antennas are always well within 1 dB of the three-parameter ABG model standard deviation, and the 1 dB reduction in standard deviation is less than an order of magnitude than the standard deviation of either model, thus motivating the use of a simpler model (i.e. fewer parameters) given the lack of substantial model improvement when using more parameters and a non-physically-based model [112]. From Table 12, it is also seen that the LOS standard deviations are 5.7 dB, 4.8 dB, and 4.7 dB for the CIX, CIFX, and ABGX models, respectively.

E. DIRECTIONAL PATH LOSS MODELS FOR COMBINED POLARIZATIONS

In order to characterize path loss regardless of polarization, the co- and cross-polarization measurements were lumped into a single dataset for 28 GHz and 73 GHz to generate large-scale path loss models that may be applied to arbitrary antenna polarizations, a common practice in standards bodies. Table 13 provides the single frequency directional path loss models using combined co- and cross-polarization measurement data at 28 GHz and 73 GHz for the LOS, NLOS, and NLOS-Best scenarios. When considering the single strongest pointing angle combination for each specific T-R separation distance, as compared with arbitrary pointing angles in NLOS conditions, Table 13 shows that the PLE reduces by 18 dB and 23 dB per decade of distance for 28 GHz and 73 GHz, respectively. In LOS, the FI β values are lower than 1 (0.8 and 0.7 for 28 GHz and 73 GHz, respectively) and thus lack a sensible intuitive explanation based on physics. In the NLOS-Best scenario, the β values are larger (3.7 and 2.9 at 28 GHz and 73 GHz, respectively) than the corresponding β values for the FI NLOS model (2.4 and 1.3 at 28 GHz and 73 GHz, respectively) also contradicting physical intuition for propagation as a function of distance when considering the lowest path loss measured for the best antenna pointing angles at the TX and RX for each measurement location.

Table 14 lists the 28 GHz and 73 GHz multi-frequency combined polarization directional path loss model parameters for the LOS, NLOS, and NLOS-Best scenarios. In

TABLE 14. 28 GHz and 73 GHz multi-frequency combined polarization directional path loss models for LOS, NLOS, and NLOS-Best scenarios.

28 GHz and 73 GHz Multi-Frequency Combined Polarization Directional CI Path Loss Models with $d_0 = 1$ m		
Env.	PLE	σ [dB]
LOS	3.0	15.2
NLOS	5.2	15.5
NLOS-Best	3.2	11.5

28 GHz and 73 GHz Multi-Frequency Combined Polarization Directional CIF Path Loss Models with $d_0 = 1$ m				
Env.	n	b	f_0	σ [dB]
LOS	3.0	0.07	51 GHz	15.2
NLOS	5.2	0.21	50 GHz	14.5
NLOS-Best	3.2	0.13	50 GHz	11.3

28 GHz and 73 GHz Multi-Frequency Combined Polarization Directional ABG Path Loss Models with $d_0 = 1$ m				
Env.	α	β	γ	σ [dB]
LOS	0.7	47.1	2.5	14.2
NLOS	1.9	27.5	4.5	11.0
NLOS-Best	3.3	11.1	3.2	11.2

all three scenarios, the CI PLE and CIF n values are identical, 3.0 in LOS, 5.2 in NLOS, and 3.2 for NLOS-Best. This result shows the consistency of using a FSPL anchor grounded in true physics for path loss modeling. The CIF model reduces the standard deviation only slightly in the NLOS and NLOS-Best scenarios, by only 1.0 dB and 0.2 dB respectively, and is identical in LOS (15.2 dB). A difference of 1.1 dB or 0.2 dB is much smaller than the actual standard deviation value of 15.5 dB (CI-NLOS) and 14.5 dB (CIF-NLOS), and 11.5 dB (CI-NLOS-Best) and 11.3 dB (CIF-NLOS-Best), as shown in Table 14. For the ABG model, the α and β terms are seen to vary over a wide range of values that do not provide intuitive sense. Table 14 does show that the ABG model for LOS, NLOS, and NLOS-best has lower standard deviation than both the CI and CIF models, but the reduction is so small (a few dB to a fraction of a dB) compared to the overall standard deviation values which are all greater than 11 dB. Figs 5a and 5b show the LOS and NLOS CIF and ABG directional path loss models for combined polarizations. Note that the CIF model standard deviation

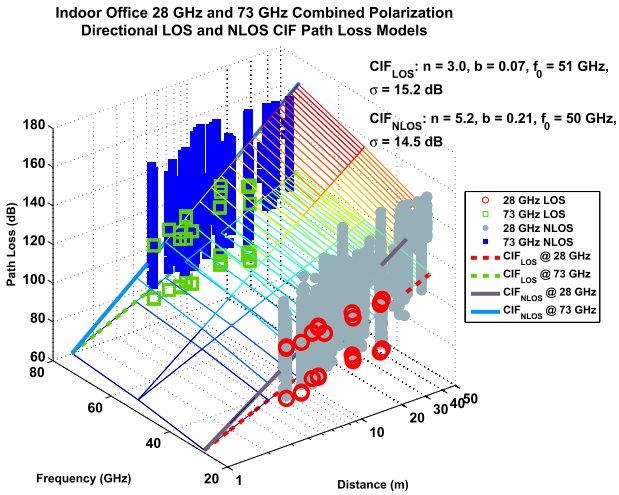

(a) Multi-frequency combined polarization directional CIF LOS and NLOS scatter plot

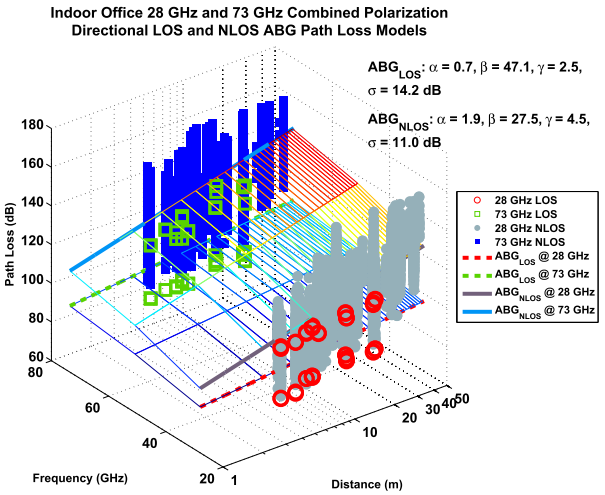

(b) Multi-frequency combined polarization directional ABG LOS and NLOS scatter plot

FIGURE 5. 28 GHz and 73 GHz multi-frequency combined polarization CIF and ABG directional path loss models for LOS and NLOS environments. Red circles represent 28 GHz LOS directional path loss values, green squares represent 73 GHz LOS directional path loss values, solid gray circles represent 28 GHz NLOS directional path loss values, and solid blue squares represent 73 GHz NLOS directional path loss values for (a) CIF Model; (b) ABG Model.

is within 0.4 dB of the ABG model in the NLOS-Best scenario, a very tiny difference achieved using one less model parameter. For the NLOS arbitrary pointing angle case, the standard deviation for the ABG model is 3.5 dB smaller than the CIF model, reducing it from 14.5 dB to 11 dB through the use of three modeling parameters, but Table 14 shows that the ABG model parameters vary over a wide range without intuition of the physics, and in the other cases (LOS and NLOS-Best) the differences in standard deviation between the CIF and ABG models are less than a dB, less than an order of magnitude of standard deviation values of all models, and certainly within typical measurement error. As shown subsequently, the CIF and ABG models are even closer in performance (a fraction of a dB difference in standard deviation, well within typical measurement error from cable flexing, pointing errors, or temperature variations) for omnidirectional path loss modeling.

F. OMNIDIRECTIONAL PATH LOSS MODELS FOR COMBINED POLARIZATIONS

Using the synthesized omnidirectional path loss values described here, and given in Appendix B, omnidirectional path loss models were computed for single and multi-frequency cases at 28 GHz and 73 GHz with the co- and cross-polarized measurements lumped into a common dataset. Table 15 provides combined polarization single frequency path loss model parameters at 28 GHz and 73 GHz and Figs. 6a and 6b display the corresponding 28 GHz and 73 GHz scatter plots. It is apparent that the 28 GHz and 73 GHz NLOS CI model standard deviations are within 1 dB of the respective NLOS FI models, well within measurement error, and less than an order of magnitude than the actual standard deviations, where the CI model

TABLE 15. 28 GHz and 73 GHz single frequency combined polarization CI and FI omnidirectional path loss models for LOS and NLOS environments.

Single Frequency Combined Polarization Omnidirectional CI Path Loss Models with $d_0 = 1$ m				
Freq.	LOS		NLOS	
	PLE	σ [dB]	PLE	σ [dB]
28 GHz	1.8	7.3	3.1	10.9
73 GHz	2.4	12.0	3.8	12.9

Single Frequency Combined Polarization Omnidirectional FI Path Loss Models						
Freq.	LOS			NLOS		
	α [dB]	β	σ [dB]	α [dB]	β	σ [dB]
28 GHz	4.1 m $\leq d \leq$ 21.3 m			3.9 m $\leq d \leq$ 45.9 m		
	66.7	1.3	7.2	58.0	3.4	10.9
73 GHz	4.1 m $\leq d \leq$ 21.3 m			3.9 m $\leq d \leq$ 41.9 m		
	86.3	0.8	11.3	88.1	2.2	12.1

requires only one parameter and uses a physically-based FSPL anchoring point. The FI model 73 GHz LOS slope value β (0.8) indicates a channel with extremely low loss, showing the lack of fundamental physics in the FI model. The FI model is limited as it is only valid over the measurement range of the data, which is between 4.1 m and 21.3 m in LOS at 28 GHz and 73 GHz, and between 3.9 m to 45.9 m in NLOS at 28 GHz and 3.9 m to 41.9 m in NLOS at 73 GHz.

All co- and cross-polarized omnidirectional measurement data at 28 GHz and 73 GHz were combined and used to develop the combined polarization CI, CIF, and ABG omnidirectional multi-frequency path loss models as provided in Table 16. The CI and CIF models show stability with the use of a FSPL anchoring point grounded in true physics, such that the CI PLE and CIF n values are identical in LOS (2.1)

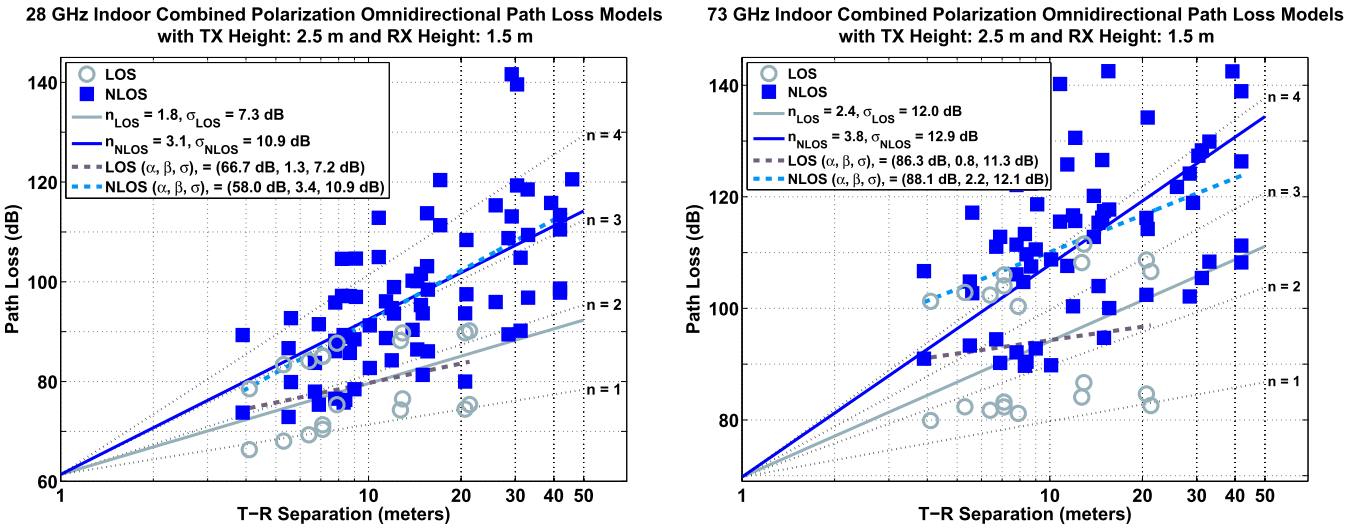

(a) 28 GHz omnidirectional combined polarization path loss

(b) 73 GHz omnidirectional combined polarization path loss

FIGURE 6. 28 GHz and 73 GHz single frequency combined polarization CI and FI omnidirectional path loss models for LOS and NLOS environments. Gray circles represent LOS omnidirectional path loss values and solid blue squares represent NLOS omnidirectional path loss values for (a) 28 GHz; (b) 73 GHz.

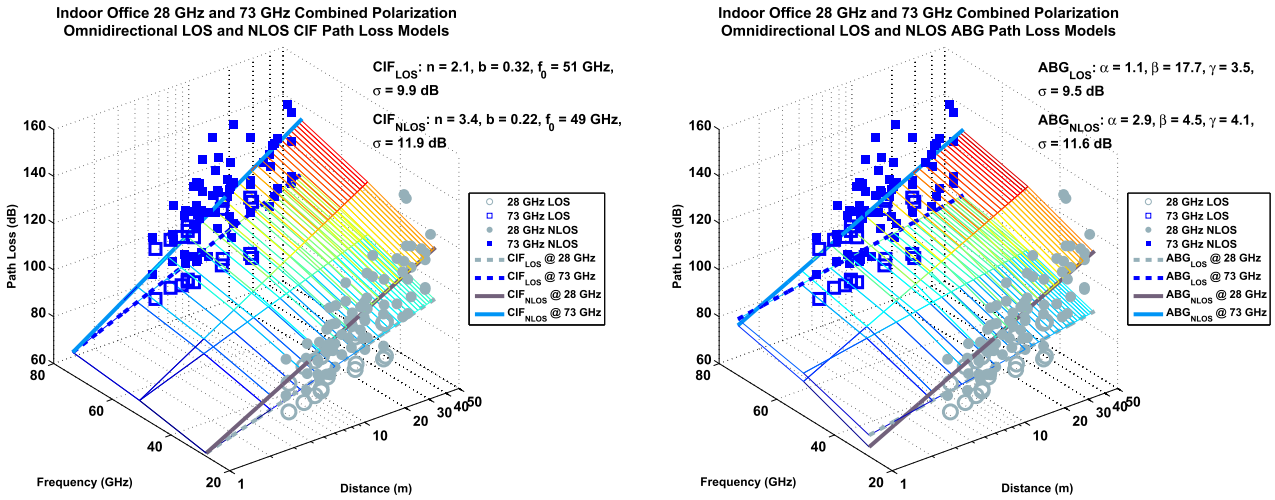

(a) Multi-frequency combined polarization omnidirectional CIF LOS and NLOS path loss

(b) Multi-frequency combined polarization omnidirectional ABG LOS and NLOS path loss

FIGURE 7. 28 GHz and 73 GHz multi-frequency combined polarization CIF and ABG omnidirectional path loss models for LOS and NLOS environments. Gray circles represent 28 GHz LOS omnidirectional path loss values, blue squares represent 73 GHz LOS omnidirectional path loss values, solid gray circles represent 28 GHz NLOS omnidirectional path loss values, and solid blue squares represent 73 GHz NLOS omnidirectional path loss values for (a) CIF Model; (b) ABG Model.

and NLOS (3.4) environments. As observed for the co- and cross-polarized multi-frequency omnidirectional models, the omnidirectional CIF models using all co- and cross-polarized measurements also have lower standard deviations than the CI models, but only by 0.5 dB and 0.6 dB in LOS and NLOS environments, respectively, due to the model's second parameter, the frequency-dependent balancing term *b*. The three-parameter ABG model has the lowest standard deviation in LOS and NLOS compared to the CI and CIF models, but by only a fraction of a dB in both environments (a very small improvement, considering the standard deviations for all models are about 11 dB). Comparatively, the standard deviation in LOS is 10.4 dB for CI, 9.9 dB for CIF, and 9.5 dB for the ABG model, not a large difference for standard deviations that are already greater than 9 dB. Furthermore, the standard deviation in NLOS is 12.5 dB for CI, 11.9 dB for CIF, and 11.6 dB for the ABG model, also within measurement errors and typical cable loss variations or gain drift in typical measurements, and not a vast difference for already large standard deviations. Figs. 7a and 7b show the 3D scatter plots of combined polarization omnidirectional LOS and NLOS

IEEE Access
The journal for rapid open access publishing

TABLE 16. 28 GHz and 73 GHz multi-frequency combined polarization CI, CIF, and ABG omnidirectional path loss models for LOS and NLOS environments.

28 GHz and 73 GHz Multi-Frequency Combined Polarization Omnidirectional CI Path Loss Models with $d_0 = 1$ m				
Env.	PLE		σ [dB]	
LOS	2.1		10.4	
NLOS	3.4		12.5	
28 GHz and 73 GHz Multi-Frequency Combined Polarization Omnidirectional CIF Path Loss Models with $d_0 = 1$ m				
Env.	n	b	f_0	σ [dB]
LOS	2.1	0.32	51 GHz	9.9
NLOS	3.4	0.22	49 GHz	11.9
28 GHz and 73 GHz Multi-Frequency Combined Polarization Omnidirectional ABG Path Loss Models with $d_0 = 1$ m				
Env.	α	β	γ	σ [dB]
LOS	1.1	17.7	3.5	9.5
NLOS	2.9	4.5	4.1	11.6

path loss values and the corresponding CIF and ABG path loss models, where the CIF model is anchored by FSPL at 1 m. Both figures show a similar trend as path loss increases with frequency. The combined polarization omnidirectional path loss models given in Tables 15 and 16 also show comparable standard deviations in LOS and NLOS environments between the CI and FI single frequency models and the CI, CIF, and ABG multi-frequency models, where differences in standard deviations are less than an order of magnitude of the standard deviation, and less than or equal to 1 dB in all cases.

From the large-scale path loss models and parameters shown above, it is apparent that the single frequency CI model does an excellent job in predicting indoor path loss at individual mmWave frequencies by using a single parameter. For multiple-frequency omnidirectional modeling, it is clear that indoor channels offer greater loss with distance at higher frequencies. The work above shows that the two-parameter CIF model retains a physical link to the physics of propagation while reducing the standard deviation as compared to the CI model. The three-parameter ABG model can typically obtain a fraction of a dB to a dB or two less standard deviation but at the expense of an additional model parameter and a lack of physical basis. Thus, the CIF model appears to be a good candidate for indoor large-scale path loss modeling over a wide range of mmWave frequencies.

V. mmWave INDOOR TIME DISPERSION PROPERTIES

The time dispersion properties of wideband channels are generally characterized by RMS delay spread, as it is a good measure of the multipath time dispersion and coherence bandwidth nature of multipath channels, and an indication of the potential severity of intersymbol interference, depending on the signal's bandwidth [73], [136], [137]. To build power-efficient mmWave mobile communications systems with simple equalization, it was recently postulated that there could be advantages in searching for particular beam pointing directions that offer both minimum path loss and minimum multipath delay spread [124]. Physical layer design is often dictated by channel RMS delay spread and other time dispersion characteristics, and analysis of such properties can provide valuable information for the design of indoor mmWave communications systems. All RMS delay spread and temporal statistics presented in this section are for typical LOS and NLOS environments.

TABLE 17. Comparison of mean, standard deviation, minimum, and maximum RMS delay spreads at 28 GHz and 73 GHz for V-V and V-H antenna polarization combinations in LOS and NLOS indoor propagation environments. "Ant. Pol." means TX-RX antenna polarization and "Env." indicates the environment type of the RX locations.

RMS Delay Spreads Over All Arbitrary Angles					
Ant. Pol.	Env.	28 GHz			
		μ (ns)	σ (ns)	Min. (ns)	Max. (ns)
V-V	LOS	17.3	18.0	0.7	134.4
	NLOS	17.7	13.8	0.6	198.5
	LOS-Best	4.1	1.6	1.6	6.1
	NLOS-Best	13.4	13.1	0.9	47.9
V-H	LOS	17.2	14.5	0.9	126.4
	NLOS	18.0	10.9	0.6	128.1
	LOS-Best	7.3	3.5	4.2	14.6
	NLOS-Best	13.2	10.8	3.5	55.7
Ant. Pol.	Env.	73 GHz			
		μ (ns)	σ (ns)	Min. (ns)	Max. (ns)
V-V	LOS	12.8	16.9	0.6	101.9
	NLOS	12.3	14.2	0.5	142.0
	LOS-Best	3.6	1.5	0.8	5.1
	NLOS-Best	11.3	14.4	3.7	73.4
V-H	LOS	11.4	17.5	0.5	143.8
	NLOS	8.4	10.6	0.5	122.2
	LOS-Best	7.0	10.9	0.8	37.7
	NLOS-Best	12.5	22.5	2.2	122.2

The RMS delay spread is defined as the square root of the second moment of a PDP [73]:

$$\sigma_\tau = \sqrt{\overline{\tau^2} - (\bar{\tau})^2} \tag{9}$$

where,

$$\bar{\tau} = \frac{\sum_k P(\tau_k)\tau_k}{\sum_k P(\tau_k)} \tag{10}$$

$$\overline{\tau^2} = \frac{\sum_k P(\tau_k)\tau_k^2}{\sum_k P(\tau_k)} \tag{11}$$

In Eqs. (9)-(11), σ_τ is the RMS delay spread, $P(\tau_k)$ is the received power (in mW) at the delay bin centered at τ_k, $\bar{\tau}$ is the mean excess delay which is the first moment of a PDP, and $\overline{\tau^2}$ is the second central moment of a PDP. We captured a PDP at each unique antenna pointing angle between the TX and RX in the azimuth and elevation planes, for all measured TX and RX pointing angles where energy was detectable, for each TX-RX location combination.

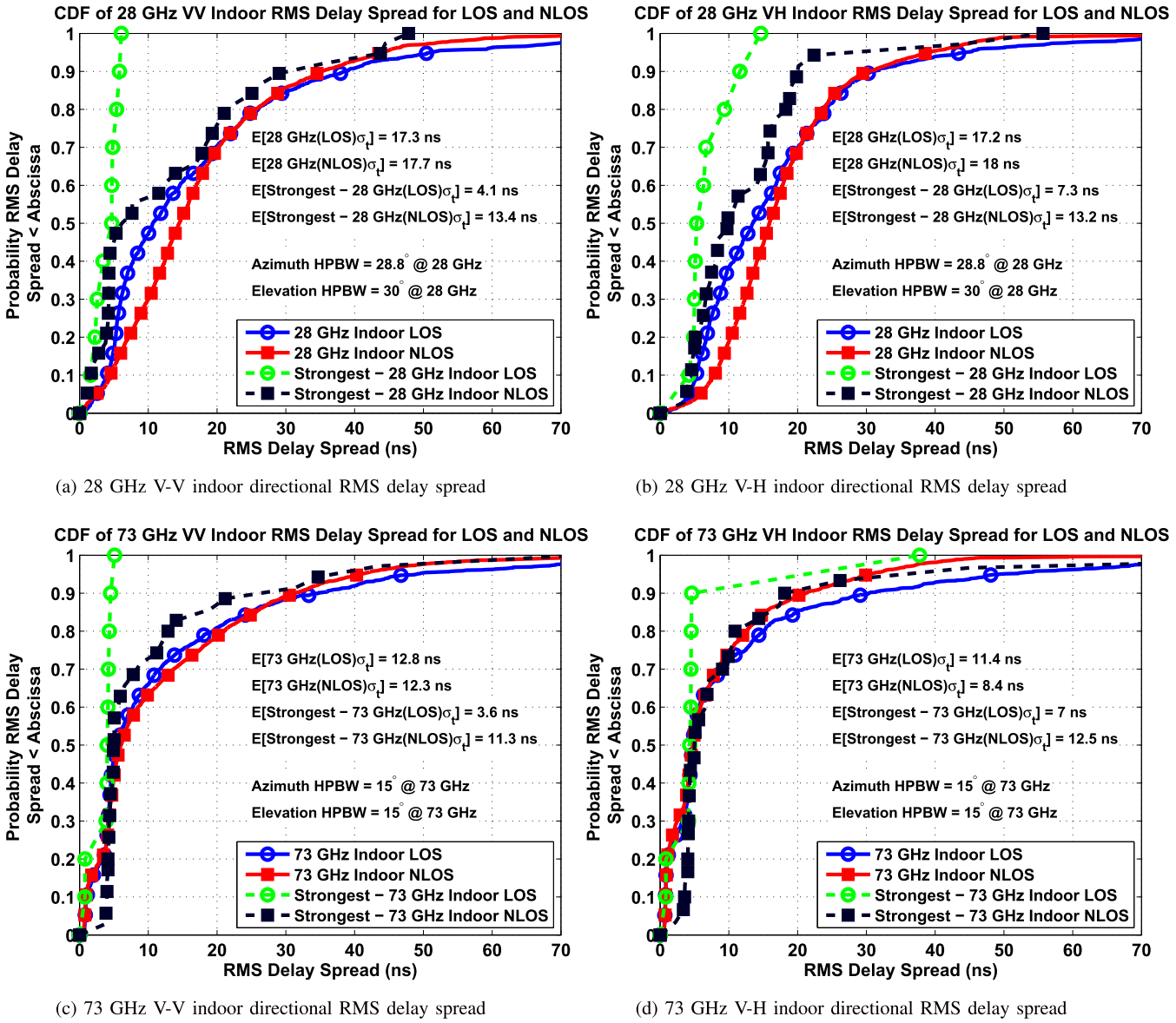

(a) 28 GHz V-V indoor directional RMS delay spread

(b) 28 GHz V-H indoor directional RMS delay spread

(c) 73 GHz V-V indoor directional RMS delay spread

(d) 73 GHz V-H indoor directional RMS delay spread

FIGURE 8. **28 GHz and 73 GHz arbitrary pointing angle (directional) RMS delay spread CDFs for TX antenna heights of 2.5 m and RX antenna heights of 1.5 m in a typical indoor office environment for co- and cross-polarized TX and RX antennas in LOS and NLOS environments. The T-R separation distances ranged from 3.9 m to 45.9 m. (a) 28 GHz V-V; (b) 28 GHz V-H; (c) 73 GHz V-V; and (d) 73 GHz V-H.**

A. MULTIPATH TIME DISPERSION STATISTICS FOR CO- OR CROSS-POLARIZED ANTENNAS

Figs. 8a and 8b show the cumulative distribution functions (CDF) for the RMS delay spreads of the PDPs measured over all pointing angles at 28 GHz for V-V and V-H antenna polarization configurations, respectively. Both figures show that 90% of the measured RMS delay spreads in both LOS and NLOS environments are less than 40 ns for all measured arbitrary pointing angles. The NLOS locations were generally found to have greater RMS delay spreads than LOS locations, since obstructions in NLOS locations blocked or severely attenuated the direct path, causing multipath to arrive at the receiver over a larger propagation time interval. In LOS environments, the LOS component was much stronger than reflected or scattered paths, leading to lower RMS delay spreads. Similar trends were observed in propagation measurements below 6 GHz, conducted by Hashemi *et al.* in two office environments [137]. The mean RMS delay spread was smaller in LOS environments (where the direct path was dominant) compared to NLOS environments (where the direct path was obstructed). Similar RMS delay spread statistics at 60 GHz were reported by Geng *et al.*, where RMS delay spreads in a NLOS hall were larger than in either a LOS hall or corridor [82].

The measured mean RMS delay spreads at 28 GHz are between 17 ns and 18 ns in all environments and polarization combinations (as summarized in Table 17), which in general are larger than the mean RMS delay spreads between 8 ns and 13 ns at 73 GHz. Similar results were reported by Yang *et al.* where the mean RMS delay spreads at 58 GHz

(8 ns to 14 ns) were about 50% lower than those at 2.25 GHz (20 ns to 28 ns) due to high penetration loss caused by walls, such that multipath components observed at 58 GHz came mostly from reflected waves confined to the room, while the reflected waves from neighboring rooms at 2.25 GHz had significantly longer delays [138].

The results reported in Table 17 and displayed in Fig. 8 show that for co-polarized antennas, the minimum measured RMS delay spreads are all lower than 1 ns, while the maximum delay spread values observed are all greater than 100 ns, regardless of frequency or environment. Maximum RMS delay spreads were measured to be 98 ns at 58 GHz [76], between 100 ns and 150 ns at 1.5 GHz [42], and up to 250 ns at 850 MHz [139]. At 28 GHz and 73 GHz the maximum measured RMS delay spreads in LOS environments are smaller than in NLOS environments for most cases, with the only exception for the 73 GHz V-H antenna polarization scenario, where the maximum RMS delay spread in a NLOS environment is larger than that in a LOS environment (21.6 ns greater), as noticed in Table 17 and Fig. 8. Additionally, standard deviations of RMS delay spreads in LOS and NLOS environments at both frequencies are less than 18 ns. There was no clear trend observed between the minimum RMS delay spreads and standard deviations of RMS delay spreads in relation to environment, polarization, or frequency.

RMS delay spreads are also studied when considering the single best unique antenna pointing angles between the TX and RX locations that resulted in the strongest received power, for each TX-RX location combination measured. For all LOS and NLOS locations measured, the CDF of the RMS delay spreads for the angles with the strongest received power (lowest path loss) are also provided in the subfigures in Fig. 8. For both 28 GHz and 73 GHz, and for the co- and cross-polarized antenna configurations, the mean RMS delay spreads when considering the single strongest pointing angles are less as compared to the mean RMS delay spreads over all unique antenna pointing angles measured for all locations, except for 73 GHz V-H NLOS. This is particularly true for LOS environments, where Fig. 8 shows that the strongest beams offer much smaller RMS delay spread than arbitrary pointing beams, although the difference is not as great for NLOS channels. For cross-polarized NLOS channels, however, the best beam can sometimes increase the multipath dispersion. As shown in Table 17 and Fig. 8, the strongest beams in NLOS locations resulted in greater standard deviations than in LOS locations, which is not observed when considering arbitrary pointing angles. Table 17 shows that the minimum values of RMS delay spreads when considering the best beam are in general within 4 ns regardless of frequency, environment, and antenna polarization, indicating that the best beam can simultaneously minimize path loss and RMS delay spread. These observations indicate the opportunity to minimize multipath time dispersion with high gain, narrowbeam, directional, co-polarized antennas for indoor mmWave communications systems when exploiting the strongest pointing angle beams between the TX and RX.

TABLE 18. Comparison of mean, standard deviation, minimum, and maximum RMS delay spreads at 28 GHz and 73 GHz for combined antenna polarizations in LOS and NLOS indoor propagation environments. "Env." indicates the environment type of the RX locations.

RMS Delay Spreads Over All Arbitrary Angles For Combined Polarizations				
Env.	28 GHz			
	μ (ns)	σ (ns)	Min. (ns)	Max. (ns)
LOS	17.2	16.4	0.7	134.4
NLOS	17.8	12.5	0.6	198.5
LOS-Best	4.1	1.6	1.6	6.1
NLOS-Best	13.4	13.1	0.9	47.9
Env.	73 GHz			
	μ (ns)	σ (ns)	Min. (ns)	Max. (ns)
LOS	12.1	17.2	0.5	143.8
NLOS	10.7	13.0	0.5	142.0
LOS-Best	3.6	1.5	0.8	5.1
NLOS-Best	11.3	14.4	3.7	73.4

Figs. 8c and 8d show similar RMS delay spread CDF curves at 73 GHz for both V-V and V-H antenna polarization configurations. The figures indicate that 90% of RMS delay spreads in both LOS and NLOS indoor environments are less than 30 ns at 73 GHz. Little difference in RMS delay spread is noticed between LOS and NLOS locations for both V-V and V-H antenna configurations.

At both 28 GHz and 73 GHz, the mean RMS delay spreads were significantly reduced when considering the single strongest co-polarized pointing angle combinations between the TX and RX antennas, where in V-V LOS cases the mean RMS delay spreads were reduced from 17.3 ns to 4.1 ns, and from 12.8 ns to 3.6 ns, for 28 GHz and 73 GHz respectively. Somewhat smaller reductions in RMS delay spreads were seen in NLOS for the V-V case, where the mean RMS delay spreads were reduced from 17.7 ns to 13.4 ns, and from 12.3 ns to 11.3 ns, for 28 GHz and 73 GHz, respectively, when considering the strongest pointing angles. The smaller RMS delay spreads are due to the strongest received power angle combinations containing a main LOS component and very weak multipath at large excess delays (or none at all). The largest difference in mean RMS delay spread for co-polarized antennas when comparing arbitrary pointing angles to the strongest pointing angles is in the LOS environment, where beamforming and beam steering algorithms [140], [141] will be useful in reducing RMS delay spread by searching for the strongest received power pointing angles. As seen in Table 17, the V-H scenario at 28 GHz is very similar to the V-V case with mean RMS delay spreads reduced by 9.9 ns and 4.8 ns in LOS and NLOS respectively; however, 73 GHz mean RMS delay spreads reduced by 4.4 ns in LOS and increased by 4.1 ns in NLOS for the V-H case.

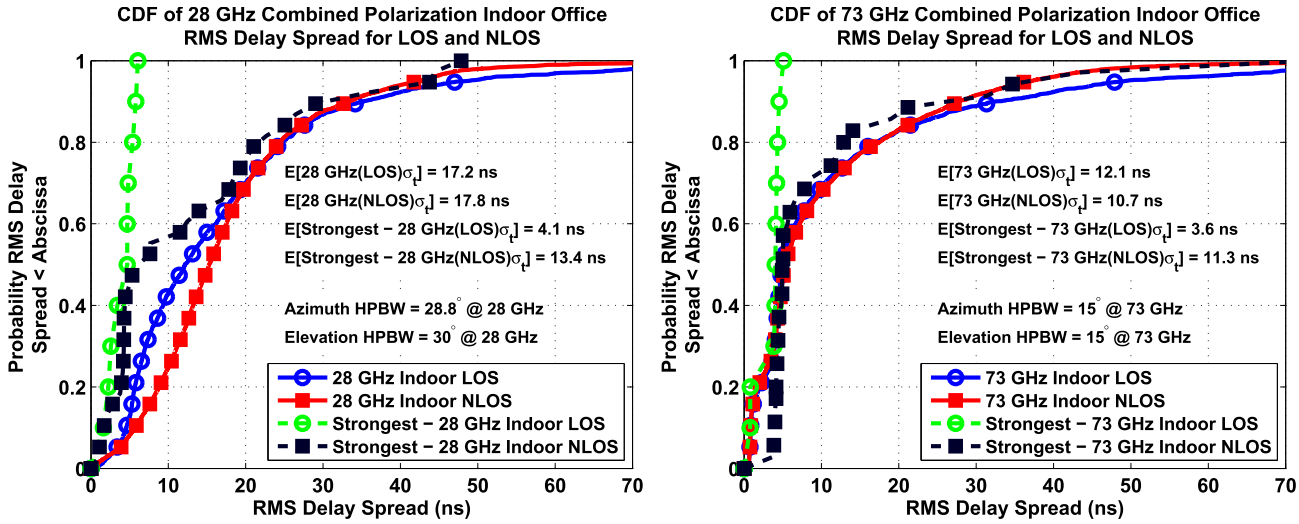

(a) 28 GHz combined polarization indoor directional RMS delay spread

(b) 73 GHz combined polarization indoor directional RMS delay spread

FIGURE 9. 28 GHz and 73 GHz arbitrary pointing angle (directional) combined polarization RMS delay spread CDFs for TX antenna heights of 2.5 m and RX antenna heights of 1.5 m in a typical indoor office environment for LOS and NLOS scenarios. The T-R separation distances ranged from 3.9 m to 45.9 m. (a) 28 GHz combined polarization; (b) 73 GHz combined polarization.

In all cases for the 28 GHz and 73 GHz measurements, the cross-polarized antenna RMS delay spreads were larger than co-polarized antenna RMS delay spreads (see Table 17), likely a result of additional energy captured based on wave de-polarization from the TX to RX in the indoor mmWave environment, and was also noticed in [46], [48], and [115] where cross-polarized omnidirectional antennas experienced 3-4 ns larger mean and maximum RMS delay spreads compared to co-polarized antennas.

Table 17 summarizes the mean, standard deviation, minimum, and maximum measured RMS delay spread statistics calculated from the 28 GHz and 73 GHz measurements for co- and cross-polarized antenna configurations in LOS and NLOS environments. Compared to 28 GHz, the 73 GHz band had smaller observed RMS delay spreads, similar to results reported in [142] when comparing RMS delay spreads of 2 GHz, 5 GHz, and 17 GHz. The time dispersion values given in Table 17 are marginally different than those in [109] as a result of a newer more stringent noise thresholding method described in [112].

B. MULTIPATH TIME DISPERSION STATISTICS FOR COMBINED-POLARIZED ANTENNAS

Time dispersion characteristics are also important for modeling applications that will employ arbitrary antenna polarization configurations such as mobile handsets that are constantly changing orientations. Figs. 9a and 9b show the CDFs for the RMS delay spreads for combined polarization measurements at 28 GHz and 73 GHz, respectively, for PDPs measured over all arbitrary pointing angles and also for the single strongest pointing angles for each TX-RX location combination. Table 18 summarizes the mean RMS delay spreads from the figures and includes the standard deviation, minimum, and maximum measured RMS delay spread statistics calculated at 28 GHz and 73 GHz for combined antenna polarizations for LOS and NLOS environments.

Figs. 9a and 9b indicate that 90% of RMS delay spreads for combined antenna polarizations, regardless of environment, are less than 35 ns and 30 ns at 28 GHz and 73 GHz, respectively. From Table 17 and Table 18, there is no distinguishable difference between co-polarization (V-V) and combined polarization in the RMS delay spread statistics. The RMS delay spread statistics at 28 GHz are, in general, slightly greater than the corresponding statistics at 73 GHz. The measured mean RMS delay spreads for combined polarizations at 28 GHz are 17.2 ns (LOS) and 17.8 ns (NLOS), and are larger than the mean RMS delay spreads of 12.1 ns (LOS) and 10.7 ns (NLOS) at 73 GHz. Irrespective of frequency and environment, the minimum RMS delay spreads are all less than 2 ns and the maximum RMS delay spreads are all less than 200 ns. A majority of standard deviations of RMS delay spread are around 15 ns. The minimum value and standard deviation of RMS delay spreads show no clear dependence on environment, polarization, or frequency.

Similar to statistics for separate polarizations, the RMS delay spreads are lower when only considering the single strongest antenna pointing orientation between the TX and RX at 28 GHz and 73 GHz, most notably where Table 18 and Fig. 9 show in LOS environments that the mean RMS delay spread reduces from 17.2 ns to 4.1 ns at 28 GHz (in LOS) and from 12.1 ns to 3.6 ns at 73 GHz (in LOS). From Table 18 it is apparent that the V-V antenna polarization corresponds to the maximum observed RMS delay spreads at 28 GHz in LOS (134.4 ns) and NLOS (198.5 ns) environments for combined polarizations (as observed in Table 17). The same observation is made at 73 GHz in NLOS (142.0 ns), however, in the LOS case at 73 GHz, the V-H antenna

polarization in LOS (143.8 ns) corresponds to the maximum observed RMS delay spread for combined antenna polarizations.

Work in [124] suggests a simple algorithm to find the best beam directions that can simultaneously minimize both RMS delay spread and path loss (finding the best paths that simultaneously have both strong SNR and very small multipath time dispersion). By selecting a beam with both low RMS delay spread and low path loss, relatively high SNR can be achieved at the RX using directional antennas without complicated equalization, meaning that low latency single carrier (wideband) modulations may be a viable candidate for future mmWave wireless communications systems [135]. The measured values presented in Tables 17–18 and Figs. 8 and 9 give insight to the range of multipath channel parameters for arbitrary pointing co-, cross-, or combined-polarized antennas, as well as for the best TX and RX antenna pointing angles that result in the lowest path loss/link attenuation.

VI. CONCLUSION

This paper provided large-scale path loss models and temporal statistics derived from extensive wideband mmWave indoor propagation measurements using rotatable directional horn antennas at 28 GHz and 73 GHz. Directional and omnidirectional path loss models and directional multipath RMS delay spread values were presented, yielding insight into mmWave indoor office propagation characteristics. Extensive analysis shows that for mmWave indoor channels, large-scale path loss over distance and frequency may be modeled with virtually no sacrifice in accuracy by using simple close-in free space reference distance models (e.g., the CI or CIF models) with just one or two parameters that ensure a physical tie to the transmitter power, rather than using existing 3GPP and WINNER floating intercept (FI) models that have no tie to the transmitted power, lack intuition when interpreting model parameters, and require more parameters.

Single frequency directional path loss models were provided using the 1 m close-in free space reference distance (CI), close-in free space reference distance with XPD factor (CIX), and floating-intercept (FI) forms. The CI path loss models showed that for co-polarized antennas, constructive interference due to waveguiding and reflections resulted in nearly identical LOS PLEs of 1.7 and 1.6 for 28 GHz and 73 GHz, respectively, smaller than theoretical FSPL ($n = 2$), suggesting that directional LOS PLEs are independent of frequency. Path loss observed in NLOS environments had much greater attenuation (44 dB ($n = 4.4$) and 53 dB ($n = 5.3$) per decade of distance for 28 GHz and 73 GHz, respectively) than in LOS environments; however, the high attenuation was significantly reduced (resulting in $n = 3.0$ at 28 GHz and $n = 3.4$ at 73 GHz), when considering the best TX and RX antenna pointing angles that resulted in the maximum received power at each measured location. The shadowing factor increased from 28 GHz to 73 GHz (2.5 dB to 3.2 dB in LOS, and 11.6 dB to 15.7 dB in NLOS), indicating more variability in large-scale shadowing at higher mmWave frequencies, most likely due to increased diffuse scattering, greater diffraction loss, and weaker reflections. The directional PLEs for the V-H antenna polarization configurations indicated significant de-polarization in NLOS indoor environments at both 28 GHz and 73 GHz. For LOS channels, large directional XPD factors of 24.7 dB and 31.4 dB were found for V-H scenarios at 28 GHz and 73 GHz, respectively, and showed that there was large isolation between co- and cross-polarized transmission when using high-gain directional horn antennas. Larger fluctuations in received signal strength about the distance-dependent mean path loss were observed at 73 GHz in NLOS environments for cross-polarized directional antennas (15.9 dB) compared to 28 GHz cross-polarized directional antennas (10.9 dB). The CIX model was shown to be a useful and simple path loss model for cross-polarized antenna systems, and was shown to improve (reduce) the standard deviation compared to the CI model, most notably by 4.0 dB and 2.7 dB in LOS and NLOS environments, respectively, at 73 GHz. The FI path loss model is sensitive to the post-processing methods and was shown to lack a physical basis for radio propagation. The directional CI path loss model better explained the physical propagation at 28 GHz and 73 GHz compared to the FI model, where the β slope values were 1.0 and 0.7 for V-V in LOS at 28 GHz and 73 GHz, respectively, suggesting the nonsensical situation of ultra-low loss with distance when using the FI model. The better stability and physical sensibility of the CI model is due to the fixation of received power at 1 m from the transmitter, which is based in physics [112], as well as the inherent frequency dependence of path loss in the first meter of propagation.

For the combined co- and cross-polarized measurements, which are the most representative of arbitrary (e.g. random) antenna orientations in an indoor wireless network, the single frequency directional LOS PLEs were 2.9 and 3.1 for 28 GHz and 73 GHz, respectively, noticeably greater than FSPL ($n = 2$). NLOS environments experienced greater attenuation for the combined data, with PLEs of 4.8 and 5.7 at 28 GHz and 73 GHz, respectively, showing a higher path loss with increased distance at higher frequencies in the indoor channel (this frequency dependence on PLE is not as prominent in outdoor channels [112]). However, the NLOS path loss attenuation was reduced (resulting in $n = 3.0$ at 28 GHz and $n = 3.4$ at 73 GHz), when considering the antenna pointing angle combination between the TX and RX that resulted in maximum received power for each location combination.

Single frequency omnidirectional path loss models were provided in the CI, CIX, and FI forms for the co- and cross-polarization measurements. Similar to the directional models, the CI PLEs calculated in LOS environments were significantly smaller than the theoretical free space PLE (1.1 and 1.3 for 28 GHz and 73 GHz, respectively), due to constructive interference and a waveguide effect in the indoor mmWave propagation channel. In NLOS indoor environments for co-polarized antennas, the 73 GHz CI model PLE was 3.2 (32 dB of attenuation per decade of distance) and

the 28 GHz PLE was 2.7 (27 dB of attenuation per decade of distance), with shadow fading factors of 11.3 dB and 9.6 dB at 73 GHz and 28 GHz, respectively. The 73 GHz measurements showed greater omnidirectional isolation for co- and cross-polarized antenna configurations with a LOS XPD factor of 22.8 dB and a NLOS XPD factor of 15.4 dB, encouraging the use of dual polarization modulations and antenna polarization diversity applications for indoor mmWave communications systems. The 28 GHz measurements exhibited smaller omnidirectional isolation than 73 GHz, 14.0 dB and 10.4 dB for LOS and NLOS, respectively, but may still be good enough for polarization diversity. From the directional and omnidirectional path loss models presented here, it is clear that path loss increases with frequency much more prominently than in outdoor channels - likely due to the pronounced impact of the environment which is in very close proximity to the TX and RX and likely induces frequency-dependent diffuse scattering and weaker reflections at smaller wavelengths [112].

The multi-frequency directional and omnidirectional path loss models for both separate and combined polarization measurements showed the simplicity and accuracy of the CI and CIF models which use a FSPL anchored at 1 m to create a physically-based model for path loss. The three-parameter floating ABG model in all cases resulted in lower standard deviation compared to the CI and CIF models, but a large majority of the scenarios had differences less than 1 dB, and in all cases *the differences between all models were less than an order of magnitude of the standard deviation of all models*. The differences in modeling error between the CIF and ABG models were always minor, well within typical error ranges caused by gain drift, flexing of cables, antenna pointing or distance errors, and other typical measurement errors. All omnidirectional path loss data are provided in tables in Appendix B so that other researchers may generate their own models and conduct further studies based on the indoor propagation data at 28 GHz and 73 GHz.

For the most important case of the combined polarization omnidirectional path loss models, the single frequency CI model showed that there is more attenuation at 73 GHz (LOS PLE $=$ 2.4, NLOS PLE $=$ 3.8) than at 28 GHz (LOS PLE $=$ 1.8, NLOS PLE $=$ 3.1), where the FI model lacked an intuitive explanation of physics with the 73 GHz LOS and NLOS β values of 0.8 and 2.2, respectively. The multi-frequency CI and CIF models exhibited value as a one-parameter and two-parameter model, respectively, with little variation in standard deviation from the more complex and less intuitive three-parameter ABG model, where in LOS the standard deviations were 10.4 dB (CI), 9.9 dB (CIF), and 9.5 dB (ABG) for each respective model. Furthermore, the NLOS standard deviations were 12.5 dB for CI, 11.9 dB for CIF, and 11.6 dB for the ABG model, not considerably different for already large standard deviations that are greater than 11 dB. The CI PLEs and CIF n values also matched in LOS (PLE and n $=$ 2.1) and NLOS (PLE and n $=$ 3.4) environments for the combined polarization omnidirectional models. The ABG model provided slightly lower standard deviations in LOS and NLOS (fraction of a dB from CI and CIF), but at the expense of more parameters that varied widely and often lacked intuitive meaning, and with no physical tie to transmitted power.

This work showed the efficacy of the CI model standardized to a 1 m free space reference distance. This model allows for simple calculations of large-scale path loss, as well as easy comparisons across frequency bands, environments, and measurements from other researchers [112], [122]. The CIF model is a natural extension of the CI model to account for frequency-dependent path loss beyond the first meter, and uses two parameters while retaining a link to the close-in free space distance, and offers virtually identical performance to the more complex three-parameter ABG model that has a floating optimization parameter not tied to the true transmitted power. This work shows that either the one-parameter CI model or the two-parameter CIF model may be most suitable for indoor large-scale path loss modeling, with the CIF model providing a better fit to measured data and intuitive meaning of the two model parameters over a wide range of mmWave frequencies, whereas outdoor channels are suitably modeled with the one-parameter CI model. 3GPP, ITU, and other standards bodies would do well to consider the simplicity, accuracy, and stability of the CI and CIF models for future 5G standards.

Time dispersion characteristics using directional antennas showed that 90% of the RMS delay spreads in both LOS and NLOS environments were under 40 ns and 30 ns at 28 GHz and 73 GHz, respectively. LOS locations were generally found to have smaller RMS delay spreads than NLOS locations due to less obstructions and multipath in the LOS environment, but by no more than a few ns (not an order of magnitude). The higher frequency of 73 GHz had greater path loss for a fixed transmitter power, thus making late arriving components weaker than at 28 GHz. The mean RMS delay spreads for the single strongest pointing angles were reduced by 13.2 ns in LOS (from 17.3 ns to 4.1 ns) and 4.3 ns in NLOS (from 17.7 ns to 13.4 ns) for 28 GHz V-V scenarios, and were reduced by 9.2 ns and 1.0 ns in LOS and NLOS 73 GHz V-V scenarios, respectively, compared to the corresponding mean RMS delay spreads averaged over all arbitrary antenna pointing angles, indicating the potential for implementing steerable beams to reduce multipath time dispersion while increasing SNR for indoor mmWave wideband communications systems. Cross-polarized channels had less reduction in RMS delay spread when choosing the strongest angles between the TX and RX at both 28 GHz and 73 GHz, and in NLOS at 73 GHz, cross-polarized strongest received angles increased the RMS delay spread compared to arbitrary beam pointing. For time dispersion statistics with combined polarizations at 28 GHz and 73 GHz, it is apparent that the V-V polarized antennas contribute to larger delay spreads (maximum of 198.5 ns in NLOS), due to cross-polarization isolation in the V-H case. Similar to the co- and cross-

polarized time dispersion statistics, the combined polarization mean RMS delay spreads were reduced when only considering the single strongest beams in LOS environments (reduced from 17.2 ns to 4.1 ns at 28 GHz and 12.1 ns to 3.6 ns at 73 GHz).

The multipath time dispersion characteristics and large-scale path loss models presented here will be important for mmWave channel modeling and may assist in the creation of new mmWave systems that support the Internet of Things (IoT) and the indoor use of future unlicensed bands or 5G cellular for high bandwidth applications. The large-scale path loss models presented in this paper were explored and compared with extensive propagation data, and new multi-frequency path loss models were introduced for use across the entire mmWave spectrum. Results suggest the use of simpler and physically-based path loss models compared to previous 3GPP models that use more parameters but offer very little additional accuracy while lacking a physical basis. While path loss characteristics at 73 GHz showed higher attenuation than at 28 GHz, both will be attractive options for high bandwidth and high data-rate applications in indoor environments.

APPENDIX A
PATH LOSS MODEL PARAMETER CLOSED-FORM EXPRESSIONS

Here we provide mathematical derivations for the closed-form solutions for minimum shadow fading (SF) standard deviation (i.e. best fit) large-scale path loss model parameters, for the CI (1), CIX (2), CIF (6), CIFX (7), FI (3), ABG (4), and ABGX (5) path loss models. The raw data used to compute the omnidirectional models in this paper are given in Tables 19–22 in Appendix B.

A. CI PATH LOSS MODEL

The CI model with a reference distance of 1 m is given by (1) where n denotes the PLE, d is the 3D T-R separation distance, and X_σ^{CI} is the SF. FSPL(f, 1 m) denotes the free space path loss in dB at a 3D T-R separation distance of 1 m at the carrier frequency f:

$$\mathrm{FSPL}(f, 1\ \mathrm{m})[\mathrm{dB}] = 10\log_{10}\left(\frac{4\pi f}{c}\right)^2 \tag{12}$$

where c is the speed of light.

From (1), the SF random variable is given by (13)

$$\begin{aligned} X_\sigma^{\mathrm{CI}} &= \mathrm{PL}^{\mathrm{CI}}(f, d)[\mathrm{dB}] - \mathrm{FSPL}(f, 1\ \mathrm{m})[\mathrm{dB}] - 10n\log_{10}(d) \\ &= A - nD \end{aligned} \tag{13}$$

where A (in dB) represents $\mathrm{PL}^{\mathrm{CI}}(f, d)[\mathrm{dB}] - \mathrm{FSPL}(f, 1\ \mathrm{m})[\mathrm{dB}]$, and D denotes $10\log_{10}(d)$. It follows that the standard deviation of the random variable X_σ^{CI} is:

$$\sigma^{\mathrm{CI}} = \sqrt{\sum X_\sigma^{\mathrm{CI}2}/N} = \sqrt{\sum (A - nD)^2/N} \tag{14}$$

where N is the number of measured path loss data points (see Tables 19–22 for omnidirectional path loss data points and values). All summations in this appendix are performed over the length of the data or sample size, and the sums are calculated *directly* from the elements, i.e., if the elements are

TABLE 19. 28 GHz co-polarized antenna (V-V) omnidirectional path loss values with corresponding Environment (Env.), TX IDs, RX IDs, path loss (PL) in dB, and 3D T-R separation distance in meters.

28 GHz Omnidirectional V-V Path Loss				
Env.	TX ID	RX ID	PL (dB)	T-R (m)
LOS	1	1	69.3	6.4
LOS	1	4	75.3	7.9
LOS	1	7	76.5	12.9
LOS	2	10	66.3	4.1
LOS	3	16	68.0	5.3
LOS	4	11	74.3	12.7
LOS	4	12	70.4	7.1
LOS	4	28	75.4	21.3
LOS	4	121	71.3	7.1
LOS	4	161	74.5	20.6
NLOS	1	2	76.6	7.8
NLOS	1	3	82.7	10.1
NLOS	1	5	84.3	11.9
NLOS	1	6	86.4	14.4
NLOS	1	8	95.9	25.9
NLOS	1	9	118.5	32.9
NLOS	2	11	78.5	9.0
NLOS	2	12	89.5	28.5
NLOS	2	13	113.1	29.2
NLOS	2	14	119.3	30.4
NLOS	2	15	115.8	39.2
NLOS	2	16	97.8	41.9
NLOS	2	17	120.5	45.9
NLOS	2	18	93.6	12.1
NLOS	2	19	103.1	15.5
NLOS	2	20	111.3	17.1
NLOS	2	21	78.0	6.7
NLOS	2	22	95.3	14.8
NLOS	2	161	98.6	41.9
NLOS	3	17	85.8	8.7
NLOS	3	23	79.9	5.6
NLOS	3	24	86.1	7.8
NLOS	3	25	76.31	8.4
NLOS	3	26	72.9	5.5
NLOS	3	27	75.8	8.3
NLOS	4	13	97.2	8.2
NLOS	4	14	105.0	10.8
NLOS	4	15	97.5	20.8
NLOS	4	16	80.0	20.6
NLOS	4	18	96.8	33.0
NLOS	5	8	73.8	3.9
NLOS	5	19	75.3	6.9
NLOS	5	28	86.1	15.6
NLOS	5	29	81.3	15.0
NLOS	5	30	88.7	11.4
NLOS	5	31	90.4	13.9
NLOS	5	32	90.2	31.2
NLOS	5	33	97.0	9.1

TABLE 20. 28 GHz cross-polarized antenna (V-H) omnidirectional path loss values with corresponding Environment (Env.), TX IDs, RX IDs, path loss (PL) in dB, and 3D T-R separation distance in meters.

28 GHz Omnidirectional V-H Path Loss				
Env.	TX ID	RX ID	PL (dB)	T-R (m)
LOS	1	1	84.1	6.4
LOS	1	4	87.7	7.9
LOS	1	7	89.7	12.9
LOS	2	10	78.6	4.1
LOS	3	16	83.4	5.3
LOS	4	11	88.2	12.7
LOS	4	12	85.1	7.1
LOS	4	28	90.2	21.3
LOS	4	121	85.0	7.1
LOS	4	161	89.8	20.6
NLOS	1	2	88.2	7.8
NLOS	1	3	91.3	10.1
NLOS	1	5	94.7	11.9
NLOS	1	6	100.1	14.4
NLOS	1	8	115.3	25.9
NLOS	2	11	88.5	9.0
NLOS	2	12	108.8	28.5
NLOS	2	13	141.6	29.2
NLOS	2	14	139.6	30.4
NLOS	2	16	113.4	41.9
NLOS	2	18	98.9	12.1
NLOS	2	19	113.7	15.5
NLOS	2	20	120.4	17.1
NLOS	2	21	83.7	6.7
NLOS	2	22	101.6	14.8
NLOS	2	161	110.5	41.9
NLOS	3	17	97.2	8.7
NLOS	3	23	92.7	5.6
NLOS	3	24	95.8	7.8
NLOS	3	25	88.9	8.4
NLOS	3	26	86.7	5.5
NLOS	3	27	89.3	8.3
NLOS	4	13	104.6	8.2
NLOS	4	14	112.8	10.8
NLOS	4	15	108.4	20.8
NLOS	4	16	93.7	20.6
NLOS	4	18	109.4	33.0
NLOS	5	8	89.3	3.9
NLOS	5	19	91.5	6.9
NLOS	5	28	98.4	15.6
NLOS	5	29	93.7	15.0
NLOS	5	30	96.1	11.4
NLOS	5	31	100.2	13.9
NLOS	5	32	104.8	31.2
NLOS	5	33	104.6	9.1

TABLE 21. 73 GHz co-polarized antenna (V-V) omnidirectional path loss values with corresponding Environment (Env.), TX IDs, RX IDs, path loss (PL) in dB, and 3D T-R separation distance in meters.

73 GHz Omnidirectional V-V Path Loss				
Env.	TX ID	RX ID	PL (dB)	T-R (m)
LOS	1	1	81.7	6.4
LOS	1	4	81.2	7.9
LOS	1	7	86.7	12.9
LOS	2	10	79.9	4.1
LOS	3	16	82.4	5.3
LOS	4	11	84.1	12.7
LOS	4	12	82.3	7.1
LOS	4	28	82.6	21.3
LOS	4	121	83.2	7.1
LOS	4	161	84.6	20.6
NLOS	1	2	92.1	7.8
NLOS	1	3	89.8	10.1
NLOS	1	5	100.4	11.9
NLOS	1	6	104.0	14.4
NLOS	1	8	121.8	25.9
NLOS	2	11	92.8	9.0
NLOS	2	12	102.1	28.5
NLOS	2	13	118.9	29.2
NLOS	2	14	127.4	30.4
NLOS	2	15	142.5	39.2
NLOS	2	16	111.2	41.9
NLOS	2	18	115.7	12.1
NLOS	2	19	142.5	15.5
NLOS	2	21	94.5	6.7
NLOS	2	22	116.3	14.8
NLOS	2	161	108.2	41.9
NLOS	3	17	107.5	8.7
NLOS	3	23	102.7	5.6
NLOS	3	24	111.4	7.8
NLOS	3	25	90.4	8.4
NLOS	3	26	93.3	5.5
NLOS	3	27	89.7	8.3
NLOS	4	13	104.7	8.2
NLOS	4	14	115.5	10.8
NLOS	4	15	114.2	20.8
NLOS	4	16	102.4	20.6
NLOS	4	18	108.4	33.0
NLOS	5	8	91.0	3.9
NLOS	5	19	90.2	6.9
NLOS	5	28	100.1	15.6
NLOS	5	29	94.7	15.0
NLOS	5	30	107.6	11.4
NLOS	5	31	112.8	13.9
NLOS	5	32	105.5	31.2
NLOS	5	33	118.7	9.1

in dB units then the sum is calculated by adding all of the elements in dB units.

Minimizing the SF standard deviation σ^{CI} is equivalent to minimizing the term $\sum (A - nD)^2$. When $\sum (A - nD)^2$ is minimized, the derivative with respect to n should be zero:

$$\frac{d \sum (A - nD)^2}{dn} = \sum 2D(nD - A)$$

TABLE 22. 73 GHz cross-polarized antenna (V-H) omnidirectional path loss values with corresponding Environment (Env.), TX IDs, RX IDs, path loss (PL) in dB, and 3D T-R separation distance in meters.

73 GHz Omnidirectional V-H Path Loss				
Env.	TX ID	RX ID	PL (dB)	T-R (m)
LOS	1	1	102.4	6.4
LOS	1	4	100.4	7.9
LOS	1	7	111.5	12.9
LOS	2	10	101.3	4.1
LOS	3	16	102.9	5.3
LOS	4	11	108.2	12.7
LOS	4	12	104.0	7.1
LOS	4	28	106.6	21.3
LOS	4	121	106.0	7.1
LOS	4	161	108.7	20.6
NLOS	1	2	106.1	7.8
NLOS	1	3	108.8	10.1
NLOS	1	5	116.7	11.9
NLOS	1	6	115.3	14.4
NLOS	2	11	110.6	9
NLOS	2	12	124.2	28.5
NLOS	2	16	138.9	41.9
NLOS	2	18	130.6	12.1
NLOS	2	21	111.0	6.7
NLOS	2	22	126.6	14.8
NLOS	2	161	126.4	41.9
NLOS	3	17	122.3	8.7
NLOS	3	23	117.2	5.6
NLOS	3	24	122.1	7.8
NLOS	3	25	109.7	8.4
NLOS	3	26	104.8	5.5
NLOS	3	27	113.3	8.3
NLOS	4	13	123.4	8.2
NLOS	4	14	140.2	10.8
NLOS	4	15	134.2	20.8
NLOS	4	16	116.2	20.6
NLOS	4	18	129.9	33.0
NLOS	5	8	106.7	3.9
NLOS	5	19	112.8	6.9
NLOS	5	28	117.7	15.6
NLOS	5	29	117.4	15.0
NLOS	5	30	125.8	11.4
NLOS	5	31	120.2	13.9
NLOS	5	32	128.3	31.2
NLOS	5	33	132.1	9.1

$$= 2\sum D(nD - A)$$
$$= 2(n\sum D^2 - \sum DA) = 0 \qquad (15)$$

Therefore, from (15):

$$n = \frac{\sum DA}{\sum D^2} \qquad (16)$$

and hence the minimum SF standard deviation for the CI model is:

$$\sigma_{min}^{\mathrm{CI}} = \sqrt{\sum (A - D\frac{\sum DA}{\sum D^2})^2/N} \qquad (17)$$

To find the closed-form solutions for software processing such as MATLAB, A and D are written as column vectors, and n can be expressed in matrix form as:

$$n = A^T(D^TD)^{-1}D \qquad (18)$$

Accordingly, the minimum SF standard deviation for the CI model becomes:

$$\sigma_{min}^{\mathrm{CI}} = \sqrt{\sum (A - (A^T(D^TD)^{-1}D)D)^2/N} \qquad (19)$$

From Section IV the CI model may be used for estimating path loss for co-, cross-, or combined-polarization measurement data with arbitrary polarizations, where the PLE n is usually higher for cross-polarization as compared to co-polarization for the same locations.

B. CIX PATH LOSS MODEL

The CIX model (2) is an extension of the CI model (1) that describes path loss from cross-polarization measurements, where XPD denotes the cross-polarization discrimination factor. The CIX model in (2) uses the same PLE n as in the co-polarization CI model (1). The proper value for XPD is solved via the minimum mean square error (MMSE) method that fits the measured cross-polarized path loss data with the smallest error (i.e., minimum SF standard deviation).

Using the same notations as (13), the SF in (2) is expressed as:

$$X_\sigma^{\mathrm{CIX}} = A - nD - \mathrm{XPD} \qquad (20)$$

and the SF standard deviation is:

$$\sigma^{\mathrm{CIX}} = \sqrt{\sum {X_\sigma^{\mathrm{CIX}}}^2/N} = \sqrt{\sum (A - nD - \mathrm{XPD})^2/N} \qquad (21)$$

The term $\sum (A - nD - \mathrm{XPD})^2$ should be minimized in order to minimize σ^{CIX}. Let the derivative of $\sum (A - nD - \mathrm{XPD})^2$ with respect to XPD be zero, such that:

$$\frac{\partial \sum (A - nD - \mathrm{XPD})^2}{\partial \mathrm{XPD}} = \sum 2(\mathrm{XPD} + nD - A)$$
$$= 2(\mathrm{XPD} \times N + n\sum D - \sum A)$$
$$= 2(\mathrm{XPD} \times N + \frac{\sum DA \sum D}{\sum D^2} - \sum A)$$
$$= 0 \qquad (22)$$

From (22):

$$\text{XPD} = \frac{\sum A}{N} - \frac{\sum DA \sum D}{N \sum D^2} \tag{23}$$

Therefore, the minimum SF standard deviation for the CIX model is:

$$\sigma_{min}^{\text{CIX}} = \sqrt{\sum (A - D\frac{\sum DA}{\sum D^2} - \frac{\sum A}{N} + \frac{\sum DA \sum D}{N \sum D^2})^2 / N} \tag{24}$$

Since both A and D can be considered column vectors, the optimum XPD can also be expressed in matrix form as:

$$\text{XPD} = \frac{\sum A - (A^T (D^T D)^{-1} D) \sum D}{N} \tag{25}$$

C. CIF PATH LOSS MODEL

The equation of the CIF model (6) with a reference distance of 1 m is re-organized in the form:

$$\text{PL}^{\text{CIF}}(f, d)[dB] = \text{FSPL}(f, 1\text{ m})[\text{dB}] + 10\log_{10}(d)\left(n(1-b) + \frac{nb}{f_0} f\right) + X_\sigma^{\text{CIF}} \tag{26}$$

where n is the PLE that includes the frequency-effect parameter b, and f_0 is the specified reference frequency that may be selected as the weighted average of all measured frequencies. Let $A = \text{PL}^{\text{CIF}}(f, d)[\text{dB}] - \text{FSPL}(f, 1\text{ m})[\text{dB}]$, $D = 10\log_{10}(d)$, $a = n(1-b)$, and $g = \frac{nb}{f_0}$, then we have:

$$X_\sigma^{\text{CIF}} = A - D(a + gf) \tag{27}$$

The SF standard deviation is:

$$\sigma^{\text{CIF}} = \sqrt{\sum X_\sigma^{\text{CIF}2} / N} = \sqrt{\sum (A - D(a+gf))^2 / N} \tag{28}$$

Minimizing σ^{CIF} is equivalent to minimizing $\sum (A - D(a + gf))^2$. When $\sum (A - D(a+gf))^2$ is minimized, its derivatives with respect to a and g should be zero, i.e.

$$\begin{aligned} \frac{\partial \sum (A - D(a+gf))^2}{\partial a} &= \sum 2D(aD + gDf - A) \\ &= 2(a\sum D^2 + g\sum D^2 f - \sum DA) \\ &= 0 \end{aligned} \tag{29}$$

$$\begin{aligned} \frac{\partial \sum (A - D(a+gf))^2}{\partial g} &= \sum 2Df(aD + gDf - A) \\ &= 2(a\sum D^2 f + g\sum D^2 f^2 \\ &\quad - \sum DAf) = 0 \end{aligned} \tag{30}$$

which can be simplified to:

$$a\sum D^2 + g\sum D^2 f - \sum DA = 0 \tag{31}$$

$$a\sum D^2 f + g\sum D^2 f^2 - \sum DAf = 0 \tag{32}$$

Combining (31) and (32) yields:

$$a = \frac{\sum D^2 f \sum DAf - \sum D^2 f^2 \sum DA}{(\sum D^2 f)^2 - \sum D^2 \sum D^2 f^2} \tag{33}$$

$$g = \frac{\sum D^2 f \sum DA - \sum D^2 \sum DAf}{(\sum D^2 f)^2 - \sum D^2 \sum D^2 f^2} \tag{34}$$

Put into matrix form, a and g are:

$$a = \frac{f^T \text{diag}(DD^T) f^T \text{diag}(DA^T) - (\text{diag}(ff^T))^T \text{diag}(DD^T) D^T A}{(f^T \text{diag}(DD^T))^2 - (\text{diag}(ff^T))^T \text{diag}(DD^T) D^T D} \tag{35}$$

$$g = \frac{f^T \text{diag}(DD^T) D^T A - f^T \text{diag}(DA^T) D^T D}{(f^T \text{diag}(DD^T))^2 - (\text{diag}(ff^T))^T \text{diag}(DD^T) D^T D} \tag{36}$$

Equations (33)–(36) are closed-form solutions for a and g. Substituting a and g in (28) with (35) and (36), the minimum SF standard deviation for the CIF model is found.

After solving for a and g, we can use the previous definition $a = n(1-b)$ and $g = \frac{nb}{f_0}$ to calculate n, b, and f_0. However, there are two equations but three unknowns, hence there is no unique solution in general using three parameters. However, a unique closed-form solution is available when f_0 is specified as a constant deemed appropriate by the user, such as the weighted average of all frequencies used in the model, or at a natural loss transition band (e.g., where measurements show an inflection point in the PLE), or at known transition points like the 60 GHz oxygen absorption band. Consequently, n and b are solved by:

$$n = a + gf_0 \tag{37}$$

$$b = \frac{gf_0}{a + gf_0} \tag{38}$$

D. CIFX PATH LOSS MODEL

The CIFX path loss model (7) is also expressed as:

$$\text{PL}^{\text{CIFX}}(f, d)[\text{dB}] = \text{FSPL}(f, 1\text{ m})[\text{dB}] + 10\log_{10}(d)(a + gf) + \text{XPD} + X_\sigma^{\text{CIFX}} \tag{39}$$

where XPD denotes the cross-polarization discrimination factor, a and g have the same meanings as in (27). Note that the CIFX model (39) uses the same a and g as substituted in the CIF model (26), thus the a and g in (39) are also given by (35) and (36), respectively. The XPD is solved via the MMSE method that fits the measured cross-polarized path loss data with the smallest error (i.e., SF standard deviation).

Using the same notations as in the CIF model, the SF in the CIFX model can be expressed as

$$X_\sigma^{\text{CIFX}} = A - (a + gf)D - \text{XPD} \tag{40}$$

Hence the SF standard deviation is:

$$\sigma^{\text{CIFX}} = \sqrt{\sum X_\sigma^{\text{CIFX}2} / N}$$

$$= \sqrt{\sum (A - (a + gf)D - \mathrm{XPD})^2 / N} \quad (41)$$

Thus the term $\sum (A - (a + gf)D - \mathrm{XPD})^2$ should be minimized in order to minimize σ^{CIFX}. With the derivative of $\sum (A - (a + gf)D - \mathrm{XPD})^2$ with respect to XPD set to zero, we have:

$$\begin{aligned} &\frac{\partial \sum (A - (a + gf)D - \mathrm{XPD})^2}{\partial \mathrm{XPD}} \\ &= \sum 2(\mathrm{XPD} + (a + gf)D - A) \\ &= 2(\mathrm{XPD} \times N + a \sum D + g \sum Df - \sum A) = 0 \end{aligned} \quad (42)$$

From (42):

$$\mathrm{XPD} = \frac{\sum A - a \sum D - g \sum Df}{N} \quad (43)$$

Or equivalently

$$\mathrm{XPD} = \frac{\sum A - a \sum D - gD^T f}{N} \quad (44)$$

Therefore, by plugging (35), (36) and (43) back into (41), the minimum SF standard deviation for the CIFX model is found.

E. FI PATH LOSS MODEL

The FI path loss model (3) uses α as the floating intercept in dB (different from a FSPL reference), and β is the slope of the line (different from a PLE). Assuming $B = \mathrm{PL}^{\mathrm{FI}}(d)[\mathrm{dB}]$, and $D = 10\log_{10}(d)$, the SF is given by:

$$X_\sigma^{\mathrm{FI}} = B - \alpha - \beta D \quad (45)$$

and the SF standard deviation is:

$$\sigma^{\mathrm{FI}} = \sqrt{\sum X_\sigma^{\mathrm{FI}2} / N} = \sqrt{\sum (B - \alpha - \beta D)^2 / N} \quad (46)$$

The term $\sum (B - \alpha - \beta D)^2$ is to be minimized, which means its partial derivatives with respect to α and β should be zero, i.e.,

$$\begin{aligned} \frac{\partial \sum (B - \alpha - \beta D)^2}{\partial \alpha} &= \sum 2(\alpha + \beta D - B) \\ &= 2(N\alpha + \beta \sum D - \sum B) \\ &= 0 \end{aligned} \quad (47)$$

$$\begin{aligned} \frac{\partial \sum (B - \alpha - \beta D)^2}{\partial \beta} &= \sum 2D(\alpha + \beta D - B) \\ &= 2(\alpha \sum D + \beta \sum D^2 - \sum DB) \\ &= 0 \end{aligned} \quad (48)$$

(47) and (48) yield:

$$N\alpha + \beta \sum D - \sum B = 0 \quad (49)$$

$$\alpha \sum D + \beta \sum D^2 - \sum DB = 0 \quad (50)$$

Combining (49) and (50) yields:

$$\alpha = \frac{\sum D \sum DB - \sum D^2 \sum B}{(\sum D)^2 - N \sum D^2} \quad (51)$$

$$\beta = \frac{\sum D \sum B - N \sum DB}{(\sum D)^2 - N \sum D^2} \quad (52)$$

The minimum SF standard deviation can be obtained by substituting α and β in (46) with (51) and (52), respectively. Alternatively, α and β in the FI model can be expressed in matrix form as

$$\beta = (D - \overline{D})^T ((D - \overline{D})^T (D - \overline{D}))^{-1} (B - \overline{B}) \quad (53)$$

$$\alpha = \overline{B} - \beta \overline{D} \quad (54)$$

where $\overline{D}$ and $\overline{B}$ denote the mean value of the elements in column vectors D and B, respectively. All the mean values are calculated *directly* from the elements in the vector, i.e., if the elements are in dB scale then the mean is calculated directly in dB scale.

F. ABG PATH LOSS MODEL

The ABG model (4) has a 1 m reference distance and 1 GHz reference frequency where α and γ are coefficients showing the dependence of path loss on distance and frequency, respectively, β is the offset in path loss, d is the 3D T-R separation distance in meters, and f is the carrier frequency in GHz. Assuming $B = \mathrm{PL}^{\mathrm{ABG}}(f, d)[\mathrm{dB}]$, $D = 10\log_{10}(d)$, and $F = 10\log_{10}(f)$ in (4), the SF is given by:

$$X_\sigma^{\mathrm{ABG}} = B - \alpha D - \beta - \gamma F \quad (55)$$

and the SF standard deviation is:

$$\sigma^{\mathrm{ABG}} = \sqrt{\sum X_\sigma^{\mathrm{ABG}2} / N} = \sqrt{\sum (B - \alpha D - \beta - \gamma F)^2 / N} \quad (56)$$

Similar to minimizing Eqs. (13) and (28), the term $\sum (B - \alpha D - \beta - \gamma F)^2$ is to be minimized, which means its partial derivatives with respect to α, β, and γ should be zero, i.e.,

$$\begin{aligned} \frac{\partial \sum (B - \alpha D - \beta - \gamma F)^2}{\partial \alpha} &= \sum 2D(\alpha D + \beta + \gamma F - B) \\ &= 2(\alpha \sum D^2 + \beta \sum D \\ &\quad + \gamma \sum DF - \sum DB) \\ &= 0 \end{aligned} \quad (57)$$

$$\begin{aligned} \frac{\partial \sum (B - \alpha D - \beta - \gamma F)^2}{\partial \beta} &= \sum 2(\alpha D + \beta + \gamma F - B) \\ &= 2(\alpha \sum D + N\beta + \gamma \sum F \\ &\quad - \sum B) \\ &= 0 \end{aligned} \quad (58)$$

$$\begin{aligned} \frac{\partial \sum (B - \alpha D - \beta - \gamma F)^2}{\partial \gamma} &= \sum 2F(\alpha D + \beta + \gamma F - B) \\ &= 2(\alpha \sum DF + \beta \sum F \\ &\quad + \gamma \sum F^2 - \sum FB) \\ &= 0 \end{aligned} \quad (59)$$

$$\alpha = \frac{(\sum D \sum B - N \sum DB)((\sum F)^2 - N \sum F^2) - (\sum D \sum F - N \sum DF)(\sum F \sum B - N \sum FB)}{((\sum D)^2 - N \sum D^2)((\sum F)^2 - N \sum F^2) - (\sum D \sum F - N \sum DF)^2} \quad (66)$$

$$\beta = \frac{(\sum D \sum FB - \sum B \sum DF)(\sum F \sum D^2 - \sum D \sum DF) - (\sum B \sum D^2 - \sum D \sum DB)(\sum D \sum F^2 - \sum F \sum DF)}{((\sum D)^2 - N \sum D^2)(\sum D \sum F^2 - \sum F \sum DF) + (\sum D \sum F - N \sum DF)(\sum F \sum D^2 - \sum D \sum DF)} \quad (67)$$

$$\gamma = \frac{(\sum F \sum B - N \sum FB)((\sum D)^2 - N \sum D^2) - (\sum D \sum F - N \sum DF)(\sum D \sum B - N \sum DB)}{((\sum F)^2 - N \sum F^2)((\sum D)^2 - N \sum D^2) - (\sum D \sum F - N \sum DF)^2} \quad (68)$$

$$\alpha = \frac{(\sum D \sum B - ND^T B)((\sum F)^2 - NF^T F) - (\sum D \sum F - ND^T F)(\sum F \sum B - NF^T B)}{((\sum D)^2 - ND^T D)((\sum F)^2 - NF^T F) - (\sum D \sum F - ND^T F)^2} \quad (69)$$

$$\beta = \frac{(F^T B \sum D - D^T F \sum B)(D^T D \sum F - D^T F \sum D) - (D^T D \sum B - D^T B \sum D)(F^T F \sum D - D^T F \sum F)}{((\sum D)^2 - ND^T D)(F^T F \sum D - D^T F \sum F) + (\sum D \sum F - ND^T F)(D^T D \sum F - D^T F \sum D)} \quad (70)$$

$$\gamma = \frac{(\sum F \sum B - NF^T B)((\sum D)^2 - ND^T D) - (\sum D \sum F - ND^T F)(\sum D \sum B - ND^T B)}{((\sum F)^2 - NF^T F)((\sum D)^2 - ND^T D) - (\sum D \sum F - ND^T F)^2} \quad (71)$$

from (57), (58), and (59) it is clear that

$$\alpha \sum D^2 + \beta \sum D + \gamma \sum DF - \sum DB = 0 \quad (60)$$

$$\alpha \sum D + N\beta + \gamma \sum F - \sum B = 0 \quad (61)$$

$$\alpha \sum DF + \beta \sum F + \gamma \sum F^2 - \sum FB = 0 \quad (62)$$

Such that (60), (61), and (62) in matrix form is:

$$\begin{pmatrix} \sum D^2 & \sum D & \sum DF \\ \sum D & N & \sum F \\ \sum DF & \sum F & \sum F^2 \end{pmatrix} \begin{pmatrix} \alpha \\ \beta \\ \gamma \end{pmatrix} = \begin{pmatrix} \sum DB \\ \sum B \\ \sum FB \end{pmatrix} \quad (63)$$

Through calculation and simplification, the closed-form solutions for α, β, and γ are given by (66), (67), and (68), as shown at the top of the page, respectively. Equations (69), (70), and (71), as shown at the top of the page, show the solutions in matrix form. Finally, the minimum SF standard deviation for the ABG model can be obtained by plugging (66), (67), and (68) back into (56). Or a system of simultaneous equations allow for α, β, and γ to be found by:

$$\begin{pmatrix} \alpha \\ \beta \\ \gamma \end{pmatrix} = \begin{pmatrix} \sum D^2 & \sum D & \sum DF \\ \sum D & N & \sum F \\ \sum DF & \sum F & \sum F^2 \end{pmatrix}^{-1} \begin{pmatrix} \sum DB \\ \sum B \\ \sum FB \end{pmatrix} \quad (64)$$

G. ABGX PATH LOSS MODEL

The ABGX model (5) is found in the exact same manner as the CIX and CIFX models. The α, β, and γ values found for the co-polarized ABG model (4) are substituted into the right hand side of (5) for all measured distances d to form a vector of estimated path loss values, specified as ABG_{PL}. Then using the cross-polarized path loss values in vector form B from measurements, the XPD factor for the ABGX model is:

$$\text{XPD} = \frac{\sum B - \sum ABG_{PL}}{N}. \quad (65)$$

APPENDIX B
OMNIDIRECTIONAL PATH LOSS VALUES

See Tables 19–22.

Acknowledgment

The authors wish to thank M. K. Samimi, T. Wu, K. Patade, and A. Hamza for their contribution to this project.

REFERENCES

[1] Z. Pi and F. Khan, "An introduction to millimeter-wave mobile broadband systems," *IEEE Commun. Mag.*, vol. 49, no. 6, pp. 101–107, Jun. 2011.
[2] Y. Li, J. Yang, and N. Ansari, "Cellular smartphone traffic and user behavior analysis," in *Proc. IEEE Int. Conf. Commun. (ICC)*, Jun. 2014, pp. 1326–1331.
[3] T. S. Rappaport, "Keynote speech: Millimeter wave wireless communications—The renaissance of computing and communications," presented at the *IEEE Int. Conf. Commun. (ICC)*, Sydney, NSW, Australia, Jun. 2014. [Online]. Available: http://icc2014.ieee-icc.org/speakers_28_4101586138.pdf
[4] F. Aldhaban, "Exploring the adoption of smartphone technology: Literature review," in *Proc. Technol. Manage. Emerg. Technol. (PICMET)*, Jul./Aug. 2012, pp. 2758–2770.
[5] Gartner. (Dec. 2014). *Gartner Says by 2018, More Than 50 Percent of Users Will Use a Tablet or Smartphone First for All Online Activities*. [Online]. Available: http://www.gartner.com/newsroom/id/2939217
[6] T. S. Rappaport *et al.*, "Millimeter wave mobile communications for 5G cellular: It will work!" *IEEE Access*, vol. 1, pp. 335–349, May 2013.
[7] T. S. Rappaport, R. W. Heath, Jr., R. C. Daniels, and J. N. Murdock, *Millimeter Wave Wireless Communications*. Englewood Cliffs, NJ, USA: Prentice-Hall, 2015.
[8] CISCO. (2007). *20 Myths of Wi-Fi Interference: Dispel Myths to Gain High Performing and Reliable Wireless*. http://www.cisco.com/c/en/us/products/collateral/wireless/spectrum-expert-wi-fi/prod_white_paper0900aecd807395a9.pdf
[9] Z. Hays, G. Richter, S. Berger, C. Baylis, and R. J. Marks, "Alleviating airport WiFi congestion: An comparison of 2.4 GHz and 5 GHz WiFi usage and capabilities," in *Proc. Texas Symp. Wireless Microw. Circuits Syst. (WMCS)*, Apr. 2014, pp. 1–4.
[10] C. Na, J. K. Chen, and T. S. Rappaport, "Hotspot traffic statistics and throughput models for several applications," in *Proc. IEEE Global Telecommun. Conf. (GLOBECOM)*, Nov./Dec. 2004, pp. 3257–3263.
[11] C. Na, J. K. Chen, and T. S. Rappaport, "Measured traffic statistics and throughput of IEEE 802.11b public WLAN hotspots with three different applications," *IEEE Trans. Wireless Commun.*, vol. 5, no. 11, pp. 3296–3305, Nov. 2006.
[12] C. Sergiou, P. Antoniou, and V. Vassiliou, "A comprehensive survey of congestion control protocols in wireless sensor networks," *IEEE Commun. Surveys Tuts.*, vol. 16, no. 4, pp. 1839–1859, Nov. 2014.

[13] P. Smulders, "Exploiting the 60 GHz band for local wireless multimedia access: Prospects and future directions," *IEEE Commun. Mag.*, vol. 40, no. 1, pp. 140–147, Jan. 2002.

[14] H. Xu, V. Kukshya, and T. S. Rappaport, "Spatial and temporal characteristics of 60-GHz indoor channels," *IEEE J. Sel. Areas Commun.*, vol. 20, no. 3, pp. 620–630, Apr. 2002.

[15] A. Maltsev, R. Maslennikov, A. Sevastyanov, A. Khoryaev, and A. Lomayev, "Experimental investigations of 60 GHz WLAN systems in office environment," *IEEE J. Sel. Areas Commun.*, vol. 27, no. 8, pp. 1488–1499, Oct. 2009.

[16] X. Ge, H. Cheng, M. Guizani, and T. Han, "5G wireless backhaul networks: Challenges and research advances," *IEEE Netw.*, vol. 28, no. 6, pp. 6–11, Nov./Dec. 2014.

[17] T. S. Rappaport, J. N. Murdock, and F. Gutierrez, Jr., "State of the art in 60-GHz integrated circuits and systems for wireless communications," *Proc. IEEE*, vol. 99, no. 8, pp. 1390–1436, Aug. 2011.

[18] R. C. Daniels, J. N. Murdock, T. S. Rappaport, and R. W. Heath, Jr., "60 GHz wireless: Up close and personal," *IEEE Microw. Mag.*, vol. 11, no. 7, pp. 44–50, Dec. 2010.

[19] E. Perahia, C. Cordeiro, M. Park, and L. L. Yang, "IEEE 802.11ad: Defining the next generation multi-Gbps Wi-Fi," in *Proc. 7th IEEE Consum. Commun. Netw. Conf. (CCNC)*, Jan. 2010, pp. 1–5.

[20] N. Guo, R. C. Qiu, S. S. Mo, and K. Takahashi, "60-GHz millimeter-wave radio: Principle, technology, and new results," *EURASIP J. Wireless Commun. Netw.*, vol. 2007, no. 1, pp. 1–8, 2007.

[21] C. H. Doan, S. Emami, D. A. Sobel, A. M. Niknejad, and R. W. Brodersen, "Design considerations for 60 GHz CMOS radios," *IEEE Commun. Mag.*, vol. 42, no. 12, pp. 132–140, Dec. 2004.

[22] S. K. Reynolds *et al.*, "A silicon 60-GHz receiver and transmitter chipset for broadband communications," *IEEE J. Solid-State Circuits*, vol. 41, no. 12, pp. 2820–2831, Dec. 2006.

[23] F. Gutierrez, Jr., K. Parrish, and T. S. Rappaport, "On-chip integrated antenna structures in CMOS for 60 GHz WPAN systems," in *Proc. IEEE Global Telecommun. Conf. (GLOBECOM)*, Nov./Dec. 2009, pp. 1–7.

[24] S. K. Yong and C.-C. Chong, "An overview of multigigabit wireless through millimeter wave technology: Potentials and technical challenges," *EURASIP J. Wireless Commun. Netw.*, vol. 2007, no. 1, pp. 1–10, 2007.

[25] M. Chelouche and A. Plattner, "Mobile broadband system (MBS): Trends and impact on 60 GHz band MMIC development," *Electron. Commun. Eng. J.*, vol. 5, no. 3, pp. 187–197, Jun. 1993.

[26] Y. Shoji, K. Hamaguchi, and H. Ogawa, "Millimeter-wave remote self-heterodyne system for extremely stable and low-cost broad-band signal transmission," *IEEE Trans. Microw. Theory Techn.*, vol. 50, no. 6, pp. 1458–1468, Jun. 2002.

[27] D. Cabric, M. S. W. Chen, D. A. Sobel, S. Wang, J. Yang, and R. W. Brodersen, "Novel radio architectures for UWB, 60 GHz, and cognitive wireless systems," *EURASIP J. Wireless Commun. Netw.*, vol. 2006, no. 2, pp. 1–18, 2006.

[28] C. J. Hansen, "WiGig: Multi-gigabit wireless communications in the 60 GHz band," *IEEE Wireless Commun.*, vol. 18, no. 6, pp. 6–7, Dec. 2011.

[29] (Jun. 2010). *WiGig White Paper: Defining the Future of Multi-Gigabit Wireless Communications*. [Online]. Available: http://wirelessgigabitalliance.org/specifications/

[30] T. Urushihara *et al.*, "60 GHz wireless technologies for WiGig/IEEE 802.11ad multi-gigabit systems," in *Proc. Asia-Pacific Microw. Conf. (APMC)*, Nov. 2014, pp. 628–630.

[31] D. Wang and C. Chan, "Multiband antenna for WiFi and WiGig communications," *IEEE Antennas Wireless Propag. Lett.*, 2015, to be published.

[32] D. Pepe and D. Zito, "60-GHz transceivers for wireless HD uncompressed video communication in nano-era CMOS technology," in *Proc. 15th IEEE Medit. Electrotech. Conf. (MELECON)*, Apr. 2010, pp. 1237–1240.

[33] D. Pepe and D. Zito, "60-GHz transceivers in nano-scale CMOS technology for WirelessHD standard applications," in *Proc. IET Irish Signals Syst. Conf. (ISSC)*, Jun. 2012, pp. 1–5.

[34] T. S. Rappaport, "Plenary speech: The renaissance of wireless communications in the massively Broadband® era," in *Proc. IEEE Veh. Technol. Conf. (2012 IEEE VTC-Fall)*, Quebec City, QC, Canada, Sep. 2012. [Online]. Available: http://nyuwireless.com/VTSPlenary.pdf

[35] Y. Takimoto and T. Ihara, "Research activities on millimeter wave indoor communication systems in Japan," in *IEEE MTT-S Int. Microw. Symp. Dig.*, vol. 2. Jun. 1993, pp. 673–676.

[36] T. Ihara, T. Manabe, M. Fujita, T. Matsui, and Y. Sugimoto, "Research activities on millimeter-wave indoor wireless communication systems at CRL," in *Proc. 4th IEEE Int. Conf. Universal Pers. Commun.*, Nov. 1995, pp. 197–200.

[37] P. Shrivastava and T. Rama Rao, "Performance investigations with antipodal linear tapered slot antenna on 60 GHz radio link in a narrow hallway environment," *Prog. Electromagn. Res. C*, vol. 58, pp. 69–77, Jun. 2015.

[38] A. Kumar and T. Rama Rao, "Analysis of planning and deployment issues for short range gigabit radio's at 60 GHz," in *Proc. Int. Conf. Commun. Signal Process. (ICCSP)*, Apr. 2013, pp. 24–28.

[39] S. Ramesh and T. Rama Rao, "Indoor radio link characterization studies for millimeter wave wireless communications utilizing dielectric-loaded exponentially tapered slot antenna," *J. Electromagn. Waves Appl.*, vol. 29, no. 4, pp. 551–564, Feb. 2015.

[40] S. E. Alexander, "Characterising buildings for propagation at 900 MHz," *Electron. Lett.*, vol. 19, no. 20, p. 860, Sep. 1983.

[41] D. Akerberg, "Properties of a TDMA pico cellular office communication system," in *Proc. IEEE 39th Veh. Technol. Conf.*, vol. 1. May 1989, pp. 186–191.

[42] A. A. M. Saleh and R. A. Valenzuela, "A statistical model for indoor multipath propagation," *IEEE J. Sel. Areas Commun.*, vol. 5, no. 2, pp. 128–137, Feb. 1987.

[43] R. J. C. Bultitude, "Measurement, characterization and modeling of indoor 800/900 MHz radio channels for digital communications," *IEEE Commun. Mag.*, vol. 25, no. 6, pp. 5–12, Jun. 1987.

[44] A. J. Motley and J. M. P. Keenan, "Personal communication radio coverage in buildings at 900 MHz and 1700 MHz," *Electron. Lett.*, vol. 24, no. 12, pp. 763–764, Jun. 1988.

[45] T. S. Rappaport, "Characterization of UHF multipath radio channels in factory buildings," *IEEE Trans. Antennas Propag.*, vol. 37, no. 8, pp. 1058–1069, Aug. 1989.

[46] T. S. Rappaport and D. A. Hawbaker, "Effects of circular and linear polarized antennas on wideband propagation parameters in indoor radio channels," in *Proc. 1991 IEEE Global Telecommun. Conf. (GLOBECOM)*, vol. 2. Dec. 1991, pp. 1287–1291.

[47] A. F. Molisch, L. J. Greenstein, and M. Shafi, "Propagation issues for cognitive radio," *Proc. IEEE*, vol. 97, no. 5, pp. 787–804, May 2009.

[48] C. M. P. Ho, T. S. Rappaport, and M. P. Koushik, "Antenna effects on indoor obstructed wireless channels and a deterministic image-based wide-band propagation model for in-building personal communication systems," *Int. J. Wireless Inf. Netw.*, vol. 1, no. 1, pp. 61–76, Jan. 1994.

[49] J. B. Andersen, T. S. Rappaport, and S. Yoshida, "Propagation measurements and models for wireless communications channels," *IEEE Commun. Mag.*, vol. 33, no. 1, pp. 42–49, Jan. 1995.

[50] T. S. Rappaport and S. Sandhu, "Radio-wave propagation for emerging wireless personal-communication systems," *IEEE Antennas Propag. Mag.*, vol. 36, no. 5, pp. 14–24, Oct. 1994.

[51] A. Alvarez, G. Valera, M. Lobeira, R. P. Torres, and J. L. Garcia, "Ultra wideband channel model for indoor environments," *J. Commun. Netw.*, vol. 5, no. 4, pp. 309–318, Dec. 2003.

[52] S. S. Ghassemzadeh, R. Jana, C. W. Rice, W. Turin, and V. Tarokh, "Measurement and modeling of an ultra-wide bandwidth indoor channel," *IEEE Trans. Commun.*, vol. 52, no. 10, pp. 1786–1796, Oct. 2004.

[53] G. D. Durgin, T. S. Rappaport, and H. Xu, "Partition-based path loss analysis for in-home and residential areas at 5.85 GHz," in *Proc. IEEE Global Telecommun. Conf. (GLOBECOM)*, vol. 2. Nov. 1998, pp. 904–909.

[54] G. D. Durgin, T. S. Rappaport, and H. Xu, "Radio path loss and penetration loss measurements in and around homes and trees at 5.85 GHz," in *Proc. IEEE Antennas Propag. Soc. Int. Symp.*, vol. 2. Jun. 1998, pp. 618–621.

[55] G. D. Durgin, T. S. Rappaport, and H. Xu, "5.85-GHz radio path loss and penetration loss measurements in and around homes and trees," *IEEE Commun. Lett.*, vol. 2, no. 3, pp. 70–72, Mar. 1998.

[56] G. D. Durgin, T. S. Rappaport, and H. Xu, "Measurements and models for radio path loss and penetration loss in and around homes and trees at 5.85 GHz," *IEEE Trans. Commun.*, vol. 46, no. 11, pp. 1484–1496, Nov. 1998.

[57] G. D. Durgin, V. Kukshya, and T. S. Rappaport, "Wideband measurements of angle and delay dispersion for outdoor and indoor peer-to-peer radio channels at 1920 MHz," *IEEE Trans. Antennas Propag.*, vol. 51, no. 5, pp. 936–944, May 2003.

[58] G. D. Durgin, V. Kukshya, and T. S. Rappaport, "Joint angle and delay spread statistics for 1920 MHz peer-to-peer wireless channels," in *Proc. IEEE Antennas Propag. Soc. Int. Symp.*, vol. 2. Jul. 2001, pp. 182–185.

[59] N. Patwari, G. D. Durgin, T. S. Rappaport, and R. J. Boyle, "Peer-to-peer low antenna outdoor radio wave propagation at 1.8 GHz," in *Proc. IEEE 49th Veh. Technol. Conf.*, vol. 1. Jul. 1999, pp. 371–375.

[60] J. W. McKown and R. L. Hamilton, Jr., "Ray tracing as a design tool for radio networks," *IEEE Netw.*, vol. 5, no. 6, pp. 27–30, Nov. 1991.

[61] G. E. Athanasiadou, A. R. Nix, and J. P. McGeehan, "A ray tracing algorithm for microcellular wideband propagation modelling," in *Proc. IEEE 45th Veh. Technol. Conf.*, vol. 1. Jul. 1995, pp. 261–265.

[62] K. R. Schaubach, N. J. Davis, IV, and T. S. Rappaport, "A ray tracing method for predicting path loss and delay spread in microcellular environments," in *Proc. IEEE 42nd Veh. Technol. Conf.*, May 1992, pp. 932–935.

[63] S. Y. Seidel and T. S. Rappaport, "A ray tracing technique to predict path loss and delay spread inside buildings," in *Proc. IEEE Global Telecommun. Conf.*, vol. 2. Dec. 1992, pp. 649–653.

[64] S. Y. Seidel and T. S. Rappaport, "Site-specific propagation prediction for wireless in-building personal communication system design," *IEEE Trans. Veh. Technol.*, vol. 43, no. 4, pp. 879–891, Nov. 1994.

[65] S. Y. Seidel, K. R. Schaubach, T. T. Tran, and T. S. Rappaport, "Research in site-specific propagation modeling for PCS system design," in *Proc. 43rd IEEE Veh. Technol. Conf.*, May 1993, pp. 261–264.

[66] R. R. Skidmore, T. S. Rappaport, and A. L. Abbott, "Interactive coverage region and system design simulation for wireless communication systems in multifloored indoor environments: SMT *Plus*," in *Proc. 5th IEEE Int. Conf. Universal Pers. Commun.*, vol. 2. Sep. 1996, pp. 646–650.

[67] S. Y. Seidel and T. S. Rappaport, "Path loss prediction in multifloored buildings at 914 MHz," *Electron. Lett.*, vol. 27, no. 15, pp. 1384–1387, Jul. 1991.

[68] G. D. Durgin, N. Patwari, and T. S. Rappaport, "Improved 3D ray launching method for wireless propagation prediction," *Electron. Lett.*, vol. 33, no. 16, pp. 1412–1413, Jul. 1997.

[69] T. S. Rappaport, S. Y. Seidel, and K. Takamizawa, "Statistical channel impulse response models for factory and open plan building radio communicate system design," *IEEE Trans. Commun.*, vol. 39, no. 5, pp. 794–807, May 1991.

[70] T. S. Rappaport, W. Huang, and M. J. Feuerstein, "Performance of decision feedback equalizers in simulated urban and indoor radio channels," *IEICE Trans. Commun.*, vol. E76-B, no. 2, pp. 78–79, Feb. 1993.

[71] T. S. Rappaport, S. Y. Seidel, and R. Singh, "900-MHz multipath propagation measurements for U.S. digital cellular radiotelephone," *IEEE Trans. Veh. Technol.*, vol. 39, no. 2, pp. 132–139, May 1990.

[72] S. Y. Seidel, T. S. Rappaport, S. Jain, M. L. Lord, and R. Singh, "Path loss, scattering and multipath delay statistics in four European cities for digital cellular and microcellular radiotelephone," *IEEE Trans. Veh. Technol.*, vol. 40, no. 4, pp. 721–730, Nov. 1991.

[73] T. S. Rappaport, *Wireless Communications: Principles and Practice*, 2nd ed. Upper Saddle River, NJ, USA: Prentice-Hall, 2002.

[74] J. E. Nuckols, "Implementation of geometrically based single-bounce models for simulation of angle-of-arrival of multipath delay components in the wireless channel simulation tools, SMRCIM and SIRCIM," M.S. thesis, Dept. Elect. Eng., Virginia Polytechnic Inst. State Univ., Blacksburg, VA, USA, 1999.

[75] P. F. M. Smulders and A. G. Wagemans, "Wide-band measurements of MM-wave indoor radio channels," in *Proc. 3rd IEEE Int. Symp. Pers., Indoor Mobile Radio Commun. (PIMRC)*, Oct. 1992, pp. 329–333.

[76] P. F. M. Smulders and A. G. Wagemans, "Wideband indoor radio propagation measurements at 58 GHz," *Electron. Lett.*, vol. 28, no. 13, pp. 1270–1272, Jun. 1992.

[77] P. F. M. Smulders and A. G. Wagemans, "Frequency-domain measurement of the millimeter wave indoor radio channel," *IEEE Trans. Instrum. Meas.*, vol. 44, no. 6, pp. 1017–1022, Dec. 1995.

[78] H. Xu, V. Kukshya, and T. S. Rappaport, "Spatial and temporal characterization of 60 GHz indoor channels," in *Proc. 52nd IEEE Veh. Technol. Conf. (2000 IEEE VTC-Fall)*, vol. 1. Sep. 2000, pp. 6–13.

[79] M. Bensebti, J. P. McGeehan, and M. A. Beach, "Indoor multipath radio propagation measurements and characterisation at 60 GHz," in *Proc. 21st Eur. Microw. Conf.*, vol. 2. Sep. 1991, pp. 1217–1222.

[80] T. Zwick, T. J. Beukema, and H. Nam, "Wideband channel sounder with measurements and model for the 60 GHz indoor radio channel," *IEEE Trans. Veh. Technol.*, vol. 54, no. 4, pp. 1266–1277, Jul. 2005.

[81] S. Geng, J. Kivinen, X. Zhao, and P. Vainikainen, "Millimeter-wave propagation channel characterization for short-range wireless communications," *IEEE Trans. Veh. Technol.*, vol. 58, no. 1, pp. 3–13, Jan. 2009.

[82] S. Geng, J. Kivinen, and P. Vainikainen, "Propagation characterization of wideband indoor radio channels at 60 GHz," in *Proc. IEEE Int. Symp. Microw., Antenna, Propag. EMC Technol. Wireless Commun.*, vol. 1. Aug. 2005, pp. 314–317.

[83] C. R. Anderson and T. S. Rappaport, "In-building wideband partition loss measurements at 2.5 and 60 GHz," *IEEE Trans. Wireless Commun.*, vol. 3, no. 3, pp. 922–928, May 2004.

[84] C. R. Anderson *et al.*, "In-building wideband multipath characteristics at 2.5 and 60 GHz," in *Proc. IEEE 56th Veh. Technol. Conf. (2002 IEEE VTC-Fall)*, vol. 1. Sep. 2002, pp. 97–101.

[85] T. Manabe, Y. Miura, and T. Ihara, "Effects of antenna directivity and polarization on indoor multipath propagation characteristics at 60 GHz," *IEEE J. Sel. Areas Commun.*, vol. 14, no. 3, pp. 441–448, Apr. 1996.

[86] T. Manabe *et al.*, "Polarization dependence of multipath propagation and high-speed transmission characteristics of indoor millimeter-wave channel at 60 GHz," *IEEE Trans. Veh. Technol.*, vol. 44, no. 2, pp. 268–274, May 1995.

[87] N. Moraitis and P. Constantinou, "Millimeter wave propagation measurements and characterization in an indoor environment for wireless 4G systems," in *Proc. IEEE 16th Int. Symp. Pers., Indoor Mobile Radio Commun. (PIMRC)*, vol. 1. Sep. 2005, pp. 594–598.

[88] A. Maltsev, E. Perahia, R. Maslennikov, A. Sevastyanov, A. Lomayev, and A. Khoryaev, "Impact of polarization characteristics on 60-GHz indoor radio communication systems," *IEEE Antennas Wireless Propag. Lett.*, vol. 9, pp. 413–416, May 2010.

[89] E. Torkildson, C. Sheldon, U. Madhow, and M. Rodwell, "Millimeter-wave spatial multiplexing in an indoor environment," in *Proc. IEEE GLOBECOM Workshops*, Nov./Dec. 2009, pp. 1–6.

[90] E. Torkildson, U. Madhow, and M. Rodwell, "Indoor millimeter wave MIMO: Feasibility and performance," *IEEE Trans. Wireless Commun.*, vol. 10, no. 12, pp. 4150–4160, Dec. 2011.

[91] K. Haneda, J. Järveläinen, A. Karttunen, M. Kyrö, and J. Putkonen, "Indoor short-range radio propagation measurements at 60 and 70 GHz," in *Proc. 8th Eur. Conf. Antennas Propag. (EuCAP)*, Apr. 2014, pp. 634–638.

[92] J. Poutanen, J. Salmi, K. Haneda, V. Kolmonen, and P. Vainikainen, "Angular and shadowing characteristics of dense multipath components in indoor radio channels," *IEEE Trans. Antennas Propag.*, vol. 59, no. 1, pp. 245–253, Jan. 2011.

[93] X. Wu, Y. Zhang, C.-X. Wang, G. Goussetis, E.-H. M. Aggoune, and M. M. Alwakeel, "28 GHz indoor channel measurements and modelling in laboratory environment using directional antennas," in *Proc. 9th Eur. Conf. Antennas Propag. (EuCAP)*, Apr. 2015, pp. 1–5.

[94] M. Lei, J. Zhang, T. Lei, and D. Du, "28-GHz indoor channel measurements and analysis of propagation characteristics," in *Proc. IEEE 25th Annu. Int. Symp. Pers., Indoor, Mobile Radio Commun. (PIMRC)*, Sep. 2014, pp. 208–212.

[95] K. Haneda, "Channel models and beamforming at millimeter-wave frequency bands," *IEICE Trans. Commun.*, vol. E98-B, no. 5, pp. 755–772, May 2015.

[96] *Allocations and Service Rules for the 71–76 GHz, 81–86 GHz, and 92–95 GHz Bands, FCC Memorandum Opinion Order 05-45*, Federal Commun. Commission, Washington, DC, USA, 2010.

[97] *Radio Frequency Channel Arrangements for Fixed Service Systems Operating in the Bands 71–76 GHz and 81–86 GHz*, document ECC Rec. (05)07, Electronic Communications Committee, 2005.

[98] *Making Spectrum Available for the 71–78 GHz and 81–86 GHz Bands*, Ofcom, London, U.K., Nov. 2006.

[99] *Consultation on a Renewed Spectrum Policy Framework for Canada and Continued Advancements in Spectrum Management*, document DGTP-001-005, Sep. 2005.

[100] Federal Communications Commission. (Oct. 2014). *FCC 14-154*. [Online]. Available: https://apps.fcc.gov/edocs_public/attachmatch/FCC-14-154A1.pdf

[101] Federal Communications Commission. (Jan. 2015). *FCC 14-177*. [Online]. Available: http://apps.fcc.gov/ecfs/proceeding/view?name=14-177

[102] Ofcom. (Feb. 2015). *Spectrum Above 6 GHz for Future Mobile Communications*. [Online]. Available: http://stakeholders.ofcom.org.uk/binaries/consultations/above-6ghz/summary/spectrum_above_6_GHz_CFI.pdf

[103] S. Deng, C. J. Slezak, G. R. MacCartney, Jr., and T. S. Rappaport, "Small wavelengths—Big potential: Millimeter wave propagation measurements for 5G," *Microw. J.*, vol. 57, no. 11, pp. 4–12, Sep. 2014.

[104] Y. Azar *et al.*, "28 GHz propagation measurements for outdoor cellular communications using steerable beam antennas in New York City," in *Proc. IEEE Int. Conf. Commun. (ICC)*, Jun. 2013, pp. 5143–5147.

[105] M. K. Samimi *et al.*, "28 GHz angle of arrival and angle of departure analysis for outdoor cellular communications using steerable beam antennas in New York City," in *Proc. IEEE 77th Veh. Technol. Conf. (2013 IEEE VTC-Spring)*, Jun. 2013, pp. 1–6.

[106] G. R. MacCartney, Jr., and T. S. Rappaport, "73 GHz millimeter wave propagation measurements for outdoor urban mobile and backhaul communications in New York City," in *Proc. IEEE Int. Conf. Commun. (ICC)*, Jun. 2014, pp. 4862–4867.

[107] T. S. Rappaport and S. Deng, "73 GHz wideband millimeter-wave foliage and ground reflection measurements and models," in *Proc. IEEE Int. Conf. Commun. Workshop (ICCW)*, Jun. 2015, pp. 1238–1243.

[108] S. Nie, G. R. MacCartney, Jr., S. Sun, and T. S. Rappaport, "72 GHz millimeter wave indoor measurements for wireless and backhaul communications," in *Proc. IEEE 24th Int. Symp. Pers. Indoor Mobile Radio Commun. (PIMRC)*, Sep. 2013, pp. 2429–2433.

[109] S. Deng, M. K. Samimi, and T. S. Rappaport, "28 GHz and 73 GHz millimeter-wave indoor propagation measurements and path loss models," in *Proc. IEEE Int. Conf. Commun. Workshop (ICCW)*, Jun. 2015, pp. 1244–1250.

[110] D. C. Cox, "Delay doppler characteristics of multipath propagation at 910 MHz in a suburban mobile radio environment," *IEEE Trans. Antennas Propag.*, vol. AP-20, no. 5, pp. 625–635, Sep. 1972.

[111] R. J. Pirkl and G. D. Durgin, "Optimal sliding correlator channel sounder design," *IEEE Trans. Wireless Commun.*, vol. 7, no. 9, pp. 3488–3497, Sep. 2008.

[112] T. S. Rappaport, G. R. MacCartney, Jr., M. K. Samimi, and S. Sun, "Wideband millimeter-wave propagation measurements and channel models for future wireless communication system design (invited paper)," *IEEE Trans. Commun.*, vol. 63, no. 9, pp. 3029–3056, Sep. 2015.

[113] S. Y. Seidel and T. S. Rappaport, "914 MHz path loss prediction models for indoor wireless communications in multifloored buildings," *IEEE Trans. Antennas Propag.*, vol. 40, no. 2, pp. 207–217, Feb. 1992.

[114] V. S. Abhayawardhana, I. J. Wassell, D. Crosby, M. P. Sellars, and M. G. Brown, "Comparison of empirical propagation path loss models for fixed wireless access systems," in *Proc. IEEE 61st Veh. Technol. Conf. (2015 IEEE VTC-Spring)*, vol. 1. May/Jun. 2005, pp. 73–77.

[115] T. S. Rappaport and D. A. Hawbaker, "Wide-band microwave propagation parameters using circular and linear polarized antennas for indoor wireless channels," *IEEE Trans. Commun.*, vol. 40, no. 2, pp. 240–245, Feb. 1992.

[116] P. Kyösti *et al.*, "WINNER II channel models," Eur. Commission, IST-WINNER, Tech. Rep. D1.1.2.

[117] (Sep. 2003). "Spatial channel model for multiple input multiple output (MIMO) simulations," 3rd Generat. Partnership Project, Tech. Rep. TR 25.996. [Online]. Available: http://www.3gpp.org

[118] M. K. Samimi, T. S. Rappaport, and G. R. MacCartney, Jr., "Probabilistic omnidirectional path loss models for millimeter-wave outdoor communications," *IEEE Wireless Commun. Lett.*, vol. 4, no. 4, pp. 357–360, Aug. 2015.

[119] A. I. Sulyman, A. T. Nassar, M. K. Samimi, G. R. MacCartney, Jr., T. S. Rappaport, and A. Alsanie, "Radio propagation path loss models for 5G cellular networks in the 28 GHz and 38 GHz millimeter-wave bands," *IEEE Commun. Mag.*, vol. 52, no. 9, pp. 78–86, Sep. 2014.

[120] G. R. MacCartney, Jr., J. Zhang, S. Nie, and T. S. Rappaport, "Path loss models for 5G millimeter wave propagation channels in urban microcells," in *Proc. IEEE Global Commun. Conf. (GLOBECOM)*, Dec. 2013, pp. 3948–3953.

[121] S. Piersanti, L. A. Annoni, and D. Cassioli, "Millimeter waves channel measurements and path loss models," in *Proc. IEEE Int. Conf. Commun. (ICC)*, Jun. 2012, pp. 4552–4556.

[122] S. Sun *et al.*, "Propagation path loss models for 5G urban micro- and macro-cellular scenarios," in *Proc. IEEE 83rd Veh. Technol. Conf. (2016 IEEE VTC-Spring)*, 2016, submitted.

[123] G. R. MacCartney, Jr., M. K. Samimi, and T. S. Rappaport, "Exploiting directionality for millimeter-wave wireless system improvement," in *Proc. IEEE Int. Conf. Commun. (ICC)*, Jun. 2015, pp. 4019–4025.

[124] S. Sun, T. S. Rappaport, R. W. Heath, Jr., A. Nix, and S. Rangan, "MIMO for millimeter-wave wireless communications: Beamforming, spatial multiplexing, or both?" *IEEE Commun. Mag.*, vol. 52, no. 12, pp. 110–121, Dec. 2014.

[125] T. S. Rappaport, F. Gutierrez, Jr., E. Ben-Dor, J. N. Murdock, Y. Qiao, and J. I. Tamir, "Broadband millimeter-wave propagation measurements and models using adaptive-beam antennas for outdoor urban cellular communications," *IEEE Trans. Antennas Propag.*, vol. 61, no. 4, pp. 1850–1859, Apr. 2013.

[126] E. Ben-Dor, T. S. Rappaport, Y. Qiao, and S. J. Lauffenburger, "Millimeter-wave 60 GHz outdoor and vehicle AOA propagation measurements using a broadband channel sounder," in *Proc. IEEE Global Telecommun. Conf. (GLOBECOM)*, Dec. 2011, pp. 1–6.

[127] T. S. Rappaport, E. Ben-Dor, J. N. Murdock, and Y. Qiao, "38 GHz and 60 GHz angle-dependent propagation for cellular & peer-to-peer wireless communications," in *Proc. IEEE Int. Conf. Commun. (ICC)*, Jun. 2012, pp. 4568–4573.

[128] P. Nobles, D. Ashworth, and F. Halsall, "Propagation measurements in an indoor radio environment at 2, 5 and 17 GHz," in *Proc. IEE Colloq. High Bit Rate UHF/SHF Channel Sounders, Technol. Meas.*, Dec. 1993, pp. 4/1–4/6.

[129] S. Sun and T. S. Rappaport, "Multi-beam antenna combining for 28 GHz cellular link improvement in urban environments," in *Proc. IEEE Global Commun. Conf. (GLOBECOM)*, Dec. 2013, pp. 3754–3759.

[130] S. Sun, G. R. MacCartney, Jr., M. K. Samimi, S. Nie, and T. S. Rappaport, "Millimeter wave multi-beam antenna combining for 5G cellular link improvement in New York City," in *Proc. IEEE Int. Conf. Commun. (ICC)*, Jun. 2014, pp. 5468–5473.

[131] M. Käske, C. Schneider, W. Kotterman, and R. Thomä, "Solving the problem of choosing the right MIMO measurement antenna: Embedding/de-embedding," in *Proc. 5th Eur. Conf. Antennas Propag. (EUCAP)*, Apr. 2011, pp. 2551–2555.

[132] G. R. MacCartney, Jr., M. K. Samimi, and T. S. Rappaport, "Omnidirectional path loss models in New York City at 28 GHz and 73 GHz," in *Proc. IEEE 25th Int. Symp. Pers. Indoor Mobile Radio Commun. (PIMRC)*, Sep. 2014, pp. 227–231.

[133] S. Sun, G. R. MacCartney, Jr., M. K. Samimi, and T. S. Rappaport, "Synthesizing omnidirectional antenna patterns, received power and path loss from directional antennas for 5G millimeter-wave communications," in *Proc. IEEE Global Commun. Conf. (GLOBECOM)*, Dec. 2015.

[134] U. Beckman and C. Wahlberg, "Antenna systems for polarization diversity: Reducing the size and number of antennas needed for mobile network deployment through polariztion diversity," *Microw. J.*, May 1997.

[135] A. Ghosh *et al.*, "Millimeter-wave enhanced local area systems: A high-data-rate approach for future wireless networks," *IEEE J. Sel. Areas Commun.*, vol. 32, no. 6, pp. 1152–1163, Jun. 2014.

[136] Y. Zahedi, R. Ngah, U. A. K. Chude-Okonkwo, S. Nunoo, and M. Mokayef, "Modeling the RMS delay spread in time-varying UWB communication channels," in *Proc. 5th Int. Conf. Intell. Adv. Syst. (ICIAS)*, Jun. 2014, pp. 1–5.

[137] H. Hashemi and D. Tholl, "Statistical modeling and simulation of the RMS delay spread of indoor radio propagation channels," *IEEE Trans. Veh. Technol.*, vol. 43, no. 1, pp. 110–120, Feb. 1994.

[138] H. Yang, P. F. M. Smulders, and M. H. A. J. Herben, "Indoor channel measurements and analysis in the frequency bands 2 GHz and 60 GHz," in *Proc. IEEE 16th Int. Symp. Pers., Indoor Mobile Radio Commun. (PIMRC)*, vol. 1. Sep. 2005, pp. 579–583.

[139] D. Devasirvatham, "A comparison of time delay spread and signal level measurements within two dissimilar office buildings," *IEEE Trans. Antennas Propag.*, vol. 35, no. 3, pp. 319–324, Mar. 1987.
[140] J. Qiao, X. Shen, J. W. Mark, and Y. He, "MAC-layer concurrent beamforming protocol for indoor millimeter-wave networks," *IEEE Trans. Veh. Technol.*, vol. 64, no. 1, pp. 327–338, Jan. 2015.
[141] Z. He, S. Mao, and T. S. Rappaport, "On link scheduling under blockage and interference in 60-GHz ad hoc networks," *IEEE Access*, vol. 3, pp. 1437–1449, Sep. 2015.
[142] P. Nobles and F. Halsall, "Delay spread and received power measurements within a building at 2 GHz, 5 GHz and 17 GHz," in *Proc. 10th Int. Conf. Antennas Propag.*, vol. 2. Apr. 1997, pp. 319–324.
[143] K. Minseok, Y. Konishi, and J.-I. Takada, "Large scale parameters and double-directional characterization of indoor wideband radio multipath channels at 11 GHz," *IEEE Trans. Antennas Propag.*, vol. 62, no. 1, pp. 430–441, Jan. 2014.
[144] J. Zhu, H. Wang, and W. Hong, "Large-scale fading characteristics of indoor channel at 45-GHz band," *IEEE Antennas Wireless Propag. Lett.*, vol. 14, pp. 735–738, Mar. 2015.
[145] J. Zhu, H. Wang, and W. Hong, "Characterization of large-scale fading for 45 GHz indoor channels," in *Proc. 3rd Asia-Pacific Conf. Antennas Propag. (APCAP)*, Jul. 2014, pp. 728–730.
[146] H. Zhao *et al.*, "28 GHz millimeter wave cellular communication measurements for reflection and penetration loss in and around buildings in New York City," in *Proc. IEEE Int. Conf. Commun. (ICC)*, Jun. 2013, pp. 5163–5167.

GEORGE R. MacCARTNEY, JR. received the B.S. and M.S. degrees in electrical engineering from Villanova University, Villanova, PA, USA, in 2010 and 2011, respectively. He is currently pursuing the Ph.D. degree in electrical engineering with the New York University (NYU) Tandon School of Engineering, Brooklyn, NY, USA, under the supervision of Prof. Rappaport with the NYU WIRELESS Research Center. He has authored or co-authored over 15 technical papers in the field of millimeter-wave (mmWave) measurements and models. His research interests include mmWave channel sounder prototyping and mmWave measurements, models, and analysis for 5G communications.

THEODORE S. RAPPAPORT is currently the David Lee/Ernst Weber Professor of Electrical and Computer Engineering with the New York University (NYU) Tandon School of Engineering, Brooklyn, NY, USA, and the Founding Director of the NYU WIRELESS Research Center. He also holds professorship positions with the Courant Institute of Mathematical Sciences and the NYU School of Medicine. He founded major wireless research centers with the Virginia Polytechnic Institute and State University (MPRG), The University of Texas at Austin (WNCG), and the NYU WIRELESS Research Center, and founded two wireless technology companies that were sold to publicly traded firms. He is a highly sought-after technical consultant having testified before the U.S. Congress and having served the ITU. He has advised more than 100 students. He holds more than 100 patents issued and pending, and has authored or co-authored several books, including the best-seller *Wireless Communications: Principles and Practice—Second Edition* (Prentice Hall, 2002). His latest book, entitled *Millimeter Wave Wireless Communications* (Pearson/Prentice Hall, 2015), is the first comprehensive text on the subject.

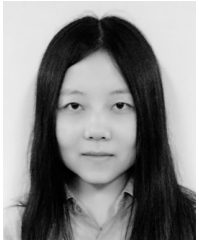

SHU SUN received the B.S. degree in applied physics from Shanghai Jiao Tong University, China, in 2012, and the M.S. degree in electrical engineering from the New York University (NYU) Tandon School of Engineering, Brooklyn, NY, USA, in 2014, where she is currently pursuing the Ph.D. degree in electrical engineering under the supervision of Prof. T. S. Rappaport, and doing research at the NYU WIRELESS Research Center. She has authored or co-authored over 15 technical papers in the field of millimeter-wave (mmWave) wireless communications. Her current research interests include mmWave mobile communications and the analysis of MIMO systems for mmWave channels.

SIJIA DENG (S'14) received the B.S. degree in electrical engineering from Sichuan University, China, in 2013. She is currently pursuing the M.S. and Ph.D. degrees in electrical engineering with the Department of Electrical and Computer Engineering, NYU WIRELESS Research Center, New York University Tandon School of Engineering, under the supervision of Prof. Rappaport. Her current research interests include millimeter-wave (mmWave) channel modeling and ray tracing propagation models for mmWave channels.